The Development of a Light Pulse Atom Interferometer Towards a Parameter Search of the Dark Contents of the Vacuum.

Thesis submitted in accordance with the requirements of
the University of Liverpool for the degree of Doctor in Philosophy
by
Oliver Stephen Burrow

May 16, 2016

Abstract

A parameter space search for dark contents of the vacuum utilising atom interferometry is motivated. This methodology is potentially sensitive to any dark contents of the vacuum that are spatially inhomogeneous on the lab scale, and couple to atoms in addition to the gravitational force. A path integral approach to atom interferometry is discussed and a parametrisation of the dark contents of the vacuum is presented. A magneto-optical trap is detailed, capable of trapping 6.5×10^7 atoms, as a cold atomic source for the atom interferometer.

The development of a prototype light pulse Mach-Zehnder atom interferometer, currently in the commissioning stages is described, as well as a unique laser system capable of running the whole atom interferometer from just two extended cavity diode lasers. Using this device 1×10^6 atoms are trapped in a magneto-optical trap and further cooled to 96 μK in an optical molasses. This prototype device is now undergoing upgrades to create larger, colder sources of atoms for the interferometer.

Contents

List of Figures

Authors Contribution

In 2011 I started my PhD working towards an experiment proposed by the Nobel Laureate, Martin Perl, to perform a parameter space search for the dark contents of the vacuum. My PhD has involved developing a prototype atom interferometer for this experiment. I essentially entered an almost empty lab, and built it from a hand-full of optical components and a laser to where it is today. Since initially starting work, many members have joined the group for which I am deeply grateful for their help and collegiality.

Initially I worked on developing the magneto-optical trap (MOT) apparatus (now in the third iteration – the first was an unsuccessful pyramidal MOT and is not included in this write-up but provided many valuable lessons), to act as a cold atom source for an atom interferometer. This work is presented in chapter 3. The laser sources, magnetic coils, warm atom source implemented here are used daily on the experiment. I also developed the MOT characterisation software and atom number measurements. This was realised in March 2013.

Chapter 4 presents the design of the prototype atom interferometer. The majority of the design was done in the summer of 2013 as a group effort, and the experiment was allocated a lab in October 2013. In this section I was responsible for the design and implementation of the MOT and molasses sections. This involved designing the optical circuit for the MOT and the magnetic field cancellation coils, which I also implemented. I also was involved in the preparation of the lab, and the assembling the vacuum chamber, I worked alongside colleagues to prepare and commission the prototype.

The laser system described in chapter 5 was designed alongside the prototype atom interferometer. I was involved in implementing this laser circuit, transferring the two laser sources from the MOT experiments, implementing the optical frequency control circuits and commissioning the AOMs. Finally, the measurements, as well as the molasses development presented in chapter 6 is also my own work.

Acknowledgement

First I must thank Jon Coleman, for giving this opportunity, and his constant support throughout my PhD. It amazes me to think that when I started working with Jon, there was only a few optics on an optical bench, and through Jon's determination there is a lab full of equipment and a group of people working on it. I must also thank Carl Metelko, who has been like a second supervisor since joining the experiment. The experiment is a team effort and I thank everyone who has contributed over the years, but in particular Joe Heffer and David Morris, who I spent many hours in the lab with and share more in-jokes with than I can count.

I would like to thank the whole of the particle physics group for my time spent in Liverpool. It was an exciting time be part of a particle physics group and the their support for the experiment was greatly appreciated. The workshop deserve a special mention for all the odd jobs they did for me over the years and also their constant humour. I must also thank the Cockcroft institute and Swapan for providing the funding for my PhD.

Whilst there are far too many to name, as they span seven or eight years of intake, my fellow PhD students were integral to my experience of Liverpool. I moved to Liverpool not knowing anyone and there was a really sense of community amongst the students. I'm going to look look back fondly on the trips to the AJ and the 5-aside, I wish you luck in the future Bubble Chamber football, you can't lose in the final every year forever! Matt Murdoch deserves a special mention for putting up living with me for three years, cheers!

Thanks to my family. Thank you, Mum, Dad, Sam, Edwin, for the support and interest in what I'm doing.

And finally, Martin Perl, is unfortunately no longer with us, came up with the concept for the experiment. It was a pleasure meeting you and collaborating.

Chapter 1

Introduction and Motivation

1.1 Knowledge of Dark Energy in Modern physics

Current cosmological observations indicate that the universe is spatially flat, consisting of 4.9% normal matter (as described by the standard model of particle physics), 26.8% dark matter and 68.3% dark energy [1]. These conclusions are arrived at by taking data from cosmological observations, such as the cosmic microwave background (CMB) [2], baryonic acoustic oscillations (BAO) [3] and type 1A supernovae [4], and fitting them to cosmological models.

The best fitting model to the data is the Λ-CDM model, a universe with a cosmological constant and cold dark matter. The model is constructed from general relativity using the principle that the universe is homogeneous and isotropic on a cosmological scale [5]. In this model, dark energy is treated as the cosmological constant, a constant energy density pervading all space, exerting a negative pressure on the universe, causing an accelerated expansion. This model is chosen, being the simplest that describes the data.

Other theories attempt to explain dark energy, and are seeking experimental validation. Current observations are not precise enough to distinguish them from the cosmological constant [5]. The possibility of a modified gravity theory explaining modern cosmological observations has been suggested, but no current model is more convincing that general relativity [5]. Little is known about dark energy other than its density, and some constraints on the equation of state of dark energy. The term dark energy is a label for a lack of knowledge in the area and there is currently no fundamental understanding of dark energy.

More precise and diverse cosmological measurements are planned for the future, which aim to shed light on the nature of dark energy [5]. For example, the Polarized Radiation Imaging and Spectroscopy Mission (PRISM) is a planned space telescope mission by the European Space Agency [6], which will measure the polarisation of the CMB across the whole sky. Another planned experiment is the Large Synoptic Survey Telescope (LSST), which is a wide-field survey experiment which will observe

the available sky every few nights, and will provide data to study dark energy through observations of BAO, type 1A supernovae and gravitational lensing [7].

In addition to increasingly precise measurements, efforts are being made to discover new physics in cosmology. Dark matter is known to make up 26.8% of the universe, but has yet to be measured through any means other than it's gravitational effect. There are three approaches to discovering more about dark matter: astronomical observation, production at a particle collider and direct detection. The first of these is often model dependent, and involves detecting the gamma rays emitted from the annihilation of dark matter particles [8]. Data analysis from the ATLAS and CMS detectors at the large hadron collider search for missing transverse momenta in collisions, where energy and momentum are carried away by dark matter particles in high energy collisions [9]. There is also a large number of experiments attempting to directly detect the recoil energy from dark matter particles colliding with detectors [10]. None of these searches have yet to have found any convincing signals.

A recent breakthrough in cosmology has been made by advanced LIGO's detection of gravitational waves from the collapse of a binary black hole system [11]. An event with a signal to noise ratio greater than twenty was seen within the first hour of running the two interferometers simultaneously, indicating that a new field of gravitational wave astronomy may be a powerful tool to observe the universe with [12]. This situation will improve in the near future with advanced VIRGO due to be at full sensitivity in 2018 [13], and a third interferometer in the advanced LIGO network is planned to be located India, which will allow sources of gravitational waves to be triangulated. Gravitational waves have opened up a new way to view the universe and are likely to provide key evidence to understanding cosmology.

The subject of this thesis is an experiment proposed by Martin Perl, the late Nobel laureate, as a terrestrial search for dark energy [14]. Whilst the dark energy density is small, it is non-zero at 6.91 $\times 10^{-27}$ kg/m^3, and may be detectable. In comparison, an electric field with the same energy density would be 12 V/m, which is detectable in a lab using a SQUID (super-conducting quantum interference device) [15]. Unlike an electric field, the dark energy field cannot be removed, so there is no way to compare measurements with and without its presence. However, if dark energy has spatial fluctuations, these may be detectable, if they interact with a measurement device in some non-gravitational way.

Whilst the original motivation of the experiment was to detect dark energy terrestrially, anything that meets the criteria above could be detected by the proposed experiment, including any dark contents of the vacuum (DCV). Similarly there could be spatial inhomogeneities in the DCV on the terrestrial scale, which on the cosmological scale would appear homogeneous, much in the way that matter and radiation are inhomogeneous on a terrestrial scale but on a large enough cosmic scale appear

homogeneous. This is illustrated in figure 1.1, with a smooth DCV distribution on the cosmological scale may have fluctuations on the lab scale.

This gives two requirements on any dark contents of the vacuum (DCV) for it to be detectable in the lab:

- The dark contents of the vacuum must be spatially inhomogeneous on the lab scale.
- The dark contents of the vacuum must interact with matter in some non gravitational way.

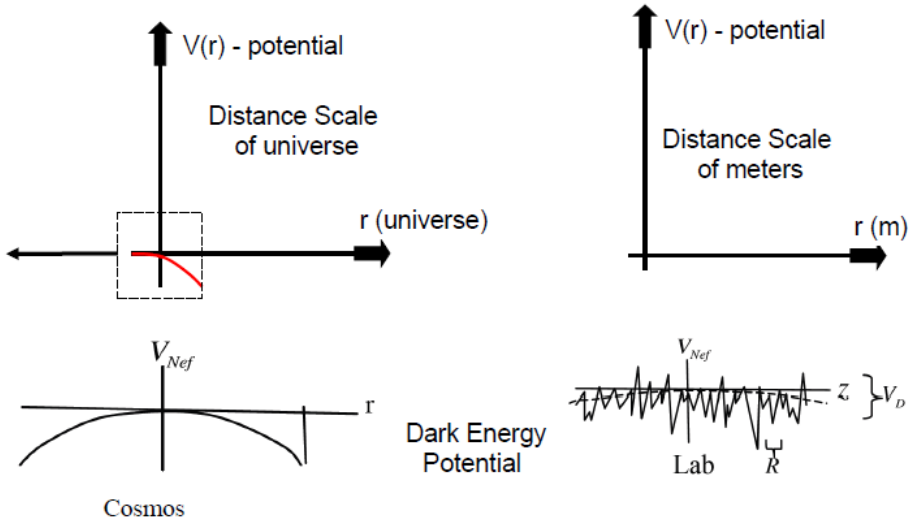

Figure 1.1: Figure illustrating how inhomogeneities on the terrestrial scale can appear homogeneous on the cosmological scale.

Interactions of the DCV with a measurement device may produce detectable forces. The precision these forces can be measured to sets the threshold limit on the detection of the DCV using this method.

1.2 Atom Interferometry

Light pulse atom interferometers are precision devices for measuring forces. The first such device was developed by Kasevich in 1992 [16], and was used to measure the local gravitational force. Since then, atom interferometers have been used in a wide range of precision applications, including gravimeters [17], gyroscopes [18], measurements of fundamental parameters such as Newton's gravitational constant [19] and the fine structure constant [20]. They are also being developed for practical applications such as geophysics [21] and navigation [22].

An atom interferometer can be described in analogy with a light based interferometer, illustrated in figure 1.2. In a Mach-Zehnder interferometer a beam is split into

two, the two beam parts travel down different paths, mirrors cause their trajectories to recombine on another beam-splitter, where the two parts of the beam interfere. The beam interference depends on differences between the two beam paths. In a light interferometer, laser beams are interfered, in an atom interferometer, it is the atoms' wave-like behaviour that interferes.

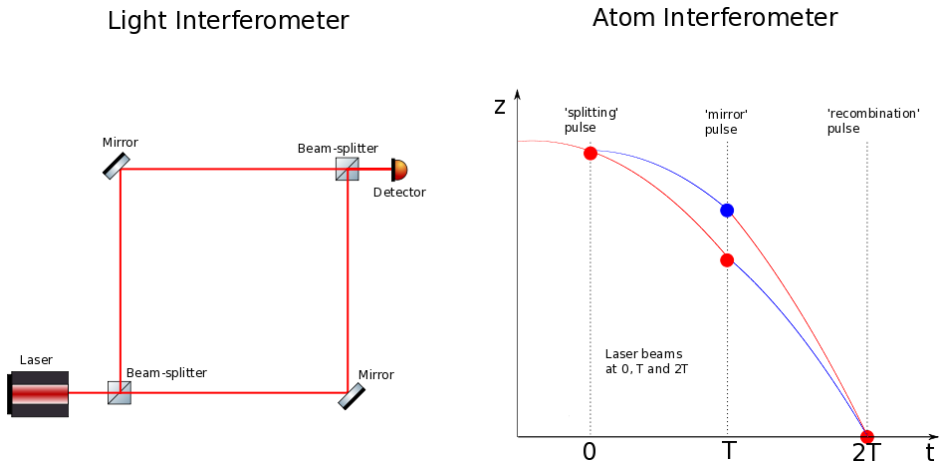

Figure 1.2: Figure illustrating the analogy between a light and an atom interferometer. On the left a sketch of an Mach-Zehnder light interferometer and on the right, a sketch of the paths taken by atoms in an atom interferometer as they interact with lasers beams. Three laser pulses at T = 0, T and 2T, which 'splits' the atomic wave-packet into a superposition, 'mirror' the atomic states, and 'recombine' the atoms, where the interference is detected.[14].

Laser pulses stimulate transitions between two states of the atoms. Pulses that split the atoms into a superposition of the two states are 'beam-splitters' and pulses that reverse the state population are 'mirrors' for an atom interferometer. The transition from one state to another is accompanied with a momenta transfer, so when atoms are put into a super-position of two states, the two parts of the superposition have different momentum and begin to spatially separate.

In this work, stimulated Raman transitions transfer atoms between the two states. Raman transitions are two photon transitions via a virtual state [23]. The Raman transitions create Rabi cycles in which the atoms are all transferred from one state to the other state and back in a full cycle (2π) [24]. The 'beam-splitter' Raman transitions are a quarter of this cycle ($\frac{\pi}{2}$ pulses), and the 'mirror' pulses are half of this cycle (π pulses).

For an atom interferometer to function, the lifetime of the states used need to be long compared to the interferometry time, which can be up to the order of seconds. Ground states of atoms with hyperfine splitting are suitable candidates for atom interferometry. The steps to an atom interferometer are illustrated in figure 1.3, with red and blue denoting atoms in the different hyperfine split ground states, and are as follows:

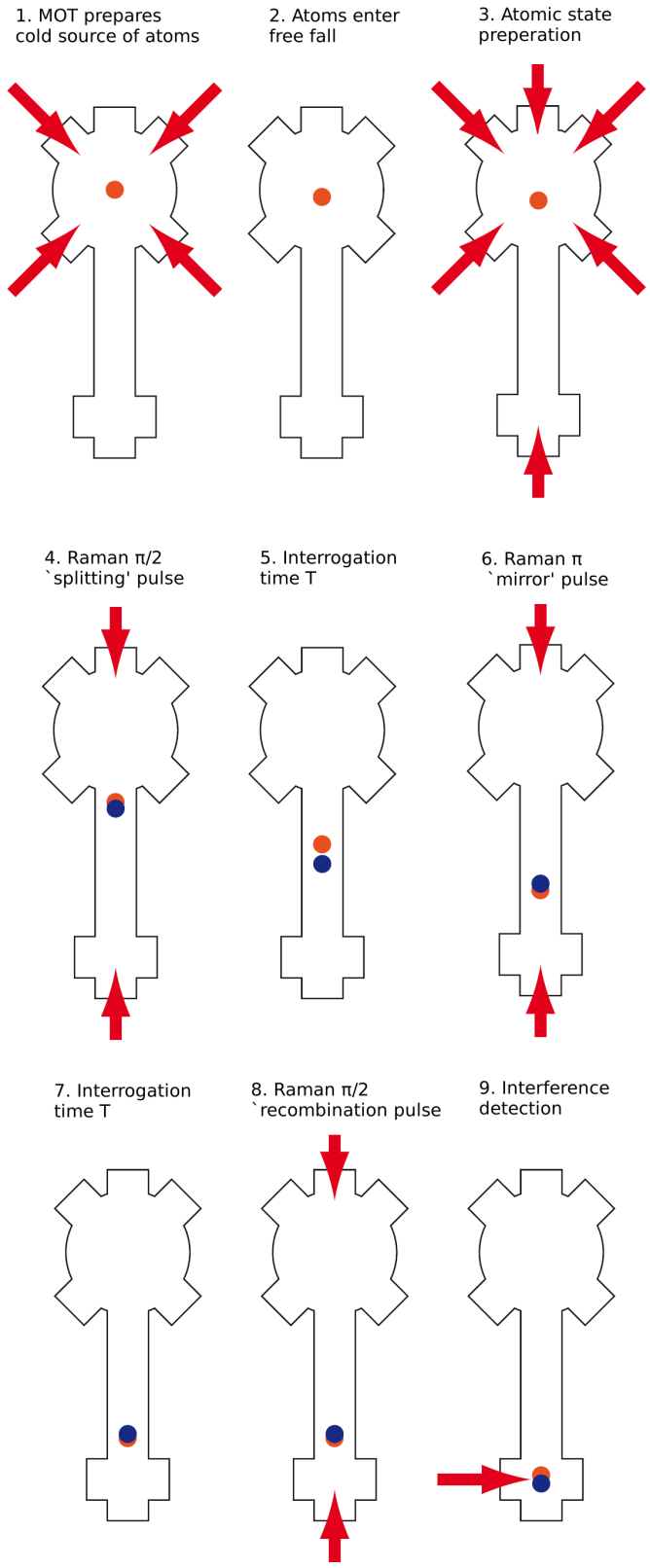

Figure 1.3: The diagram illustrates the steps to an atom interferometer. Blue and red atoms represent atoms in different atomic states. Arrows represent laser beams. [25]

1. **Prepare cold source of atoms.** The interferometer requires cold atoms, so they do not escape the confines of the laser beams during the interferometry. With beams of order a centimetre, and the time scale of the interferometry being of order a second, the atoms must have a thermal velocity of about one centimetre per second, which is at the micro-Kelvin temperature scale. This is achieved using laser cooling techniques. First a magneto-optical trap (MOT) laser cools and traps a cold source of atoms. Using this technique the atoms are lowered to approximately hundred micro-Kelvin [26]. Further cooling is implemented in an optical molasses stage, utilising polarisation gradient cooling to lower the temperature of the atoms to the micro-Kelvin level [27].

2. **Atoms enter free fall.** The atoms are released from the optical molasses, and start to free fall under gravitational acceleration.

3. **State preparation.** All the atoms are in the same ground state after the release from the optical molasses, but are distributed amongst the magnetic sub-states. The atoms are optically pumped into the magnetically insensitive $m_F = 0$ Zeeman sub-state, to minimise the effect that magnetic fields have on the atoms. Additionally a 1-D velocity sub-selection is applied in the interferometry axis. The 1-D velocity profile of the remaining atoms is of order ten nano-Kelvin [24]. This velocity selection increases the contrast in the interferometer fringes by minimising the Doppler shift effect across the velocity profile.

4. **Raman $\frac{\pi}{2}$ 'beam-splitter' pulse.** This is the first laser pulse of the interferometry sequence. Counter-propagating laser beams stimulate a Raman $\frac{\pi}{2}$ pulse, putting the atoms into a super-position of the two ground states. The part of the wave-function that is transferred into the other ground state receives a momentum kick.

5. **Interrogation time T.** The two parts of the wave-function have different momenta and start to spatially separate for time T.

6. **Raman π 'mirror' pulse.** A Raman π pulse is applied to the atoms, reversing the wave-function, and giving both parts of wave-function a momentum kick in opposite directions.

   Since the first Raman pulse, the atoms have accelerated under gravity, increasing their speed by gT. As such the frequencies of the Raman beams have to be adjusted so they are in resonance with the atoms. This alteration of the frequencies is done continuously throughout the interferometry sequence, linearly increasing the frequency at rate, and is called the chirp rate.

7. **Interrogation time** T The two parts of the wave-function propagate for a time T, where at time $2T$ they are once again at the same point in space.

8. **Raman $\frac{\pi}{2}$ 'beam-splitter' recombination pulse.** The final $\frac{\pi}{2}$ Raman pulse is applied, transferring the atoms into the same state. However the two parts of the wave-function have travelled different paths, and experienced different phases from the laser beams. The phase difference between the two paths is $\Delta\phi = k_{eff}gT^2 + \phi_{laser}$. The parameter k_{eff} is the momentum transferred by the Raman lasers pulses, g is the gravitational acceleration and ϕ_{lasers} a systematic controllable phase of the lasers.

9. **Interference detection.** The fraction of the atoms in the initial ground state, P_{g_1}, is now detected, determined by the phase difference between the wave-packets that travelled different paths. This is related to the phase on the lasers by $P_{g_1} = \frac{1}{2}(1 + Ccos(\Delta\phi))$, where C is the contrast of the atomic fringes [25].

   Atomic fringes can be traced out by varying the chirp rate of the Raman beams, illustrated in figure 1.4. If the chirp rate does not cancel the Doppler shift, the π and $\frac{\pi}{2}$ pulses are no longer the correct fraction of the Rabi cycle, giving a periodic phase difference. Doing this for multiple times T, fringes of different frequency are traced out. For the chirp rate which exactly cancels the Doppler shift due to the gravitational acceleration, all of the atomic fringes will have a maximum at the same chirp rate. This method allows the chirp rate which cancels the Doppler shift to be measured. The gravitational acceleration may be calculated from this chirp rate from the Doppler shift $\frac{df}{dt} = 2f_0\frac{g}{c}$, where f_0 is the frequency difference required to drive the Raman transitions for stationary atoms.

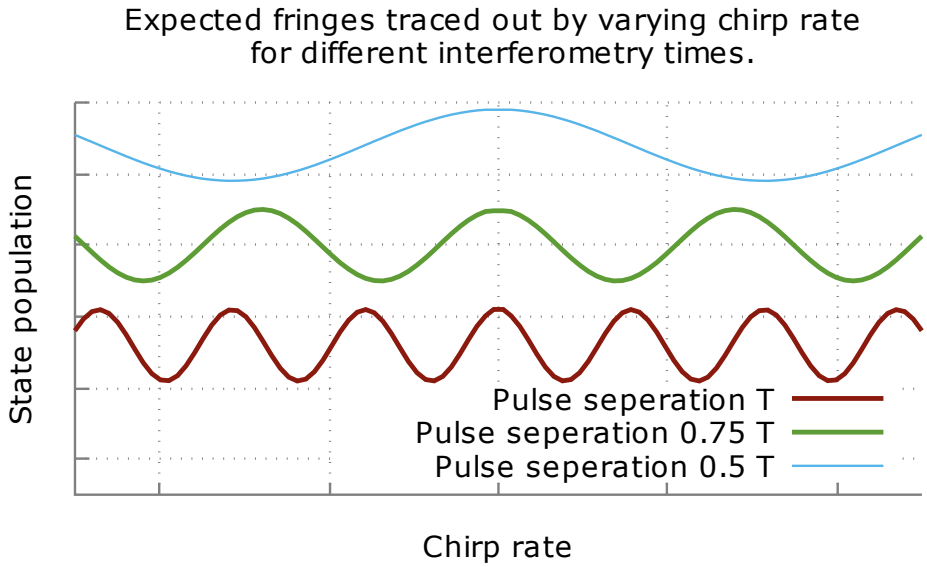

Figure 1.4: An illustration of the expected fringes from an interferometer, when varying the chirp rate for different interferometer times T

Implementing the above techniques demands several technical challenges. A sophisticated laser system is required to generate all of the frequencies required to manipulate the atoms in the interferometer. In particular, the Raman laser system is required to have a controlled phase relationship between the two lasers and low phase noise. Laser beams need to be delivered into the experimental chamber, with the precisely controlled polarisation and alignment via the experiments optical system. The experimental chamber itself needs to be at ultra-high vacuum to reduce warm gas molecules colliding with the carefully prepared atoms. Whilst reducing background gases in the experimental chamber, the atoms required for the interferometer must be introduced into the chamber. Finally several techniques used require the generation of magnetic fields (via electromagnets). These will be discussed in the contents of this thesis.

1.3 Proposed Experiment

Atomic interferometer gravimeters of length one metre have demonstrated a long term measurement of g to 10^{-10} g [17], with single shot measurements demonstrating precision of 6.7×10^{-12} g [28]. If two atom interferometers were in the same noise envelope, but spatially separated, making simultaneous measurements, they should measure the same phase difference, $\Delta\phi_A$ and $\Delta\phi_B$ (if the influence of gravity was the same on both devices). In this situation subtracting the two phase differences gives the signal,

$$\Delta\Phi = \Delta(\Delta\phi) = \Delta\phi_A - \Delta\phi_B. \tag{1.1}$$

If the two interferometers are truly in the same noise conditions, this value will be zero. However, if a force due to DCV is acting on one interferometer and not the other, this would effect the difference in phase differences, and $\Delta\Phi \neq 0$. This is illustrated in figure 1.5. If the DCV is what manifests as dark energy on a cosmological scale, it can be expected to be moving with respect to the experiment, as the experiment is not in an inertial frame. The Earth is in motion with respect to the cosmic microwave background at around 400 km/s. As such, the interferometers are going to be averaging the effect of any DCV that it sweeps through in the time it takes to make a measurement, and the signal will be noise like in nature. As such the RMS of $\Delta\Phi$ will be analysed for anomalous noise (the RMS will be taken because $\Delta\Phi$ can be both negative or positive).

With both interferometer in the same noise envelope, subtracting the measurements should cancel common noise. Two main sources of noise on an atom interferometer are vibrational noise, and phase noise on the Raman beams [29]. Two interferometers will share common vibrations if mounted on the same optical table, and will share common phase noise if they employ the same laser beam.

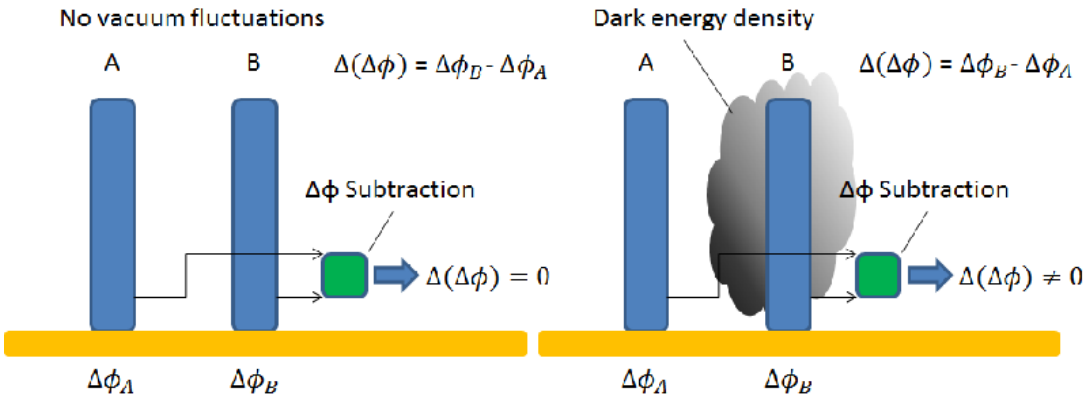

Figure 1.5: On the left, two atom interferometers measure the same phase difference, so $\Delta\Phi = 0$. On the right, there is some dark content in interferometer B, resulting in a non-zero signal. $\Delta\Phi \neq 0$.

Chapter 2

Atom Interferometry Theory

This chapter introduces the theory necessary to make a measurement of the local gravitational field strength. The theory presented here is based on a path integral approach [30], but there are other methods, such as Bordé's 5-D optics technique [31], [32]. The key points to the method are introduced, applied to a particle in gravitational field. Light interactions are introduced and combined with a particle in a gravitational field to calculate the interference between particles that travel along different paths in a Mach-Zehnder interferometer. The limitations of the theory described are discussed. The final section of this chapter is describing a parametrisation of the DCV, and a discussion of the proposed experiments sensitivity to this.

2.1 Path Integral Approach to Atom Interferometry

The physics of an atomic interferometer is very close to the classical limit; the action is much larger than $\hbar$ and small variations from the classical path result in destructive interference. In a Mach-Zehnder atom interferometer, the two super-positions of the atoms travel along the classical paths to be recombined at the end of the interferometer. This makes a path integral approach appropriate as the calculation is reduced to calculating the integrals along the classical paths. The approach presented here is based on the paper by Storey and Cohen-Tannoudji in [30], for systems described by quadratic Lagrangians.

The wave-function of a particle that propagated from position z_a at time t_a to the coordinates $z_b t_b$ is given by

$$\psi(z_b, t_b) = \int dz_a K(z_b t_b, z_a t_a) \psi(z_a, t_a) \tag{2.1}$$

where $\psi(z_a, t_a)$ is the initial wave-function, and $K(z_b t_b, z_a t_a)$ is the propagation operator. The propagation operator comprises of a term $F(z_b, t_b)$, which is the functional integral over all possible paths between point z_a and z_b and a phase factor representing the phase accumulated by the atoms whilst propagating. The case of quadratic

Lagrangians has a simplified solution, where the functional integral only affects the amplitude of the $\psi(z_b, t_b)$, and does not effect the phase on the atoms [30]. The propagation operator is given by

$$K(z_b t_b, z_a t_a) = F(t_b, t_a) exp^{\left\{\frac{i}{\hbar} S_{cl}(z_b t_a, z_a t_a)\right\}}. \tag{2.2}$$

The phase factor is dependent on the action, S_{cl}, which is calculated along the classical trajectory the particle would take,

$$S_{cl} = \int_{t_b}^{t_a} dt L[z(t), \dot{z})], \tag{2.3}$$

where $L[z(t), \dot{z})]$ is the Lagrangian. As the action is much larger than $\hbar$, the stationary phase approximation means that only the classical trajectories taken by the atoms and only the starting position contributes to the integral over z_a in equation 2.1.

The phase of the atoms at z_b, t_b is given by the phase of the initial wave-function and the phase accumulated by the atoms due to the action. Typically the atom's initial wave-function will be a plane wave, as they can suitably be modelled as free particles.

2.2 Applied Path Integrals

This section applies the path integral formalisation to a particle in a gravitational field, introducing light interactions for a two level atom and combines these two results to apply it to a Mach Zehnder atom interferometer.

2.2.1 Classical action for particle in a gravitational field

In the interferometer, the atoms free fall through the vacuum. Consider a particle mass M in a gravitational field strength g, moving in only the vertical axis, z. The Lagrangian is

$$L(z, \dot{z}) = \frac{1}{2} M \dot{z}^2 - Mgz. \tag{2.4}$$

The classical paths velocity and position is,

$$v(t) = v_a - g(t - t_a), \tag{2.5}$$

and

$$z(t) = z_a + v_a(t - t_a) - \frac{1}{2} g(t - t_a)^2. \tag{2.6}$$

At the final time, t_b, this gives

$$v_a = \frac{z_b - z_a}{t_b - t_a} + \frac{1}{2} g(t_b - t_a), \tag{2.7}$$

which can be used to show that the action along the classical path is

$$
\begin{aligned}
S_{cl}(z_b t_b, z_a t_a) &= \int_{t_a}^{t_b} \mathrm{d}t[\frac{1}{2}M\dot{z}^2 - Mgz] \\
&= \frac{M}{2}\frac{(z_b - z_a)^2}{(t_b - t_a)} - \frac{Mg}{2}(z_b + z_a)(t_b - t_a) - \frac{Mg^2}{24}(t_b - t_a)^3
\end{aligned}
\tag{2.8}
$$

The phase accumulated along the classical path is given by $\frac{i}{\hbar}S_{cl}$. This result can be used to calculate the phase accumulated in the action for a particle in a uniform gravitational field, such as the particles in the interferometer.

2.2.2 A two level atom crossing a travelling laser wave

In the interferometer, stimulated Raman transitions transfer the atoms between the two ground states, labelled here as α and β. This section discusses the phase difference accumulated from an interaction at a space-time point of $z_1 t_1$. The atom is assumed to have well defined momentum, and internal state, α or β. There are four possible interactions that can occur, summarised in figure 2.1 [33] [34] [35]. The effect of the laser interaction changes the atoms wave-function, depending on the initial and final states with one of these four factors:

$$
\begin{aligned}
U_{\beta\alpha} exp^{\{i(k_L z_1 - \omega_L t_1 - \phi)\}} (\alpha \to \beta) \\
U_{\alpha\beta} exp^{\{-i(k_L z_1 - \omega_L t_1 - \phi)\}} (\beta \to \alpha) \\
U_{\alpha\alpha}(\alpha \to \alpha) \\
U_{\beta\beta}(\beta \to \beta).
\end{aligned}
\tag{2.9}
$$

These correspond to a photon being absorbed by an atom, which gains momentum $\hbar k_L$ and is transferred from state α to state β, a photon being emitted by an atom, which loses momentum $\hbar k_L$ and is transferred from state β to state α, an atom that remains in state α and finally an atom that remains in state β respectively. Parameters k_L, ω_L and ϕ are the wave-number, frequency and phase respectively of the laser. U_{ij} is the transition amplitude from internal state j to state i. The exponential factors $exp\{\pm ik_L z_1\}$ correspond with a change of momentum $\pm\hbar k_L$ in the laser propagation axis.

An example can be seen in figure 2.2, where a particle in internal state α was to travel from $z_0 t_0$ to $z_1 t_1$, where it interacts with a laser, transferring into state β. It then propagates to $z_2 t_2$. At $z_2 t_2$ the wave-function is $\phi_B(z_2, t_2)$ is the product of the initial wave-function, a phase shift due to the free propagation before the interaction, a factor due to the laser interaction, and a phase shift due to free propagation after the interaction. The result is

$$
\begin{aligned}
\psi_\beta(z_2, t_2) = exp^{\{iS_{cl}(z_2 t_2, z_1 t_1)/\hbar\}} U_{\beta\alpha} exp^{\{i(k_L z_1 - \omega_L t_1 - \phi)\}} \\
\times exp^{\{iS_{cl}(z_1 t_1, z_0 t_0)/\hbar\}} \psi_\alpha(z_0, t_0).
\end{aligned}
\tag{2.10}
$$

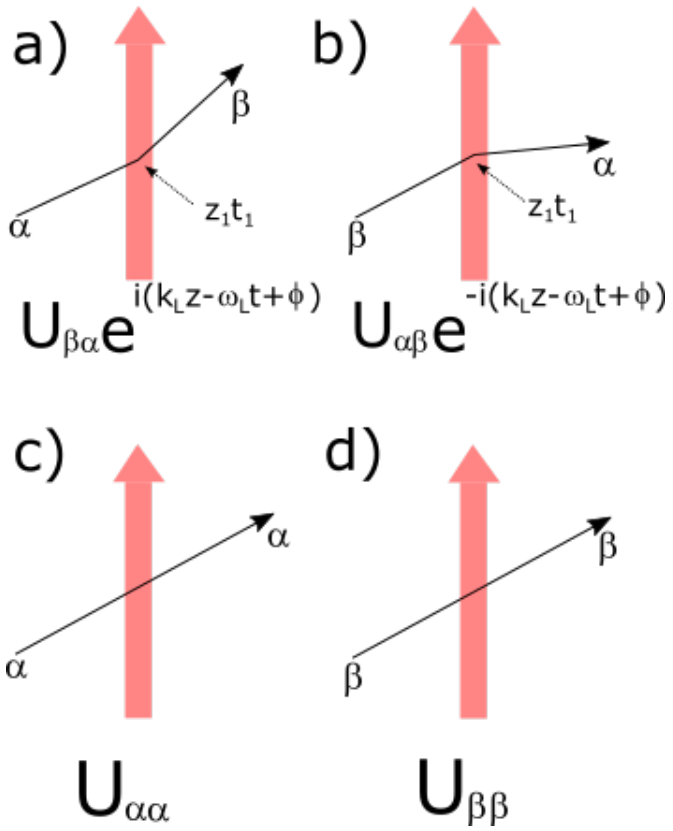

Figure 2.1: The four different possible interactions for a travelling laser wave and a two level atom: (a) atom absorbs a photon gaining momentum $\hbar k_L$ and is transferred from state α to state β, (b) atom emits a photon losing momentum $\hbar k_L$ and is transferred from state β to state α, (c) atom remains in state α, (d) atom remains in state β [30].

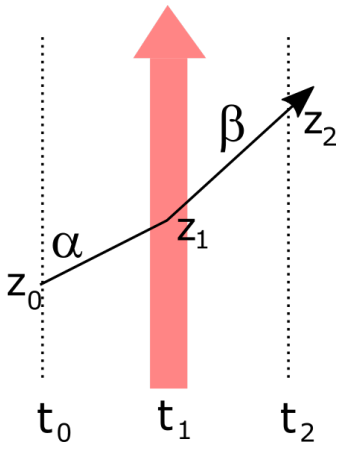

Figure 2.2: An example of a particle propagation with a laser interaction [30].

These rules are applied in section 2.2.3 to calculate the phase difference from the laser interactions in a Mach-Zehnder atom interferometer.

2.2.3 Evolution of phase for a particle in an atom interferometer

Atoms are transferred between the two internal hyperfine ground states of an atom, which will be referred to as g_1 and g_2, using stimulated Raman transitions. Three pulses are applied to separate the atomic wave-packet into two coherent parts and recombine them. This is achieved with three Raman pulses, delivered by two vertical counter-propagating laser beams, with wave-numbers, frequencies and phases k_i, ω_i and ϕ_i. The subscript $i = 1, 2$ to denote the two different beams.

Contributions to the phase come from the phase accumulated by the action, and that imparted to the atoms by the laser interactions. The contribution from the action can be calculated along the classical paths of the atoms.

The first pulse, at $t = 0$, is a $\frac{\pi}{2}$ pulse, which splits the wave-packet into two components with momentum difference $\hbar(k_1 - k_2)$. The second pulse, at $t = T$ is a π pulse and reverses the momentum and internal states of the two components of the wave-packet. Finally, at $t = 2T$, the two components spatially overlap and another $\frac{\pi}{2}$ recombines them coherently. The classical space-time paths can be seen in figure 2.3

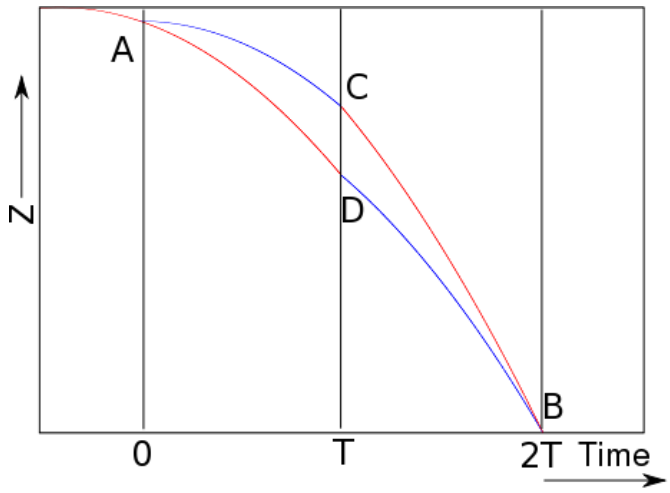

Figure 2.3: Classical paths of the atoms in the interferometry sequence. Red paths represent the first ground state, blue paths represent the second.

The phase due to the action, $\delta\phi^{prop}$ is the difference between the actions for the two classical paths.

$$\delta\phi^{prop} = S_{cl}(AC) + S_{cl}(CB) - [S_{cl}(AD) + S_{cl}(DB)] \tag{2.11}$$

From equation 2.8, the action along one path is (the third term in 2.8 is proportional to the time difference cubed, which is constant and therefore cancels),

$$S_{cl}(AC) - S_{cl}(AD) = \frac{M}{2T}\{(z_C - z_A)^2 - (z_D - z_A)^2 - gT^2[(z_C + z_A) - (z_D + z_A)]\}$$
$$= \frac{M}{2T}(z_C - z_D)(z_C + z_D - 2z_A - gT^2). \tag{2.12}$$

Similarly,

$$S_{cl}(CB) - S_{cl}(DB) = \frac{M}{2T}(z_C - z_D)(z_C + z_D - 2z_B - gT^2). \tag{2.13}$$

So

$$\delta\phi^{prop} = \frac{M}{T}(z_C - z_D)(z_C + z_D - z_A - z_B - gT^2). \tag{2.14}$$

It can be shown using equation 2.6 that

$$z_C + z_D - z_A - Z_B - gT^2 = 0. \tag{2.15}$$

This nulls the second parenthesis, thus

$$\delta\phi^{prop} = 0. \tag{2.16}$$

The stimulated Raman transitions affect the phase, with the following effective parameters:

$$k_{eff} = k_1 - k_2, \omega_{eff} = \omega_1 - \omega_2, \phi_{eff} = \phi_1 - \phi_2. \tag{2.17}$$

The contribution from path ACB is

$$U^{(3)}_{g_2g_2} U^{(2)}_{g_2g_1} exp^{\{i[k_{eff}z_C - \omega_{eff}T - \phi_{II}]\}} U^{(1)}_{g_1g_1}. \tag{2.18}$$

Along the path ADB the contribution is

$$\begin{aligned} &U^{(3)}_{g_2g_1} exp^{\{i[k_{eff}z_B - 2\omega_{eff}T - \phi_{III}]\}} \\ \times &U^{(2)}_{g_1g_2} exp^{\{-i[k_{eff}z_D - \omega_{eff}T - \phi_{II}]\}} \\ &\times U^{(1)}_{g_2g_1} exp^{\{i[k_{eff}z_A - \phi_I]\}}. \end{aligned} \tag{2.19}$$

where $U^{(1)}$, $U^{(2)}$ and $U^{(3)}$ are the transition amplitudes at t = 0, T and 2T respectively, and ϕ_I, ϕ_{II} and ϕ_{III} are the values of ϕ_{eff} at these times.

The phase difference between the two arms of the interferometer is just the phase difference due to the laser interactions, which is

$$\delta\phi^{laser} = \delta\phi^{tot} = k_{eff}gT^2 + \phi_I + \phi_{III} - 2\phi_{II}, \tag{2.20}$$

The wave-functions of the two possible routes of the particles will interfere. The superposition of the wave-function of the two paths, $|\psi_{g_1}>$ is

$$|\psi_{g_1}>=|ACB>+|ADB>, \tag{2.21}$$

where $|ACB>$ and $|ADB>$ are the wave-functions for the paths ACB and ADB respectively. Both paths originate from the wave-function (modelled by a plane wave), so the only contribution to phase is from the Raman transitions. Thus the wave functions can be summarised to

$$\begin{aligned} |ACB>&=N_1 exp^{\{i[k_{eff}z_C-\omega_{eff}T-\phi_{II}]\}} \\ |ADB>&=N_2 exp^{\{i[k_{eff}(z_B+z_A-z_D)-\omega_{eff}T-\phi_I-\phi_{III}+\phi_{II}]\}} \end{aligned} \tag{2.22}$$

where N_1 and N_2 are amplitudes. The probability of the particle being measured in ground state g_1 is

$$\begin{aligned} &=<\psi_{g_1}|\psi_{g_1}> \\ &=<ACB|ACB>+<ADB|ADB>+<ACB|ADB>+<ADB|ACB> \\ &=|N_1|^2+|N_2|^2+N_1^*N_2 exp^{\{i[k_{eff}(z_B+z_A-z_D-z_C)-\phi_I-\phi_{III}+2\phi_{II}]\}} \\ &+N_1N_2^* exp^{\{-i[k_{eff}(z_B+z_A-z_D-z_C)-\phi_I-\phi_{III}+2\phi_{II}]\}} \\ &=|N_1|^2(2+exp^{\{i[k_{eff}(z_B+z_A-z_D-z_C)-\phi_I-\phi_{III}+2\phi_{II}]\}} \\ &+exp^{\{-i[k_{eff}(z_B+z_A-z_D-z_C)-\phi_I-\phi_{III}+2\phi_{II}]\}}). \end{aligned} \tag{2.23}$$

With ideal Raman pulses, the chance of the particle travelling either path should be equal so $N_1=N_2$. Using this and equation 2.15,

$$<\psi_{g_1}|\psi_{g_1}>=2N_1^2(1+\cos(k_{eff}gT^2+\phi_I+\phi_{III}-2\phi_{II})) \tag{2.24}$$

If the Raman laser phase is known, the population ratio of atoms in state g_1 to total particles can be related to the gravitational acceleration along the axis of k_{eff}. The maximal population ratio is unity, so

$$P_{g_1}=\frac{1}{2}(1+\cos(k_{eff}gT^2+\phi_I+\phi_{III}-2\phi_{II})). \tag{2.25}$$

For any population ratio measurement, there are multiple solutions for g. The phase difference for a 1 second interferometry sequence is $k_{eff}gT^2\simeq 1.58\times 10^6$, which is many times 2π. The consequence is that a measurement of the gravitational field strength cannot be made from a single population measurement. This ambiguity can be resolved as discussed in section 1.2.

The precision of the phase difference measurement is proportional to T^2, so the precision of the device is proportional to the length of the interferometer.

2.3 Discussion of limitations

In the theory presented, simplifications of the physics were made. For example, the Lagrangian assumes a constant gravitational acceleration over the height of the interferometer, and the laser interactions are assumed to be instantaneous as opposed to finite in length. The experiment is also assumed to be in an inertial frame.

2.3.1 Non uniform gravitational acceleration

One assumption made was that the gravitational acceleration is constant along the length of the interferometer. There would be a gravity gradient over the height of the interferometer. Atoms on the higher path experience a smaller gravitational acceleration than the atoms on a lower path. The result is that the paths do not perfectly recombine at the bottom of the interferometer. The atoms still interfere though, as the wave-packets are spatially extended. However there is an associated phase difference with this separation of

$$\Delta\phi_{sep} = \frac{1}{2\hbar} p.(\Delta x_B), \tag{2.26}$$

where p is the the mean momentum of the two wave-packets and Δx_B is the separation between the two wave-packets [36] [35]. This is of order a thousand radians, and is a systematic shift depending on the gravity gradients in the laboratory.

2.3.2 Finite Length Raman Pulses

The calculation presented assumed that the Raman light interactions are instantaneous. In reality they last a duration of tens of microseconds. A more accurate calculation that that presented can be seen in [37]. The correction to the phase is

$$\Delta\phi = \delta\phi^{tot} = k_{eff} g T(T + 2\tau) + \phi_I + \phi_{III} - 2\phi_{II}, \tag{2.27}$$

where 2τ is the length of a π pulse. With Raman pulse of the order a microsecond, the phase difference is of order one radian.

2.3.3 Coriolis Effect

The experiment is on the Earth's surface, which is a non-inertial frame. A phase difference emerges in the action of a particle free falling in a rotating frame. This can be seen in [30] and [38], and is given by

$$\Delta\phi_{rot} = -2\Omega\Delta v_{EW} k_{eff} T^2 \cos(\theta_{lat}), \tag{2.28}$$

where Ω is the angular velocity of the Earth, which is $7.29 \times 10^{-5} rad/s$, Δv_{EW} is the velocity difference between the higher and lower paths in the interferometer,

going east to west, and latitude θ_{lat}, which is 53.40° in Liverpool. This will be a very small phase difference shift in the prototype, but in a conjugate pair of interferometers could be significant, depending on the configuration (i.e. if the two interferometers are separated vertically or horizontally).

2.4 Parametrisation of the DCV

Martin Perl *et al.* presented a parametrisation of the DCV based on assumptions that terrestrial scale fluctuations in the DCV behave as dark energy on the cosmological scale [14]. That parametrisation is as follows. Variations of the dark contents of the vacuum can be expressed as a potential written in it's Fourier components,

$$U(X) = \mathrm{Re} \int_0^\infty mu'(k)e^{ikX}dk, \tag{2.29}$$

where m is the mass of the test particle, $u'(k)$ is amplitude of the Fourier coefficient, X is a position and k is the wave-number. The Re denotes it is the real part, which will be taken as implied from now on. Also $U(X)$ will be restricted to one Fourier component $u(k)$. Whilst it is unknown what the interaction is, it is expected to be proportional to mass (e.g. baryon number is proportional to mass). This model can be consistent with current cosmology, with a suitable low frequency cut-off (long wavelength), the current constant dark energy density on the cosmological scale can be recovered.

Any dark contents of the vacuum (DCV) are unlikely to be at rest relative to the Earth. If there is a rest frame it is likely to that of the CMB, which moves at 369 km/s relative to Earth. If the Earth moves through this frame with velocity v, then $X = x - vt$, so

$$U(x) = mu(k)e^{i(kx-\omega_k t)} \tag{2.30}$$

where $\omega_k = kv$. An approximation can be made if the apparatus is assumed to be much smaller than $1/k$ to obtain,

$$U(x) = mu(k)e^{ikx} \approx mu(k)e^{ikx}[1 + ik(x - x_0) - \frac{1}{2}k^2(x - x_0)^2], \tag{2.31}$$

where x_0 is the lowest point of the interferometer. The constant term has spatial dependence and will cancelled out over the two paths the atoms take in the interferometer. The classical paths are

$$x_1(t) = \begin{cases} (v_i + v_r)t - \frac{1}{2}gt^2 & t < T, \\ v_r T + v_i t - \frac{1}{2}gt^2 & t > T \end{cases} \tag{2.32}$$

and

$$x_2(t) = \begin{cases} v_i t - \frac{1}{2}gt^2 & t < T, \\ v_r(t-T) + v_i t - \frac{1}{2}gt^2 & t > T, \end{cases} \tag{2.33}$$

where v_i is the initial velocity of the atom and v_r is the recoil velocity. For the paths, the phase difference is given by the difference in action between the two paths,

$$\phi = \frac{1}{\hbar}(\int_{Path_1} U(x,t)dt - \int_{Path_2} U(x,t)dt). \tag{2.34}$$

For two interferometers, the difference in the phase differences is

$$\Delta\Phi = -4\frac{L}{v}\frac{v_r}{v}\frac{mu(k)}{\hbar}\sin^2(\frac{kvT}{2})\cos(\omega_k t_0). \tag{2.35}$$

In this equation, t_0 is the time when the central interferometer pulse is applied. L is the separation between the two interferometers. The recoil velocity of the atoms is related to the momenta transferred by the Raman pulses, giving $v_r = n\hbar k_{opt}/m$, where n is the number of photon momenta transferred by the beam-splitter, and k_{opt} is the laser wave-number, which can be substituted in

$$\Delta\Phi = -4\frac{L}{v}\frac{nk_{opt}}{v}u(k)\sin^2(\frac{kvT}{2})\cos(\omega_k t_0). \tag{2.36}$$

Note that $u(k)k \equiv a(k)$, which is the acceleration at x_0 of the test particle due to the DCV, hence

$$\Delta\Phi = -4\frac{Lnk_{opt}a(k)}{v\omega_k}\sin^2(\frac{kvT}{2})\cos(\omega_k t_0). \tag{2.37}$$

2.4.1 Application to Dark Energy's Parameters

The precision to which $\Delta\Phi$ can be measured to is limited by the precision resolved by the two individual interferometers. If the interferometers can reach a precision of $\sigma_{\Delta\phi}$, then deviations in $\Delta\Phi$ exceeding this would be indications of DCV interacting with the atoms. These deviations would have to pass statistical analysis, passing the traditional three standard deviations for an indication of new physics and five standard deviations for a discovery.

Examining equation 2.37 shows that the size of signal from DCV fluctuations can be increased by increasing the separation of the two interferometers, L. Initially after commissioning one atom interferometer, techniques such as Ramsey-Bordé interferometry pulse sequences or juggling techniques could be used to create a conjugate pair of interferometers. A Ramsey-Bordé interferometer has a pulse sequence of four $\frac{\pi}{2}$ pulses separated by T, T' and then T, and is illustrated in figure 2.4, where two interferometry diamonds can be seen. A conjugate pair of interferometers is created, and separations of 350 μm on a 1 m device have been shown [39].

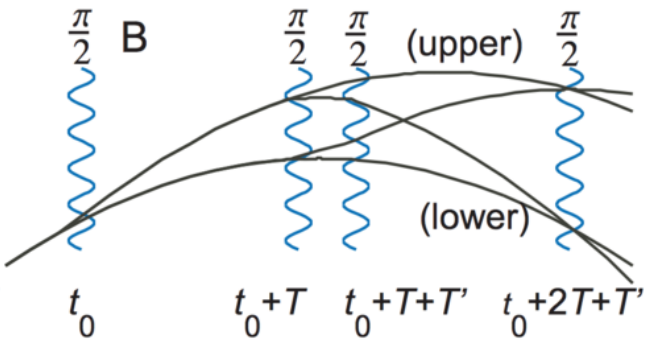

Figure 2.4: Figure illustrating a Ramsey-Bordé interferometer [39].

Juggling can be used in atomic fountain interferometers, where two clouds of atoms launched to different heights, carefully timed so they reach the apex of their trajectories at the same time. This makes full use of the interferometry pipe, allowing T to be twice as long. A conjugate pair can be created by launching two clouds to different heights, and has achieved a separation of 35 cm in a 1 m device [40]. Separations larger than this could be achieved by building two interferometers. Keeping them in the same mechanical noise envelope would become increasingly difficult, the larger the separation. Larger separations would require lower frequency noise control which is difficult to isolate from, due to it's sources being from seismic motion.

Larger momenta transfer by the interferometry pulses would also increase the size of the signal. The Raman pulse interferometer describe in this work transfers two photon momenta, but multi-photon Bragg pulses have been used to transfer 102 $\hbar k$ in the interferometer pulses [41].

Increasing the precision $\Delta\Phi$ can be measured to increases the sensitivity to small accelerations. The precision $\Delta\phi$ can be measured to is given by the precision of the individual interferometers. Interferometers can operate at the shot noise limit, where the error is limited by the counting statistics on the number of atoms [42]. Therefore, increasing the number of atoms in the interferometer increases the phase difference measurement precision. Techniques such as spin state squeezing uses entanglement to allow measurements beyond these limits [43].

The signal $\Delta\Phi$ is dependent the length of time T, which changes the periodicity of the sine function. The maximum value of T is fixed by the length of the interferometer, but short times can be used. Devices with a 1 m height are common [44] [45] with $T = 260\ ms$. These devices typically measure with milli-radian precision. 10 m interferometers being developed [46] [47] with have a time $T = 1.42\ s$, and have precision approaching micro-radians.

Figure 2.5 is a graph of the acceleration caused by the DCV for a specific Fourier component of the fluctuations ω_k. The curves are for $\Delta\Phi$ signal of 1 $mrad$ for a pair of

1 m interferometers in the red curve, and for a $\Delta\Phi$ signal of 1 μrad for a pair of 10 m interferometers in the green. Both curves are for rubidium interferometers, separated by 1 m, with momenta transfer $n = 2$, moving with respect to the DCV at 369 km/s. The variable t_0 is set to zero for maximal signal.

The area above these curves would create a $\Delta\Phi$ signal larger than the input precision of the devices, and would be detectable. Increasing L, n or decreasing the precision $\Delta\Phi$ measurement would lower these curves. These curves are only an indication of what accelerations may be detectable. This treatment has only been for one Fourier mode, and sensitivity of the measurement would have to be integrated over all acceleration components. Additionally, the DCV may not share an inertial frame with the CMB.

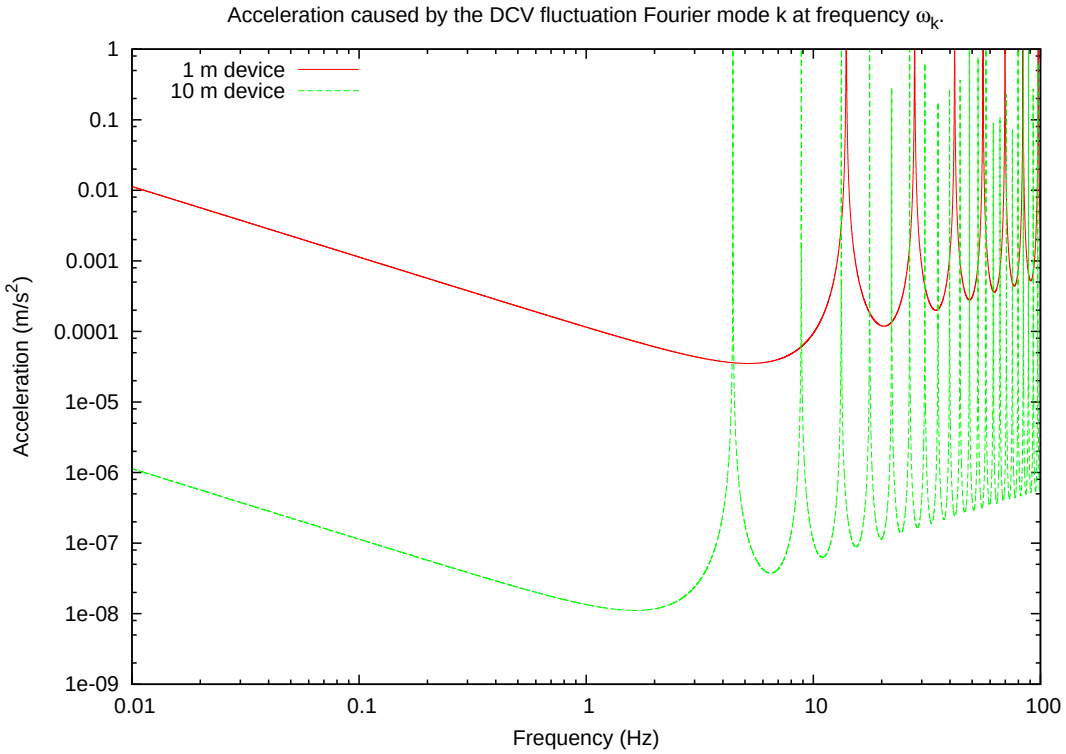

Figure 2.5: Plot of sensitivity to acceleration caused by DCV against frequency. Both curves are for Rubidium interferometers, with a 1 m separation, momentum transfer of $n = 2$, moving with respect to the DCV at 369 km/s and $t_0 = 0$. The red curve is for pair of 1 m devices measuring phase differences of $1 \times 10^{-3} rad$, and the green curve is for 10 m devices measuring phase differences of $1 \times 10^{-6} rad$

Chapter 3

Magneto-Optical Trap

The development of laser cooling and trapping of neutral atoms 25 years ago [48] allowed the creation of ensembles of atoms at the micro-Kelvin level. At these ultra-cold temperatures, the thermal velocity of the atoms is small enough (of order a centimetre per second) for the atoms to be experimented with on the order of a second.

A magneto-optical trap (MOT) combines laser cooling with a anti-Helmholtz magnetic field to form a position dependent force on atoms, forcing them into the centre of the magnetic field. This creates a cold cloud of atoms which is the starting point for the atom interferometer. To commission the first MOT in Liverpool, several components needed to be implemented. A ultra-high vacuum (UHV) chamber needed to be constructed, containing a source of rubidium atoms for the MOT to trap. The vacuum chamber must also have a suitable geometry for three pairs of orthogonal counter-propagating laser beams to cross at the centre of a set of anti-Helmholtz electro-magnets. The laser beams need specific frequencies and polarisations required to laser cool and trap the atoms, and must be guided into the correct alignment using an optical circuit.

3.1 Theory

3.1.1 Laser Cooling

Atoms are cooled by laser beams with a frequency negatively detuned to a transition. To a stationary atom, photons of this energy do not have enough energy to stimulate the transition. Atoms moving towards the source of the photons see them Doppler shifted, and will absorb the photon and it's momentum. This reduces the atoms velocity but leaves it in an excited state. When the atom spontaneously de-excites, it emits a photon in a random direction, experiencing the recoil momentum associated with the emitted photon. The net effect is that the atoms momentum is lowered. This is summarised in figure 3.1. When three pairs of counter-propagating orthogonal laser beams are crossed, at a laser cooling frequency, atoms are cooled in all directions. This forms what is known as an optical molasses [49], which cools the atom, but as the laser

cooling forces are not position dependent, it atoms may diffuse from the laser beams.

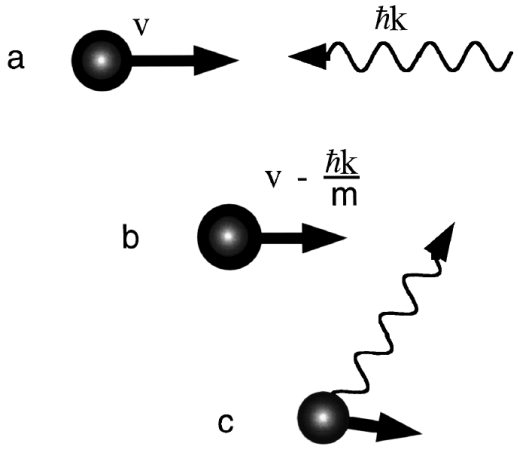

Figure 3.1: Figure summarising the laser cooling cycle. (a) An atom with velocity v encounters a photon momentum $\hbar k$: (b) The atom absorbs photon and is slowed by $\hbar k/m$: (c) The photon is re-radiated in a random direction, which on average, the atoms velocity is less than it's initial velocity. [48]

An equilibrium temperature is reached between the laser cooling and the heating effect of randomly absorbing and emitting photons. This limit is known as the the Doppler cooling limit, and the temperature T given by

$$k_B T = \frac{\hbar\gamma}{4}(\frac{\gamma}{2\delta} + \frac{2\delta}{\gamma}), \tag{3.1}$$

where k_B is Boltzmann constant, γ is the linewidth of the excited atomic state, and δ is the detuning from the transition [48]. The minimal value for this is given at $k_B T = \frac{\hbar\gamma}{2}$, with an optimal detuning of $\delta = \gamma/2$, which for Rb is 144 μK [50].

3.1.2 Magneto-Optical Trap

Anti-Helmholtz coils create a magnetic field with zero field at the centre, and a field that grows linearly away from the centre, given by the equation

$$\overrightarrow{B}(x, y, z) = B_{grad}(-\frac{x}{2}\hat{i} - \frac{y}{2}\hat{j} + z\hat{k}) \tag{3.2}$$

The centre of this field was aligned to coincide with the point where the counter-propagating laser beams cross.

Atoms have quantised total atomic angular momentum F, and $2F + 1$ magnetic sub-states m_F, ranging from $-F$ to $+F$. The total atomic angular momentum of the atom is comprised of the nuclear angular momentum I, and the total electron angular momentum J, which has contributions from the spin angular momentum S and the orbital angular momentum L [50]. The degeneracy of the magnetic sub-states is split by the magnetic field, and the energy difference increases the further the atoms are

from the centre of the magnetic field. To create a MOT, six counter-propagating beams are circularly polarised. The counter-propagating beam pairs have oppositely circular polarisations, labelled $\sigma^{\pm}$, and stimulate transitions that alter the atoms magnetic sub-states by $m_F \pm 1$. The polarisation of the beams can be seen in figure 3.2 [51].

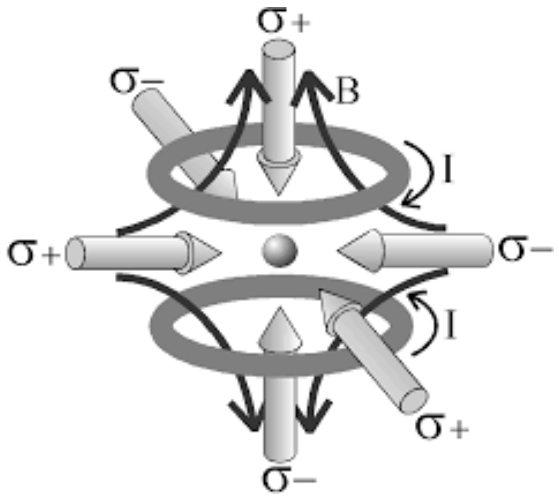

Figure 3.2: Sketch showing the correct polarisations for the MOT beams with respect to the anti-Helmholtz magnetic coils current [52].

A simplified 1-D example (figure 3.3) demonstrates how the Zeeman splitting from the anti-Helmholtz field can be used to create a position dependent force with circularly polarised beams. The $J = 1, m_F = 1$ state is lowered by the magnetic field in the negative x region. This reduces the energy required of the photon to stimulate the transition. A σ^- polarised photon travelling from negative to positive x-axis would be more likely to stimulate this transition because of the smaller energy gap. This energy gap is increased on the positive side of the x-axis, making stimulation of the transition less likely. A similar argument applies for a σ^- polarised photon travelling from the positive to negative x-axis, and the net result is that atoms are more likely to absorb photons forcing them towards the centre of the magnetic field. This can be expanded to 3-D and for higher angular momentum states.

3.1.3 Laser Cooling Rubidium Atoms

Rubidium atoms are a suitable candidate for laser cooling as the $D_2 5^2S_{\frac{1}{2}} \rightarrow 5^2P_{\frac{3}{2}}$ transition is at 780 nm, which may be stimulated with commercially available extended cavity diode lasers. Furthermore rubidium is an alkali metal, with only has one electron in the outer shell and hence a simple energy level structure close to the ground state. Limited state transitions allow for cooling cycles to be created. Another benefit is at UHV pressures, it forms a vapour, which can be used as a source of warm atoms for the laser cooling [50]. Naturally occurring rubidium is composed of two isotopes, 72% ^{85}Rb and 28% ^{87}Rb. As both isotopes have the same electron configuration ($5S^1$), they

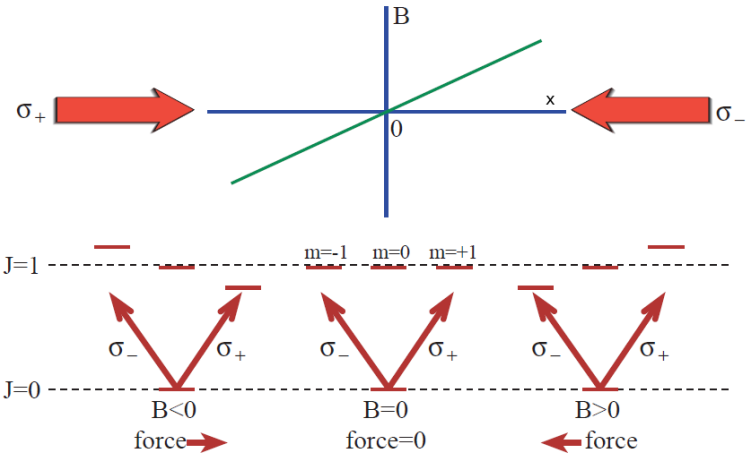

Figure 3.3: A sketch demonstrating a one dimensional explanation of how the position dependent force in a MOT arises from the magnetic field and circular polarised cooling beams [51].

are both suitable for laser cooling, and also atom interferometry.

Both isotopes were trapped using the apparatus described in this chapter, but ^{85}Rb was chosen for the interferometer. This decision was motivated by the smaller ground state splitting of ^{85}Rb (3 GHz compared to 6.8 GHz for ^{87}Rb), as the lower frequency RF signal generator, required for the Raman beams, was relatively inexpensive.

To implement laser cooling on rubidium, cooling and pumping frequencies are required. These are marked on an energy level diagram for ^{85}Rb in figure 3.4. The cooling frequency creates a cycle where atoms normally decay back into the $5^2S_{\frac{1}{2}}$ F = 3 state, due to the dipole selection rules. High order transitions can cause the atoms to fall back into the $5^2S_{\frac{1}{2}}$ F = 2 state and out of the cooling cycle. This occurs with a branching ration of approximately 1:1000, which would pump all the atoms into the F = 2 state on the order of ten microseconds.

To return the atoms in the $5^2S_{\frac{1}{2}}$ to the cooling cycle a pump laser excites any atoms that do fall into the $5^2S_{\frac{1}{2}}$ F = 2 state into the $5^2S_{\frac{3}{2}}$ F = 3 state, where they are free to spontaneously decay into either the $5^2S_{\frac{1}{2}}$ F = 2 or 3 states, with atoms decaying to $5^2S_{\frac{1}{2}}$ F = 3 state returning to the cooling cycle. The detuning from the $5^2S_{\frac{1}{2}}$ F = 3 $\rightarrow$ $5^2P_{\frac{3}{2}}$ F'= 4 is typically a few line-widths of the transition (6 MHz for both rubidium isotopes) [50].

3.2 Trapping Apparatus

The first MOT in Liverpool was constructed in March 2013, and was a portable retro reflecting MOT. A retro-reflected MOT is simpler optically, reducing the number of independent beams from six to three, which also reduces cost. However it inevitably results in an imbalance in the beam intensities, as transmission through the Rb vapour,

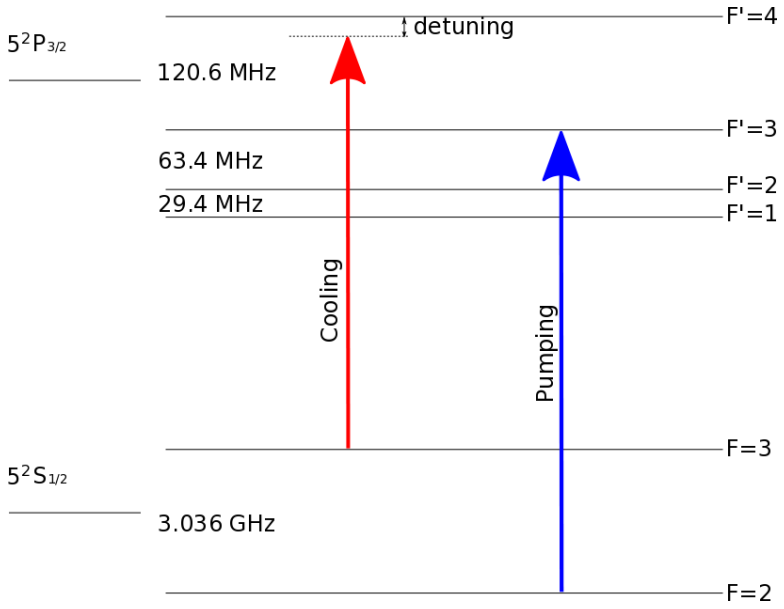

Figure 3.4: Energy level diagram for ^{85}Rb, with the cooling and pumping transitions illustrated.

vacuum windows, quarter-wave-plates and reflection off the mirrors all reduce the power in the beam. The MOT apparatus is described here, with the optical circuits presented for both the retro-reflecting trap and the balanced, six independent beam MOT.

3.2.1 Laser System

The laser system for the MOT consisted of two MOGLabs extended cavity diode lasers (ECDL's) [53]. Both lasers are sub 100 kHz linewidth, suitable for manipulating Rb hyperfine structure. These were frequency locked to the two required frequencies for the MOT, using an AC modulated saturated spectroscopy feedback.

Extended Cavity Diode Lasers

Bare laser diodes are not suitable for atom trapping as their linewidth is typically tens of mega-Hertz wide, wider than hyperfine transition line-widths. Bare diodes laser frequency varies with temperature and driving current at approximately 30 GHz/K and 3 $MHz/\mu A$ [54], which cannot be controlled as accurately as required. They are also very sensitive to optical feedback; any laser light reflected back into the diode forms an unwanted external cavity in which the laser light can resonate, affecting frequency stability.

ECDL's use this effect to stabilise the laser frequency. A commonly configuration is a Littrow extended cavity [55]. A sketch of this can be seen in figure 3.5. A diffraction grating is placed in front of the laser diode, at such an angle that the first order diffraction returns into the diode, creating a resonance cavity. The frequency of the laser is very sensitive to the length of the cavity. This length may be changed by a

piezoelectric transducer, which changes the angle of the grating when voltage is applied to it, which also changes the length of the cavity. A repeated scan in frequency can be implemented by applying a sawtooth voltage to the piezoelectric transducer.

Additional unwanted fluctuations in the length of the cavity also cause shifts in frequency. Hence ECDLs must be vibrationally isolated, mechanically rigid and temperature controlled to prevent changes in laser cavity. The ECDL's used in this experiment achieve this by machining the cavity out of a single piece of aluminium [55]. The ECDL is housed in a metal box to avoid air currents.

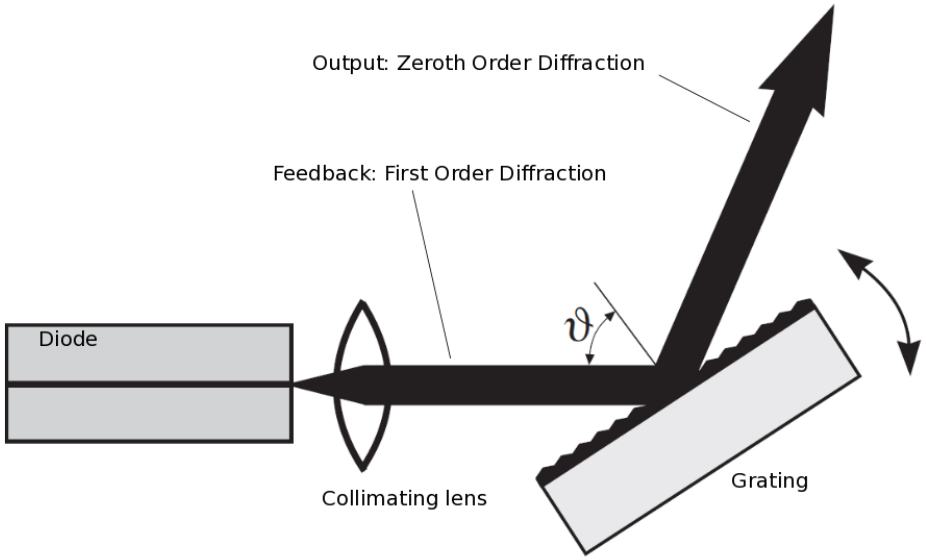

Figure 3.5: Sketch of a diode in a Littrow extended cavity. Feedback into the diode is provided by the first order diffraction of a grating [56].

The output of the ECDL is an elliptical beam. This is due the active layer of the diode having a rectangular cross-section, resulting in the beam axis' typically having a ratio between 1:2 and 1:4 [57], with the larger axis known as the fast axis. As the beam propagates, the shape of the beam will change, as the fast axis has a smaller divergence than the other axis, resulting in astigmatism of the beam.

3.2.2 Alignment of ECDL Grating

The following procedure was followed from the MOGLabs technical support and their ECDL manual [53] [58]. For proper operation the grating must be carefully aligned. The gratings are easily misaligned. This can occur during shipping or mechanical

creep over time. Therefore the external cavity needs to be optimised on receipt and periodically. The steps to do this are as follows.

First, the diode temperature must be set and stabilised. Typically the diodes used are designed to produce 785 nm at 25°C, and have a temperature dependence of -0.3 nm/K. This suggests the diode should be kept at about 12 °C to achieve a wavelength of 780 nm, but condensation forming in the electronics is risked at this temperature in high humidity. Fortunately the frequency of the ECDL is dominated by the gratings cavity alignment, and this can be used to 'pull' the laser to the correct wavelength at above 18 °C. The next step is to collimate the diode by focusing the beam to a minimum diameter at two metres. Following this the grating cavity needs aligning.

The horizontal alignment of the grating affects the wavelength of the ECDL, whilst the vertical alignment affects the cavity efficiency. First the vertical alignment must be optimised as this affects the optical power output by the ECDL. Initially, the lasing threshold of the diode should be found. At this is the point there is a sharp increase in the amount of optical power produced for an increase in current. This can be seen at 85 mA in figure 3.6, which is a graph of current against optical power.

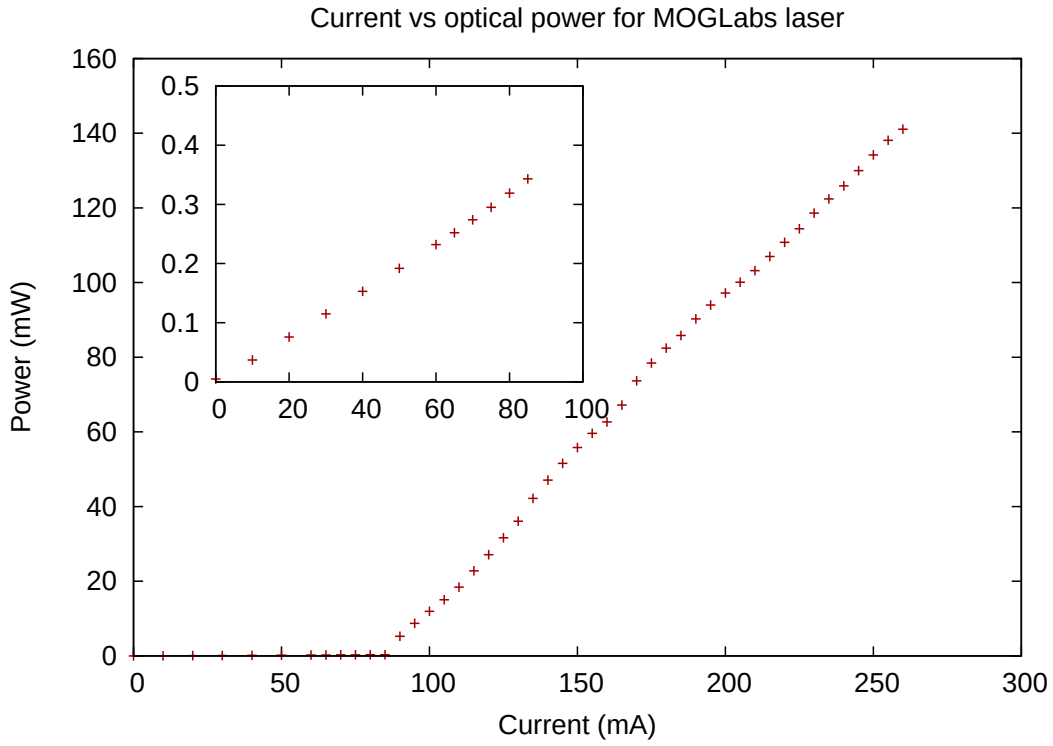

Figure 3.6: A current vs power plot for one of the MOGLabs ECDL. The ECDL starts lasing at 85 mA. The inset shows a smaller gradient before this current.

Setting the current just below the laser threshold current, and adjusting the vertical alignment of the grating causes the laser to 'flash', with an increase in optical power

output. This is an indication of an improved optimal alignment of the grating. This should be iterated, lowering the current each time until optimal. Finally the the current should be raised slowly noting the optical power is increasing. Raising the current should increase the optical power output if the grating is well aligned. The diode is likely to be damaged if raising the current further does not increase the optical power.

Whilst increasing the current, small vertical adjustments can be made to maximise the power output. However, the higher the current, the finer the adjustments need to be. Above 200 mA no adjustments were made to alignment, due to the required sensitivity needed to safely make them. Instead the current is reduced to below 200 mA to make adjustments, and then the current was increased to see the effect. Once the vertical alignment of the cavity is achieved, the horizontal alignment, which sets the wavelength must be tuned. To find the wavelength overlapping resonance in Rb, a search can be done by procedurally varying temperature, current and the horizontal grating alignment. Fluorescence is induced in a Rb vapour cell by the laser when the laser is at the correct wavelength. Changes in temperature should be made least frequently, as the diode temperature will take minutes to stabilise. Then the current should be altered in steps, with a scan of the wavelength at each setting done by altering the horizontal alignment. When the cavity is set up to fluoresce Rb atoms in a vapour cell, the ECDL is ready to be frequency locked.

Laser Frequency Locking

ECDL's wavelengths drift and therefore need to be locked. Both ECDL beams pass through AC saturated spectroscopy optical circuits, which can be seen in figure 3.7. The circuits photo-diode spectroscopy signals provide feedback to MOGLabs diode laser control boxes, which lock the laser frequency.

The AC locking circuits are based on saturated spectroscopy of a Rb vapour cell. With absorption spectroscopy, the laser is passed through the cell and the Rb vapour absorbs the laser photons when they have the correct frequency to stimulate transitions. However the Rb vapour is at room temperature and thus the frequency the Rb atoms absorbed is Doppler broadened due to the thermal motion of the atoms. This frequency broadening is at the giga-Hertz scale and completely masks the 6 MHz line-width hyperfine structure of the atoms. Figure 3.8 compares Doppler broadened Rb spectrum with the Doppler free, where the hyperfine structure can be seen. To see the hyperfine structure saturated spectroscopy is required.

In saturated spectroscopy, the laser is reflected back along its path, creating counter-propagating beams in the rubidium vapour. On the first pass the atoms are excited by the laser beam, with an intensity high enough to excite all atoms. The retro-reflected beam will cause stimulated emission of the excited atoms if they have zero velocity with respect to the laser beam. Atoms with non-zero velocity require a Doppler shift to the

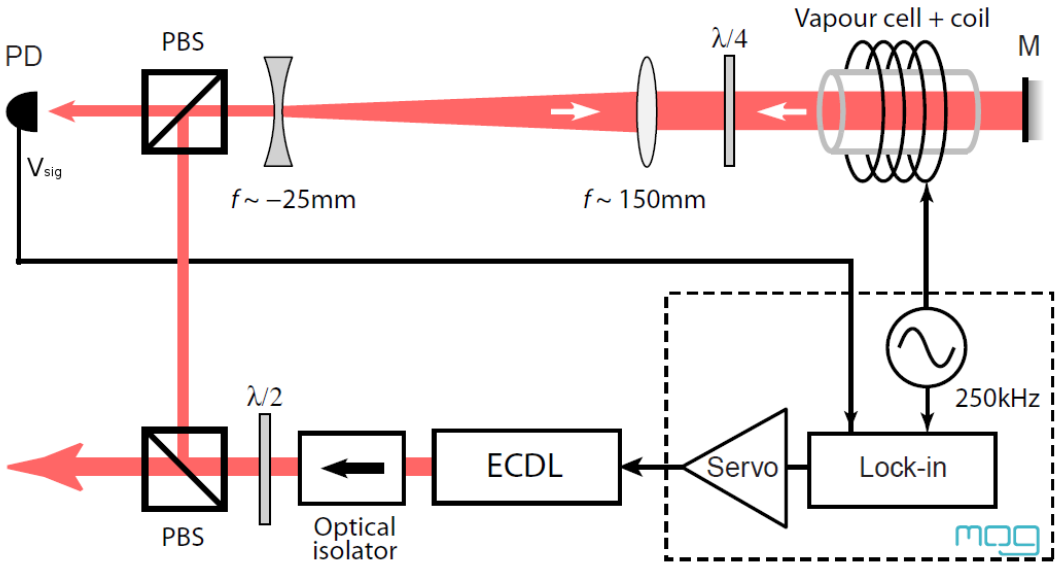

Figure 3.7: AC locking circuit for locking the ECDL. [59]

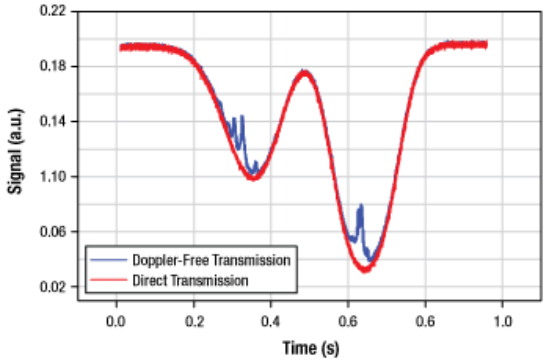

Figure 3.8: Plot of Doppler broadened (direct transmission) spectroscopy compared with saturated spectroscopy (Doppler-Free transmission) for Rb [60]

laser beam to be excited. For the retro-reflected beam, this Doppler shift is reversed so that the laser is off-resonance so no stimulated emission occurs. The stimulated emission allows the hyperfine states to be seen. Peaks can also occur when atoms are moving with a velocity such that they are Doppler shifted to absorb light from two different transitions from the two different directions. These peaks occur when the laser frequency is half way between two transitions and are called cross-over peaks.

The optical locking circuit is shown in figure 3.7. A 40 dB optical isolator protected the the ECDL from back reflections, as feedback of order one hundred nano-Watts would destabilise the lasers frequency. A variable beam-splitter is created with the combination of a half wave-plate ($\frac{\lambda}{2}$) followed by a polarising beam-splitter (PBS). About ten milli-Watts of the beam power is split into the locking circuit. The rest of the power continues for use in the experiment. Light incident on the second PBS is reflected, and sent through a beam expander, quarter wave-plate ($\frac{\lambda}{4}$) and a Rb vapour

cell, which is encased in a solenoid. The beam is then reflected back on itself, completing the saturated spectroscopy circuit. When the beam reaches the PBS, the two passes of the quarter wave-plate ensures the beam is transmitted through the PBS to be detected by the photo-diode.

The intensity of the beam is lowered by the beam expander, reducing saturation broadening of the Rb linewidth, whilst maintaining a high amplitude signal on the photo-diode. The frequency of the ECDL's is changed by a piezoelectric altering the angle of the feedback grating. To create a rubidium spectrum, like in figure 3.8, a sawtooth voltage was applied to the the piezoelectric to frequency sweep the laser.

The photo diode signal, V_{sig} is modified by the control box to generate an error signal in the following way [61]. When the laser is sweeping in frequency, the signal $V_{sig}(\omega)$ is a function of a slowly varying frequency ω. At the same time the solenoid surrounding the Rb vapour cell is driven by a 250 kHz signal, Zeeman shifting the transitions of the Rb. This modulation of the Zeeman energy levels manifests as a modulation of the frequency, $\omega(t) = \omega_0 + \Omega_0 cos\Omega t$, where Ω is the solenoid driving frequency. The frequency modulated signal can be written as a Taylor expansion,

$$V_{sig}(\omega) = V_s(\omega_0) + \frac{dV_s}{d\omega}(\Omega_0 cos\Omega t) + ... \tag{3.3}$$

The photo-diode signal is multiplied by a reference signal $V_{ref} = cos(\Omega t + \phi)$, which is the modulation signal with an adjustable phase ϕ to give

$$\begin{aligned} V_{sig}V_{ref} &= V_s cos(\Omega t + \phi) + \frac{dV_s}{d\omega}\Omega_0 cos(\Omega t) cos(\Omega t + \phi) \\ &= V_s cos(\Omega t + \phi) + \frac{1}{2}\Omega_0 \frac{dV_s}{d\omega} cos(2\Omega t + \phi) + \frac{1}{2}\Omega_0 \frac{dV_s}{d\omega} cos(\phi). \end{aligned} \tag{3.4}$$

This signal is then passed through a low pass filter and summed with a DC offset V_{DC} achieve the error signal,

$$V_{err} = \frac{1}{2}\Omega_0 \frac{dV_s}{d\omega} cos(\phi) + V_{DC} \tag{3.5}$$

The resulting error signal is proportional the differential of the signal and $cos(\phi)$ where ϕ is the adjustable phase. When there is a sudden change in absorption, such as when the frequency is modulated around a hyperfine transition, the error signal is large. The dependence on the reference phase allows the error signal to be adjusted from positive to negative. The V_{DC} allows for the signal to be shifted up and down, allowing the zero volts crossing point to be controlled.

The lock point of the laser is determined where the error signal crosses zero volts with a positive gradient. When the locking feedback is activated, the control box will lock the laser frequency to the point, a non-zero error signal modulates piezoelectric actuator for low frequency corrections (slow lock) and modulates the current for high

frequency corrections (fast lock). The gains on both the slow and fast locks can be individually optimised for stability of the lock. Examples of the ^{85}Rb and ^{87}Rb saturated spectroscopy spectrum can be seen in figure 3.9 and a smaller scan in frequency around the $5^2S_{\frac{1}{2}}$ F=3 $\rightarrow$ $5^2S_{\frac{3}{2}}$ levels in figure 3.10.

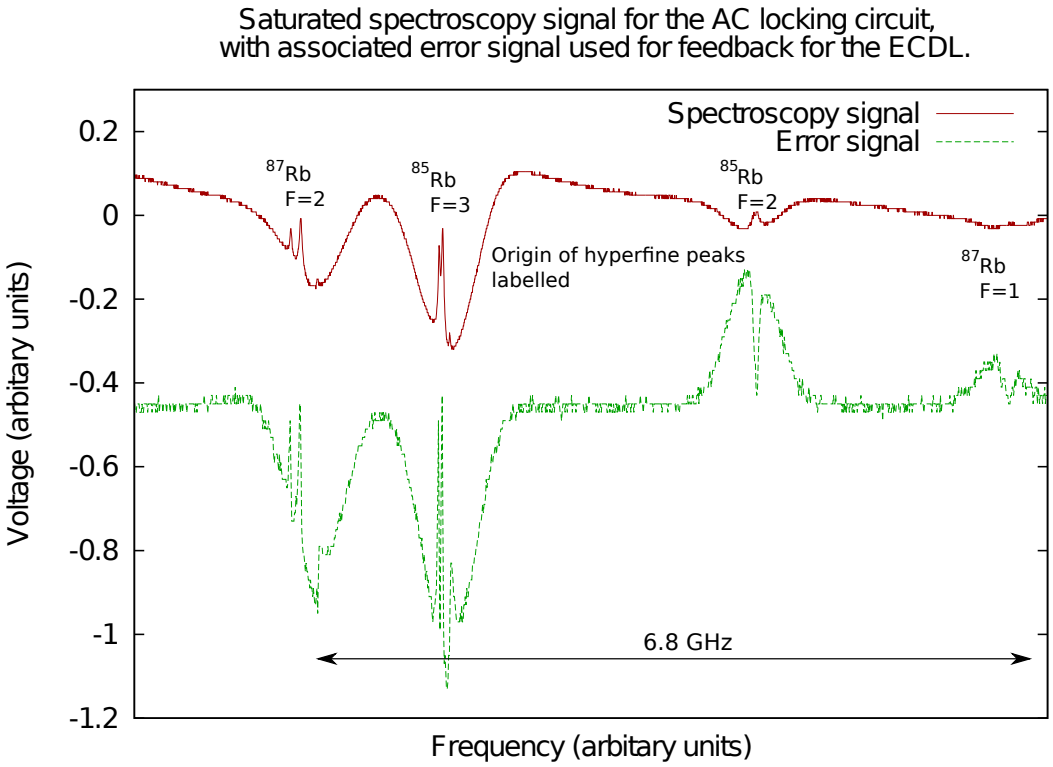

Figure 3.9: An example of the signal when the laser is freely scanning in frequency. On the x-axis is a linear scan in frequency, and on the y is the voltage generated by the saturated spectroscopy circuit in red, and the error signal in green. The hyperfine peaks are labelled.

An AC locking circuit was chosen because it can be locked in a range around the peak, by manipulating the error signal phase. This allows locking to the side of the peak, which is required for laser cooling. Additionally the AC lock should be free of drift, even if there is fluctuation in the error signals amplitude [61].

The two lasers locking circuits were built on 30 cm by 45 cm breadboards. This was done so the lasers could be transferred between apparatus's if needed, without having to rebuild the optical circuit. Note that in figure 3.11 the two circuits have the Rb cells on opposite sides. This was done because it was found that the fields from the solenoids interfere if placed next to each other.

The optical circuits were stable over a long period of time. However, due to mechanical creep in the ECDL, the grating alignment had to be periodically refined, approximately when there were large temperature changes in the lab.

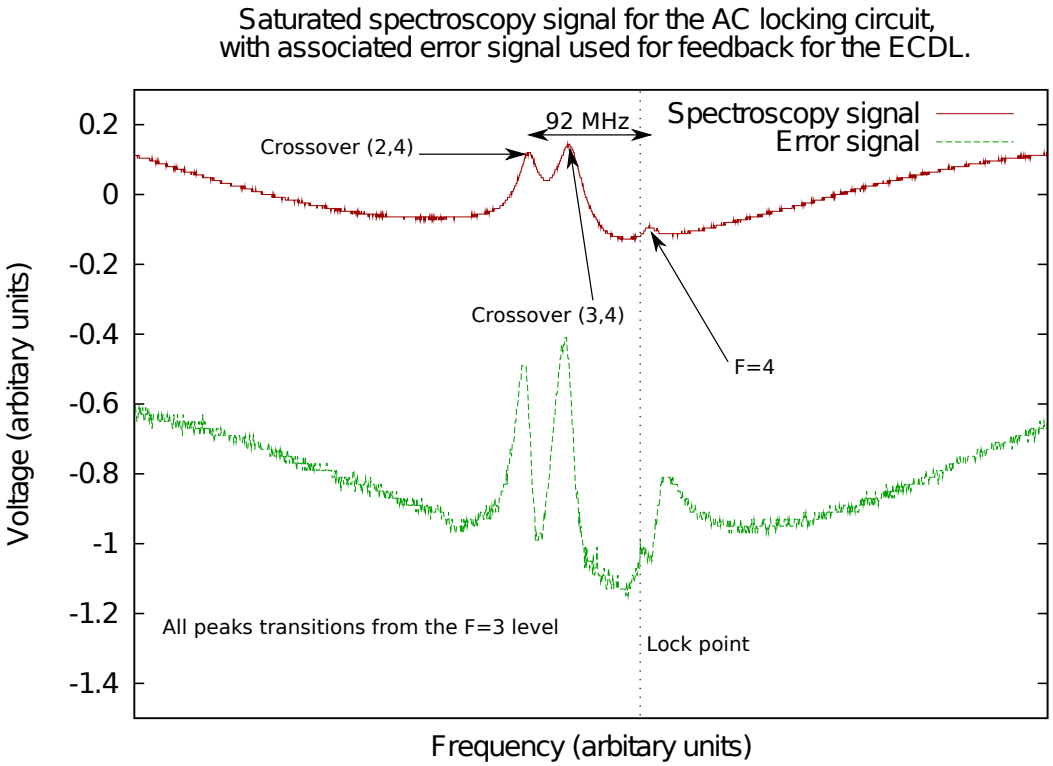

Figure 3.10: An example of the signal when the laser is freely scanning in frequency around the $5S_{\frac{1}{2}}$ F $= 3 \rightarrow 5P_{\frac{3}{2}}$ transitions. On the x-axis is a linear scan in frequency, and on the y is the voltage generated by the spectroscopy circuit in red, and the errors signal in green. This traces out the ^{85}Rb saturated spectroscopy spectrum for the F=3 $\rightarrow$ F' transitions in red, with the two large peaks in the centre being the (2,4) and (3,4) crossover peaks, with the smaller peak to the right being the F $= 3 \rightarrow$ F' $= 4$ peak.

3.2.3 Vacuum Chamber

The experimental chamber for the MOT is a 6 inch 'spherical octagon' [62]. This can be seen in figure 3.12. This allowed four of the octagonal ports and the two large side ports to be used for the MOT beams. The remaining ports were used to attach the vacuum pumps, and the warm rubidium source. An illustration of the vacuum chamber can be seen in figure 3.13.

When assembling the vacuum chamber all parts were cleaned with acetone and then ethanol using lint free cloths. The vacuum was pumped down from atmosphere using first a roughing pump, to 10^{-2} $mbar$. The vacuum was further lowered to $10^{-7} mbar$ by a turbo pump. The vacuum chamber was then baked out over a weekend at 150 $^{\circ}C$. To bake out, heater tape was wrapped around the vacuum chamber and a thermocouple measured the temperature. The chamber was then wrapped in aluminium foil once, then insulating material, and a further layer of aluminium foil. After the weekend, the warm rubidium source was commissioned and finally the ion pump was used to lower the pressure to a pressure of 3 $\times 10^{-10} mbar$.

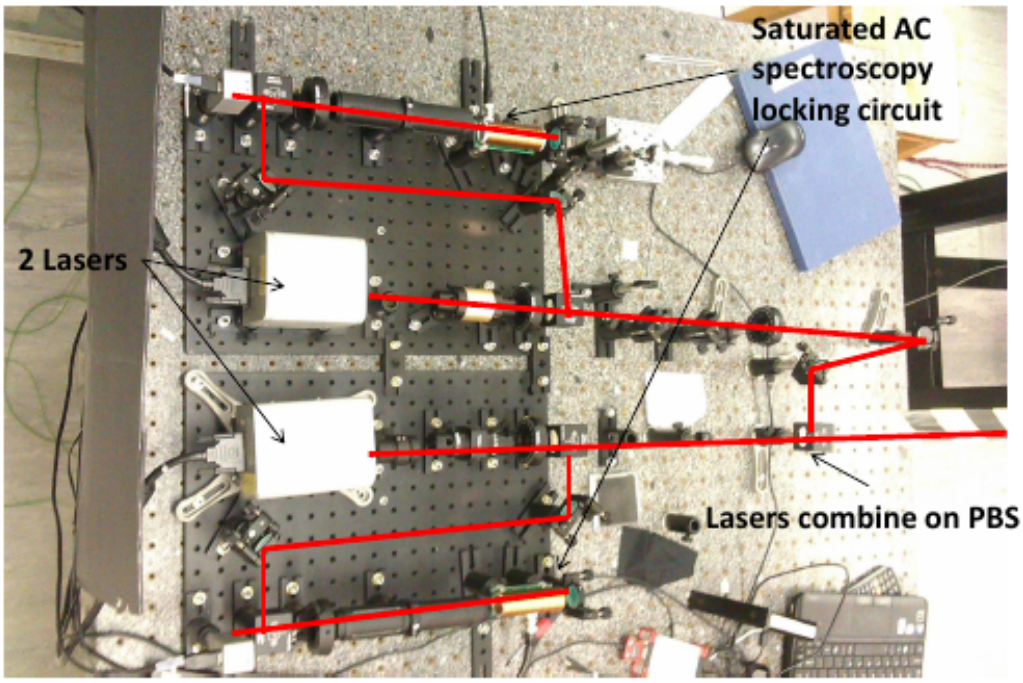

Figure 3.11: Photo of the two ECDL and the respective AC locking optical circuits.

Figure 3.12: Drawing of the spherical octagon vacuum component [62].

3.2.4 Rubidium Vapour Source

The source of atoms for the MOT was a warm rubidium getter source [63]. The getters have a boat of rubidium chromate along their length. When a current of 3 - 5 A is passed through them, the boat heats up and rubidium vapour is emitted. When initially using the getters, there is a large amount of out-gassing into the vacuum chamber. A commissioning procedure is used to prepare the getters for use [64]. The current to the getters is slowly raised from 0 A to 3 A, not allowing the pressure to rise above 10^{-5} $mbar$. This is done under the turbo pump. This takes several hours. Then three 8 A, 5 s pulses are applied. After this procedure the getters are reported to produce Rb vapour at 3 A for more than a thousand hours [64].

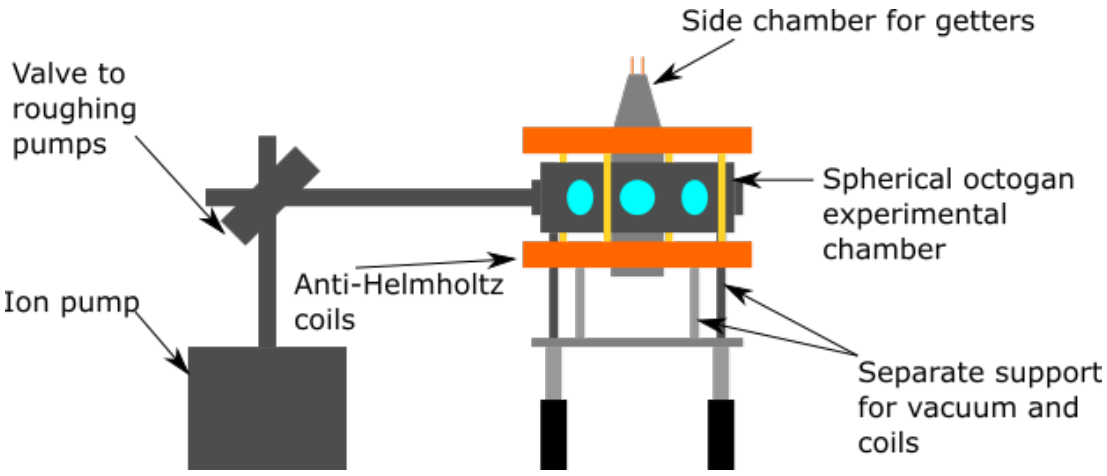

Figure 3.13: Sketch of the portable MOT vacuum chamber, with coils mounted. The getter chamber is mounted off the side of the spherical octagon experimental chamber.

To confirm that the getters were working a video was taken as current was applied. A laser was passed through the vacuum chamber to fluoresce any rubidium in the chamber. A sketch of this apparatus can be seen in figure 3.14. A frame from a video can be seen in figure 3.15. In the foreground is the getter and the rubidium chromate can be seen glowing. In the background the rubidium vapour can be seen fluorescing on the laser path, and turbulence can be seen near the getter as the gas is produced.

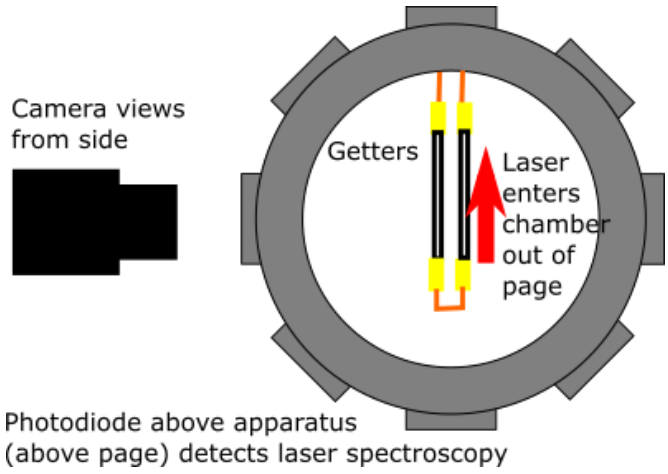

Figure 3.14: Diagram of the vacuum chamber that the getters were originally tested in.

To further prove that rubidium vapour was being produced, saturated spectroscopy was performed on the vacuum chamber, and the same spectroscopy signal was seen in both the locking circuit vapour cell and the vacuum chamber. This can be seen in figure 3.16. The Doppler broadened signal as well as the some of the cross-over peaks can be recognised as in the vacuum spectroscopy.

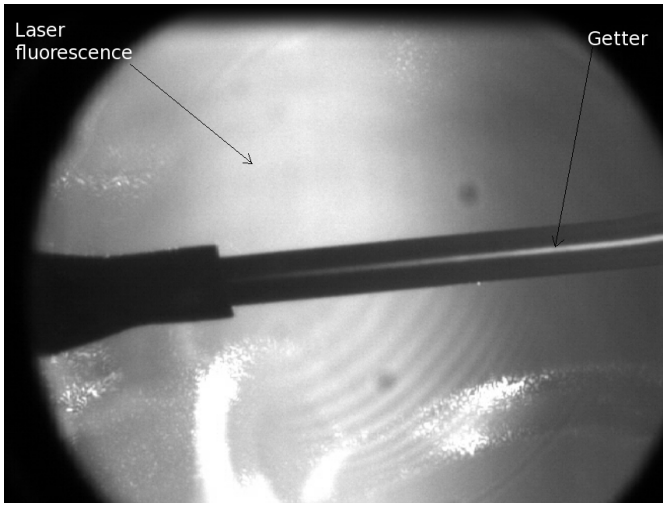

Figure 3.15: Frame from a video of the rubidium getters whilst being tested. The getter can be seen in the foreground, with the boat glowing hot. In the background laser fluorescence of the rubidium can be seen in the background.

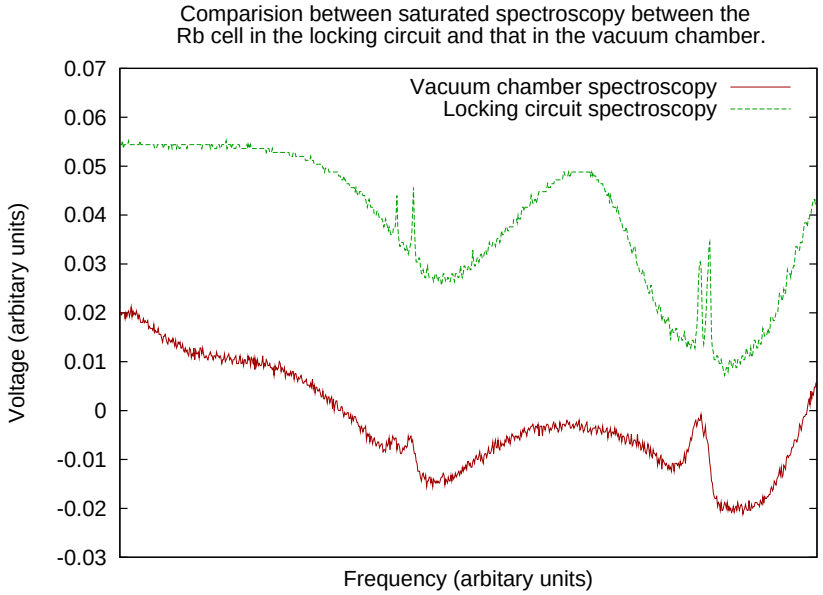

Figure 3.16: Saturated spectroscopy of rubidium in the locking circuits Rb vapour cells alongside saturated spectroscopy in the vacuum chamber.

3.2.5 Anti-Helmholtz Magnetic Coils

The magnetic field was provided by coils near to the anti-Helmholtz design, with radius of 8 cm. Testing the coils found the magnetic field to be linear in the central region, suitable for creating the MOT magnetic field. Measurements were made of the with a forward and a reverse current in the coils. The magnetic field centre was found to be the geometric centre to within 1 mm, which can be seen in figure 3.17. This accuracy was limited by the dimensions of the Hall-probe. At 3.45 A, a 5.5 G/cm field gradient

is generated. Fits were only applied to the central region, 45-85 mm.

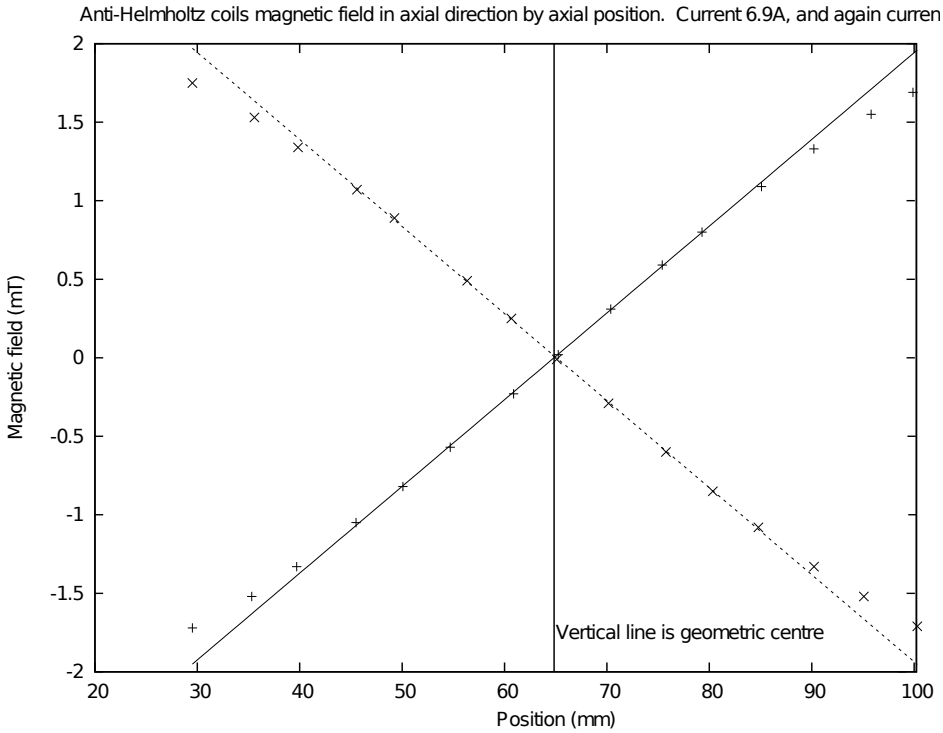

Figure 3.17: Axial magnetic field along the axial direction of the coils. The two sets of data are for forward and a reverse current in the coils. Where they cross is the centre of the magnetic field. The vertical line is the geometric centre of the coils.

3.2.6 Optical Circuit

Retro-Reflecting Trap

The optical circuit for the retro-reflecting trap can be seen in figure 3.18. How the beams cross in the vacuum chamber is further illustrated in figure 3.19. To the left of the diagram, the two ECDL's and their locking circuits are mounted. The laser beams are combined on PBS 3, and then expanded to 10 mm.

The beam is split throughout the circuit using a combination of a half wave-plate and PBS to form a variable beam-splitter. On PBS 4 the trap beam is split in a 2:1 ratio, with the larger fraction of the power being raised to the MOT chamber level. PBS 5 splits the power in a 1:1.

The beams are guided into the MOT chamber, through quarter wave-plates to circularly polarise the beams and cross at the centre of the magnetic field. They are then passed through another quarter wave-plate and are retro-reflected to form the required counter-propagating beam pairs. Similarly the beam that is transmitted through PBS 4 is guided to below the MOT chamber, and reflected upwards and retro-reflected at the top by optics suspended over the top of the vacuum chamber. A photograph of the optics can be seen in figure 3.20.

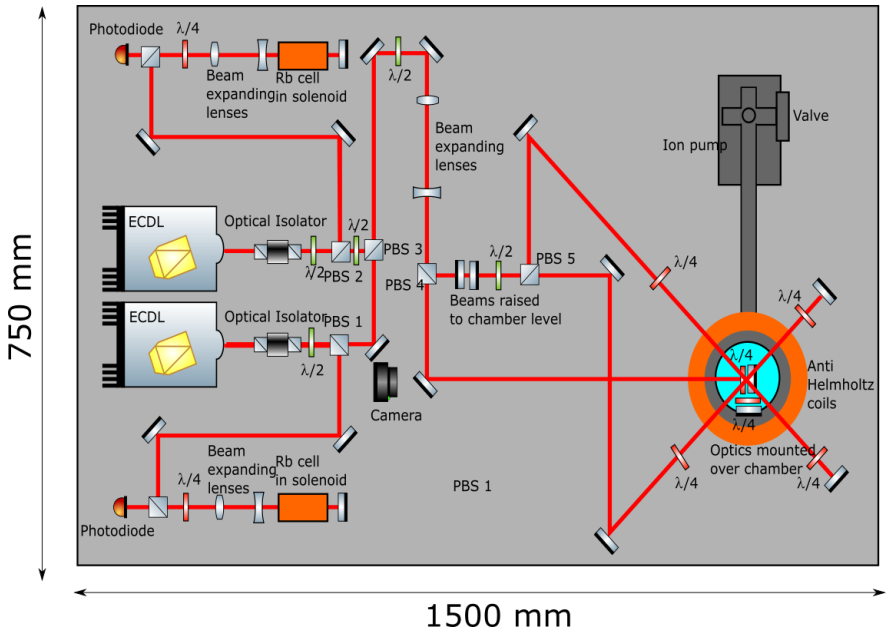

Figure 3.18: Sketch of the retro-reflected beam MOT optical circuit.

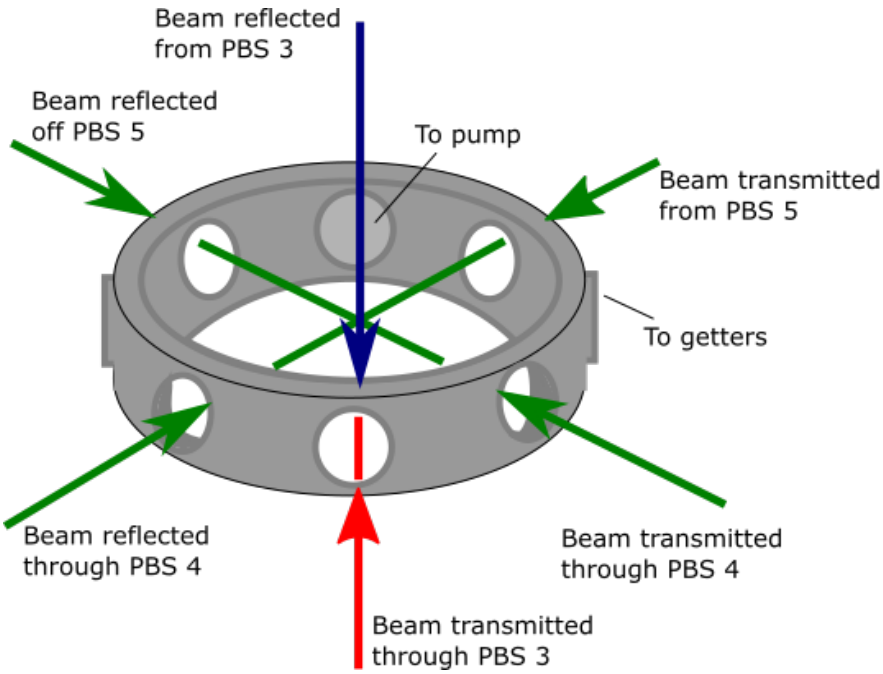

Figure 3.19: Illustration of how the laser beams crossed in the vacuum chamber in the retro-reflected beam set up.

Balanced Beam Trap.

The optical circuit overlaps six beams, each with a circular polarisation to make the counter-propagating beams as shown in figure 3.2, in the centre of the magnetic coils. This circuit utilises the same beams sources and combination technique as the retro-reflecting circuit. The combined beam enters at the bottom left of figure 3.21. Two

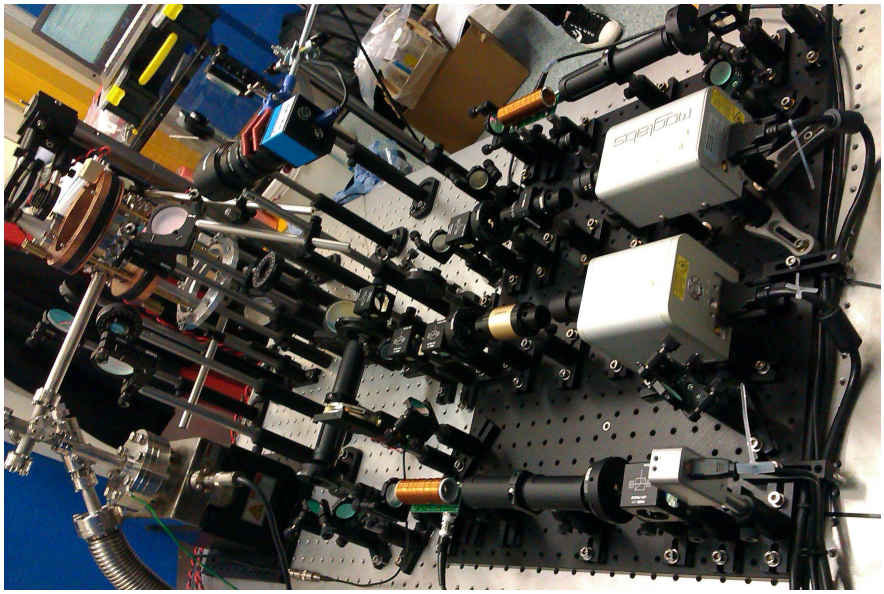

Figure 3.20: Photograph of the retro-reflected MOT.

sets of beams cross through the vacuum chamber horizontally, and thus are at the same height. The third pair of beams enter the chamber vertically from the bottom and is retro-reflected at the top, requiring two additional heights for the optics. How the beams cross in the vacuum chamber is illustrated further in figure 3.22

The beams are split into three parts with equal trap power, each of which are subsequently split into two. This is done by splitting the beam in a 1:2 ratio at PBS 1 and then a 1:1 ratio on PBS 2. Beam expanders increase the beam diameter to 10 mm. The half wave-plates are located before the beam expanders, so a smaller diameter wave-plate could be used for economy.

On PBS 3, one half of the beam is reflected upwards 60 cm, where it is reflected to a mirror suspended over the centre of the MOT chamber, and through a quarter wave-plate and into the experimental chamber. Similarly the other half is reflected to a mirror beneath the chamber, through a quarter wave-plate and into the experimental chamber. The other two beams are split in half on PBS 4 and 5. Along both beam paths the beam is expanded to 10 mm. The main difference between these two sets of paths is that to avoid the vacuum chamber pipe to the ion pump, the beam split by PBS 5 is raised to the MOT level twice (about 30 cm high). This results in the beams not being split into counter-propagating pairs on the same PBS in the horizontal plane.

To commission the MOT the quarter wave-plate's fast axis' angle relative to the polarisation of the incoming beam had to be set, to the correct circular polarisation of the laser beam. This was done by initially forming a retro-reflected trap, to reduce the degrees of freedom of the possible combinations of polarisations whilst initially producing the MOT. This was done to reduce possible issues in the apparatus. After achieving a MOT with retro-reflected beams, the beams were brought back in one by one

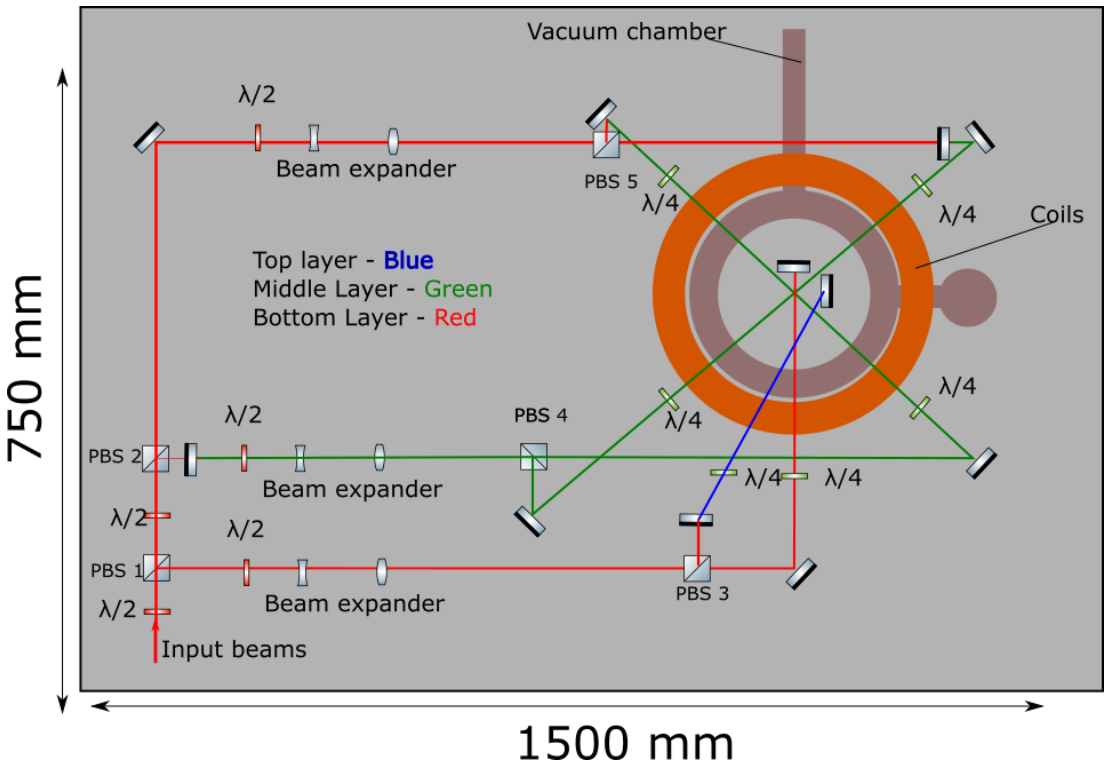

Figure 3.21: Schematic of the MOT optics for the balanced beam MOT. The lasers are on three different levels, indicated by the colour of the beam path, red being at table level, green being at the height of the side windows, and purple being above the vacuum chamber. PBS is a polarising beam-splitter, $\lambda/2$ is a half-wave-plate, and $\lambda/4$ a quarter-wave-plate. A photograph of this circuit under construction can be seen in figure 3.23

to ensure the correct polarisations for the MOT. The beam powers were balanced using an optical power meter and adjusting the half-wave plates to achieve good splitting on the PBS's. A photograph of the MOT optics with all but the beam expanders in place can be seen in figure 3.23.

3.3 Measurement of Atom Number

The bright oval shaped object in figure 3.24 is the trapped atoms. Fluorescence of the background vapour atoms can be seen, particularly in the horizontal plane, as the beam is twice as intense here. The dark circle framing the photo is the vacuum port that the MOT is being observed through, with stray reflections on its edge. This MOT can also been seen in a colour photo in figure 3.25, as the bright white spot in the crossing of the pink laser beams, as they fluoresce the background atoms.

Measurements are made from the videos of the MOT, taken with a CMOS camera. An area of interest around the MOT is selected and the pixel values of individual frames are integrated. Figure 3.26 is a comparison of 2D histograms when the MOT coils are

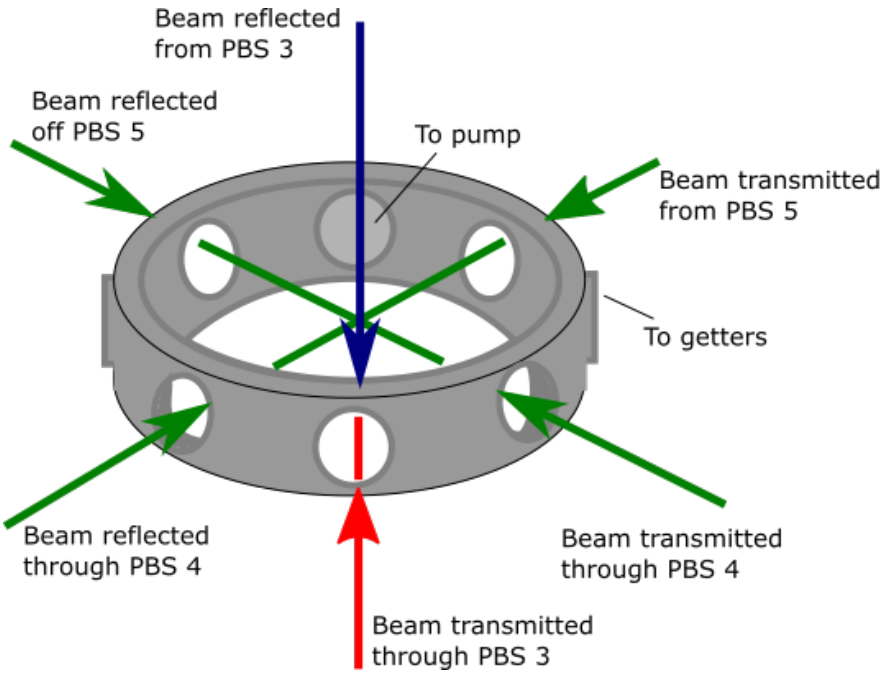

Figure 3.22: Illustration of how the laser beams crossed in the vacuum chamber in the balanced beam set up.

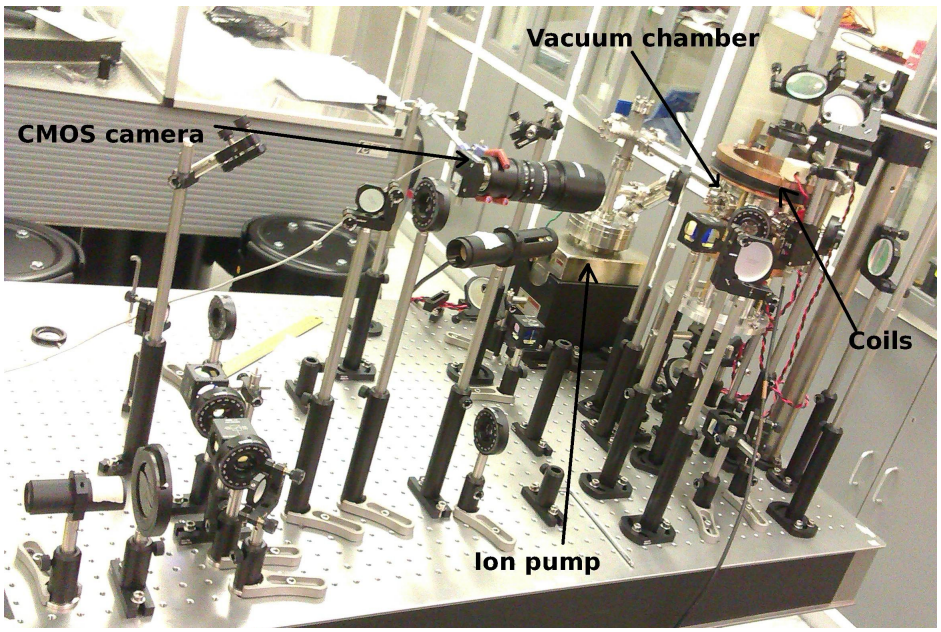

Figure 3.23: A photograph of the optical circuit sketched in figure 3.21 under construction. The three different levels of optical circuit can be seen.

on and off. The MOT forms a peak of intensity in the centre. Integrating the pixel values for these two images, and subtracting the MOT off image from the MOT on image finds the increase of fluorescence responsible due to the atoms trapped in the MOT. The MOT was turned off by turning off the field to minimise changes to the background fluorescence which is a standard method [65].

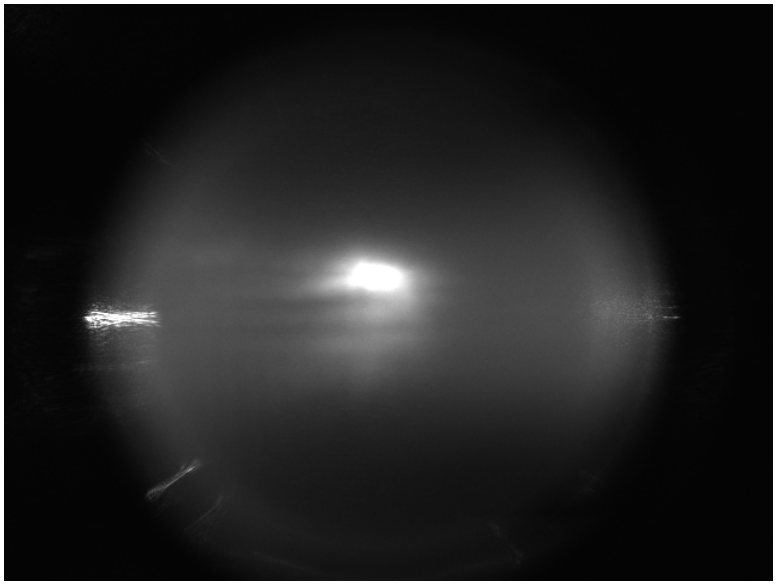

Figure 3.24: A black and white photograph of one of the first MOTs using the CMOS camera.

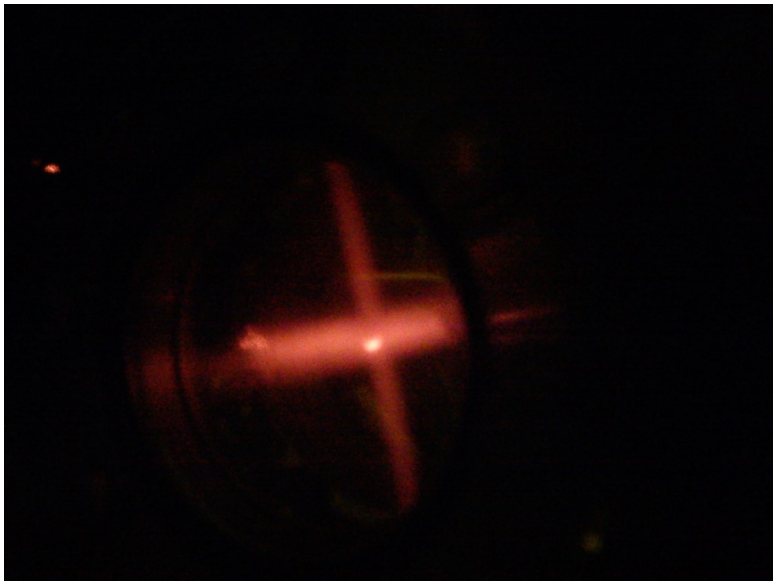

Figure 3.25: A colour photo of the MOT.

3.3.1 Atom Number

The total integrated fluorescence can be related to the number of atoms trapped. Atoms trapped in a MOT scatter light out homogeneously. If N atoms are trapped, then the power received by a detector with surface area A, and distance D from the trap and scattering rate Γ, is

$$P = N\Gamma E_\gamma \frac{A}{4\pi D^2}, \tag{3.6}$$

where E_γ is the energy carried by each photon. The scattering rate of the atoms

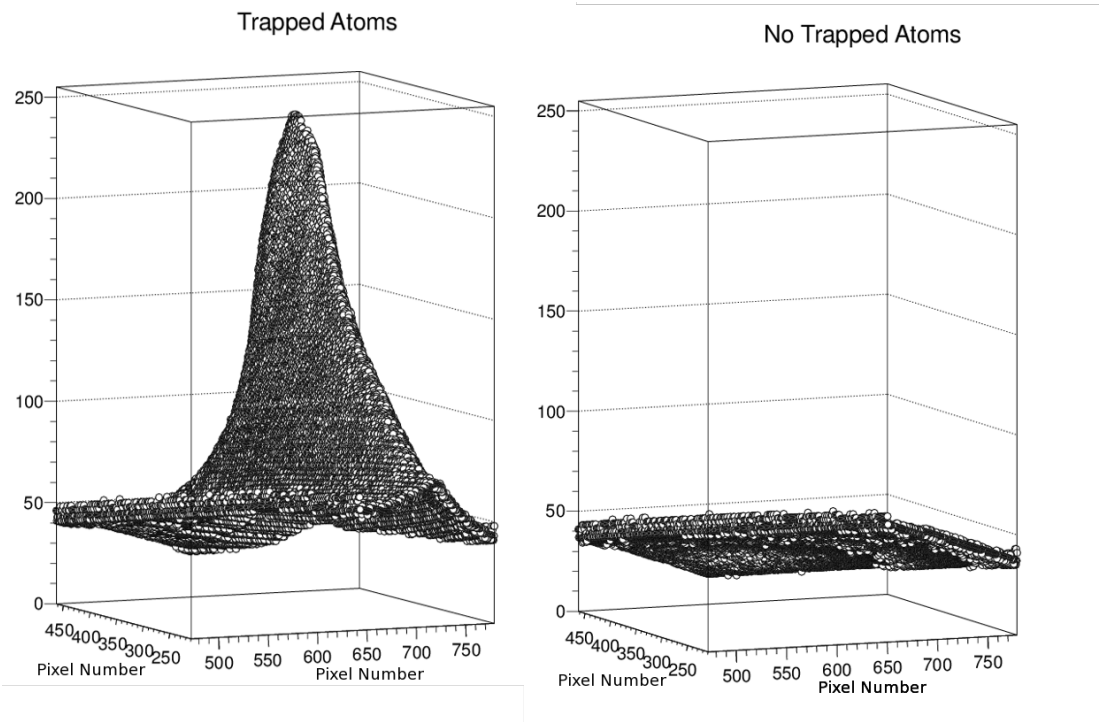

Figure 3.26: 2D histograms of the pixel values for the MOT on and off.

[50], Γ is given by

$$\Gamma(I,\delta) = \frac{\gamma}{2}\frac{I/I_{sat}}{1 + I/I_{sat} + (2\delta/\gamma)^2}. \tag{3.7}$$

In this equation, γ is the spontaneous decay rate of the transition $5^2S_{\frac{1}{2}} \rightarrow 5^2P_{\frac{3}{2}}$ of $38.117(11)\times10^6 s^{-1}$, I is the intensity of the lasers, I_{sat} is the saturation intensity of the $|F = 3, mF = \pm3 > \rightarrow |F = 4, mF = \pm4 >$ transition ($\sigma^{\pm}$ - polarized light), which is 1.669 32(35) $mW cm^{-2}$, and the δ is the detuning from the transition [50].

To measure the power radiated off the atoms, initially simultaneous measurements of the power received by the power meter, and video of the atom trap were taken. The video was split into individual frames using FFMPEG [66], and the pixel values for the individual frames of video were summed over using the CImg library [67]. The videos were taken, selecting a fixed area of interest around the trapped atoms that remained constant throughout the measurements. The power meter was placed at the vacuum chamber window, 8 cm away from the trapping point. The power meter has a 9.5 mm diameter, giving it an area of 0.71 cm^2 and was placed at the vacuum chamber window, 8 cm away from the trapping point. The energy carried by the photons is 2.56 $\times10^{-19}$ J.

The number of atoms was varied by changing the magnetic field strength, which is a standard method [65]. The power readings and the MOT images compared the atom trap on (magnetic field on) to atom trap off (magnetic field off). A calibration

was done between the absolute power measurements and the sum of the pixel values of stills from the video.

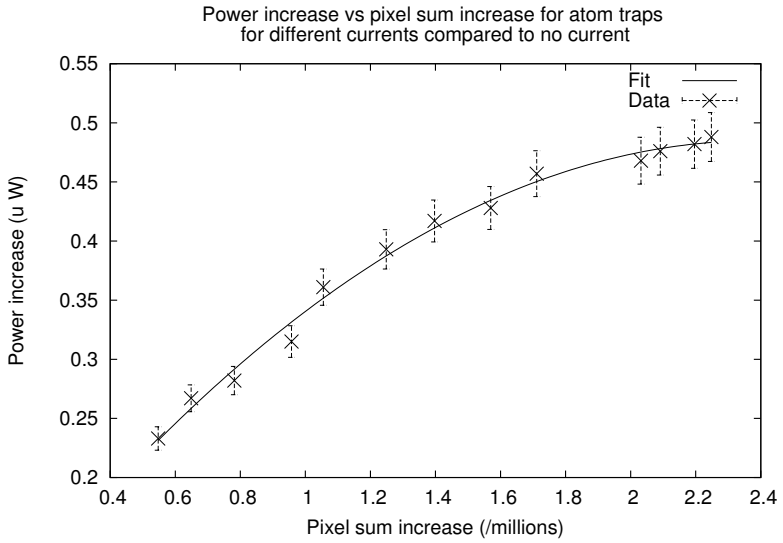

Figure 3.27: Graph of the calibration between optical power increase and pixel sum increase. The error on the power increase is the standard deviation of 20 power measurements taken over 10 s. A quadratic fit was made, to $f(x) = Ax^2 + Bx + C$, with A = -0.0743, B = 0.356 and C = 0.0588.

With this calibration performed measurements of the number of atoms were made varying the parameters. The default setting for the magnetic field was 13.6 G/cm. This was extrapolated from knowing the field gradient was 5.5 G/cm at 3.45 A (see figure 3.17), and the error was estimated to be 0.2 G/cm, by how accurate the power supply could be set. Efforts were made to keep the pressure in the vacuum chamber constant. This was done by operating the getters for few minutes, and then waiting half an hour before measurements were made. The pressure was read off the ion pump, which estimates the pressure in the chamber by the current flow. Typically it was 6×10^{-10} $mbar$. The trap beam peak intensity was 14.6 mW/cm^2 per beam. An error of 2 mW/cm^2 was estimated by measuring the power for different sizes of the beam whilst irised. The pump beam was used at maximal power, with approximately 50 mW reaching the MOT.

Figures 3.28 and 3.29 show the number of atoms trapped when varying the magnetic field gradient and the trap beam intensity respectively. In both cases the MOT appears to be in a linear proportionality regime; greater magnetic field gradients and greater beam intensity would trap more atoms. The errors on these measurements are from the above error estimations propagated through. The largest number of atoms trapped was $(65.7 \pm 4.4) \times 10^6$.

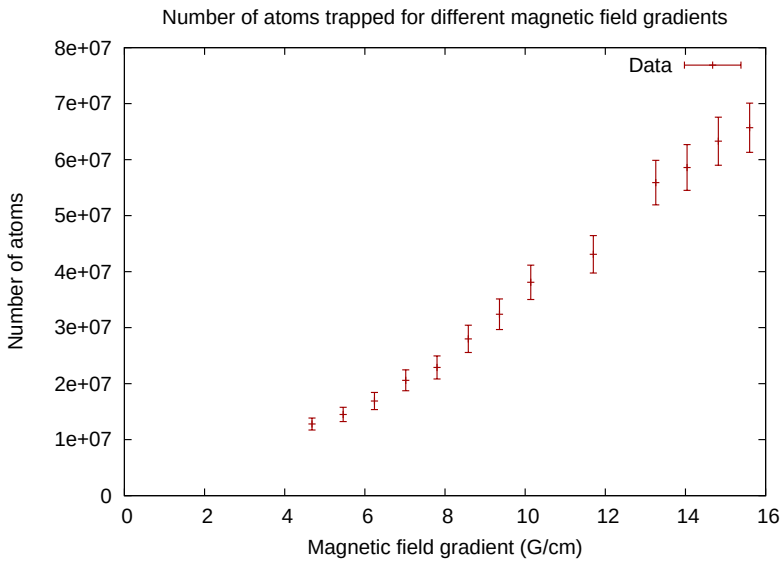

Figure 3.28: Graph of number of atoms trapped for different magnetic field gradients.

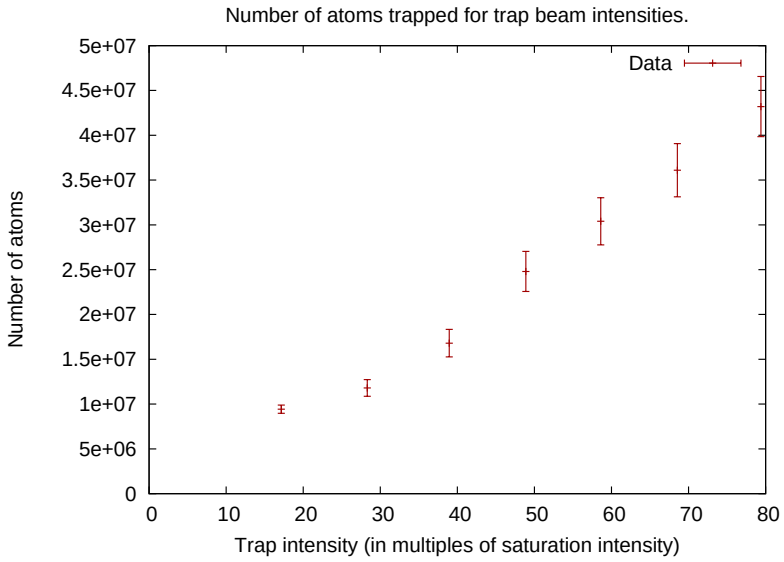

Figure 3.29: Graph of number of atoms trapped for different trap beam intensities.

3.4 Summary

The implementation of a magneto-optical trap was the first source of ultra-cold atoms in Liverpool, and a key step towards the prototype atom interferometer. The theory of laser cooling and MOT's have been presented as well as the development of our trapping apparatus. This apparatus was capable of trapping $(65.7 \pm 4.4) \times 10^6$ atoms and demonstrated improved quantities of atoms with higher magnetic field and laser intensity.

The laser's and their corresponding frequency locking optical circuits, rubidium

vapour source and anti-Helmholtz coils presented here was directly used on the next iteration of the experiment, the prototype atom interferometer, which is discussed in the next chapter. The image analysis and the measurements developed here provided the foundation for further measurements performed on the prototype atom interferometer, and will be discussed in chapter 6.

Chapter 4

Requirements and Design of an Atom Interferometer

A prototype atom interferometer was designed and constructed at the University of Liverpool. It is currently under the commissioning stages. This chapter describes the design of the interferometer, and the required laser frequencies. Chapter 5 describes how these laser frequencies are generated.

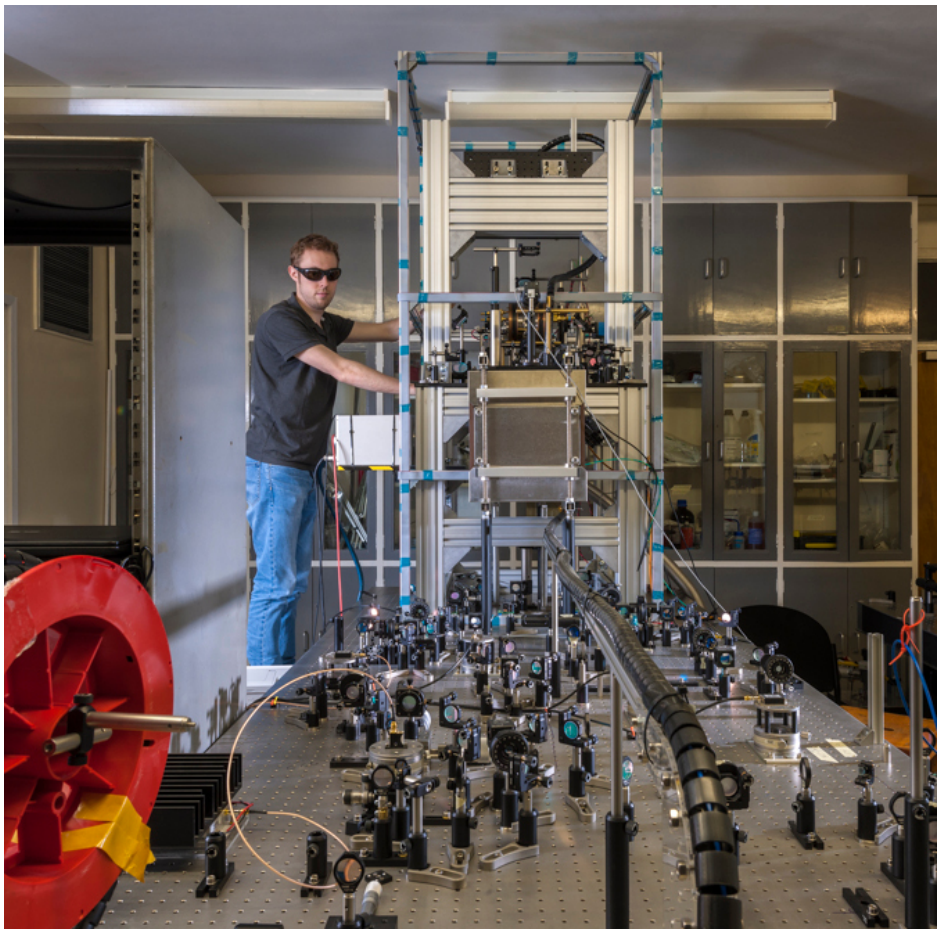

Figure 4.1: Photograph of the optics table with the prototype atom interferometer.

There are two optical tables, the laser sources occupy one as they are sensitive to vibrations, so are isolated from the rest of the experiment. The lasers pass to the other optical table via single mode polarisation maintaining fibres. On this table all the laser frequency generation optics are located and are launched into the experimental chamber, which is also located on the same optical table. This optical table can be seen in figure 4.1. Two equipment racks house the required equipment, one which contains the power supplies for the electro-magnets and getters, FPGA boards and laser control boxes, whilst the other contains the RF signal generators so they located as close as possible to where required.

4.1 Vacuum Chamber

In an atom interferometer atoms in a quantum super-position freely fall for periods of up to the of order of seconds. Ultra-high vacuum is desirable for a atom interferometry as any collisions with background vapour would destroy the super-position. At 10^{-9} $mbar$ the mean free path of a Rubidium gas at room temperature is about 1 km [68].

A sketch of the experiment can be seen in figure 4.2. The atoms are trapped in the spherical octagonal chamber at the top of the experiment and then dropped through the interferometer tube into the detection chamber. The MOT has undergone a 90 degree rotation from the apparatus discussed in chapter 3. The MOT beams are in a (1,1,0) configuration, where two of the beam pairs enter at a 45° angle from horizontal, with the last beam pair crossing the beams horizontally. This frees the vertical axis so it can be used purely for the Raman interferometry beams, and also the largest windows are vertical for optical access and additional laser beams. For example, these windows are used for the optical state selection method. The warm rubidium source is connected to the side of this chamber. State selection will also be done in the spherical octagonal chamber. A 40 cm pipe connects this to a larger 6-way cross at the bottom of the experiment, which will be used for the detection. This gives the prototype atom interferometer a maximum region of roughly 50 cm, and a maximum interferometry time of 320 ms for a drop.

The vacuum is maintained by an ion pump, which is mounted on a stand-off pipe from the detection chamber. This stand-off is to minimise the effect of magnetic field associated with the ion pump on the interferometer. An ion gauge and a valve are also attached to this 6-way cross. A 75 cm by 75 cm optical breadboard with a hole cut out of the centre for the vacuum pipe is mounted so that the optics for the MOT and state selection can be mounted around the spherical octagon. This mount is firmly clamped and has cross beams to prevent flexibility of the structure. On top of this breadboard a further breadboard is supported vertically over the top of the experiment to mount the Raman optics.

The vacuum chamber was constructed and commissioned using the techniques out-

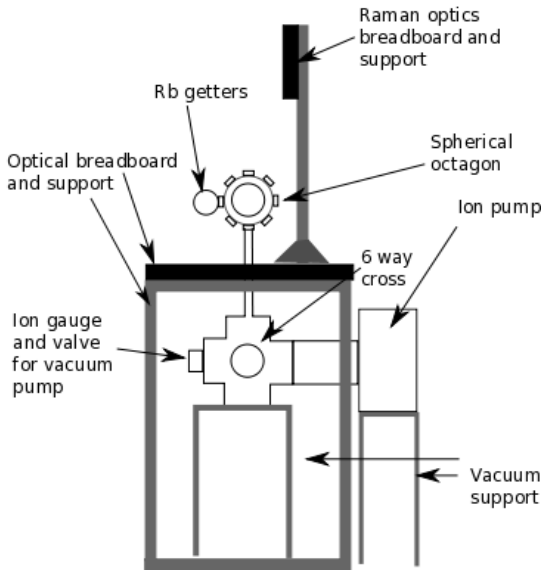

Figure 4.2: Sketch of the vacuum system for the prototype interferometer

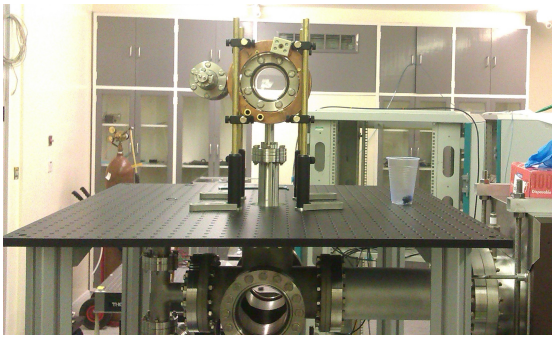

Figure 4.3: Photograph of vacuum system.

lined in section 3.2.3. The vacuum after baking out was lowered to 10^{-9} *mbar*.

4.2 Magneto-Optical Trap, Optical Molasses and Atom Dropping

The atoms are trapped in a MOT and are then further cooled in an optical molasses, before being released, allowing the atoms to enter free fall. The optical molasses stage further cools the atoms by increasing the effect of polarisation gradient cooling, by reducing the magnetic field and increasing the detuning. The counter-propagating laser beams form a lattice of potential wells which the atoms must be adiabatically released from, to prevent the potential energy being gained as kinetic energy. The optical molasses and the release to drop the atoms are discussed here.

4.2.1 Polarisation Gradient Cooling

The first experiments with laser cooling found that the atoms were being cooled below the theoretical expected temperature, the Doppler limit [69]. The cause of this was found to be polarisation gradient cooling, a sub-Doppler mechanism that can lower the temperature to approach the recoil limit, which is the temperature of an atom which spontaneously emits a photon from rest. For ^{85}Rb the temperature has been lowered to 30 μK using optical molasses [46]. The polarisation gradient cooling described here is of the σ^+-σ^- type, for a transition between a ground state with J = 1 and excited state J = 2.

The superposition of σ^+-σ^- counter-propagating beams creates a linear polarised electric field rotating in space, sketched in figure 4.4. For moving atoms, this can be shown to create unbalanced radiation pressures and consequently a force opposing the motion of moving atoms [27], with a lower temperature cooling limit than Doppler cooling.

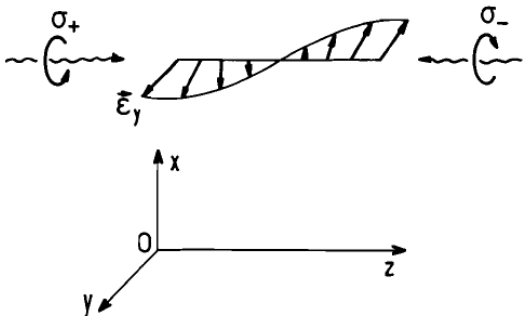

Figure 4.4: Sketch demonstrating how the combination of circular polarisations adds to a rotating linear polarisation [27].

The magnetic sub-states are split by the AC Stark effect. Stationary atoms are optically pumped by the linear polarisation, and the atoms are distributed symmetrically around the central sub-state. The steady state populations are $4/17, 9/17, 4/17$ for the sub-states g_{-1}, g_0, g_{+1}, represented by the circles in figure 4.5.

However, moving atoms experience an inertial effect due to the rotating polarisation. The optical pumping for moving atoms skews the population of the sub-states, depending on the direction the atom is travelling. For negative frequency detuning, the sub-states of an atom moving towards a σ^- beam are skewed towards the g_{-1} state. The absorption of a σ^- photon is six times more likely than absorbing a σ^+ photon, so the atom receives momentum resisting it's motion. This is due to the Clebsch-Gordan coefficients for a $J = 1 \leftrightarrow J = 2$ transition illustrated in figure 4.6.

A similar argument can be applied for an atom moving towards a σ^+ beam to explain a resistive force slowing the atoms. This cooling mechanism is different to Doppler cooling and works for much lower velocities. The thermal equilibrium energy

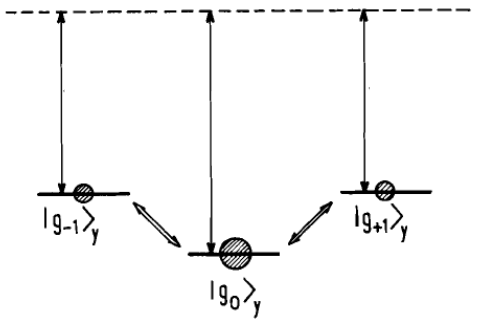

Figure 4.5: Relative distribution of stationary atoms between the sub-states for light shift for the $\sigma^+ - \sigma^-$. The steady state populations are 4/17, 9/17, 4/17, from left to right [27].

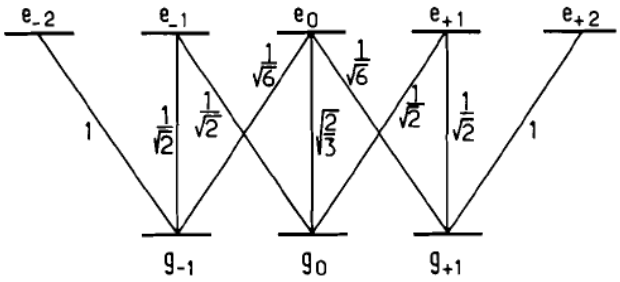

Figure 4.6: Clebsh-Gordon coefficients for a $J = 1 \leftrightarrow J = 2$ [27].

is given by,

$$k_B T = \frac{\hbar \Omega^2}{\delta} \left(\frac{29}{300} + \frac{254}{75} \frac{\Gamma^2/4}{\delta^2 + (\Gamma^2/4)} \right), \tag{4.1}$$

where T is temperature, k_B is Boltzmann's constant, $\hbar$ is the reduced Planck's constant, Ω is the Rabi frequency, δ is the detuning and Γ is the natural width of the excited state [27]. Equation 4.1 shows that colder atoms may be achieved by decreasing the laser intensity and increasing the detuning of the laser beams. Sub micro-Kelvin temperatures would be reachable with a pure polarisation gradient cooling technique.

4.2.2 Forming Optical Molasses

To implement polarisation gradient cooling on the MOT and maximise the effect of this, all magnetic fields must be eliminated. Experimentally, the magnetic field must be below to below 50 mG in magnitude [70]. The MOT coils must be switched off and background magnetic fields must be shielded from or cancelled. To minimise atom cloud expansion before polarisation gradient cooling becomes effective, the MOT coils must be turned off quickly, in around five to ten milliseconds.

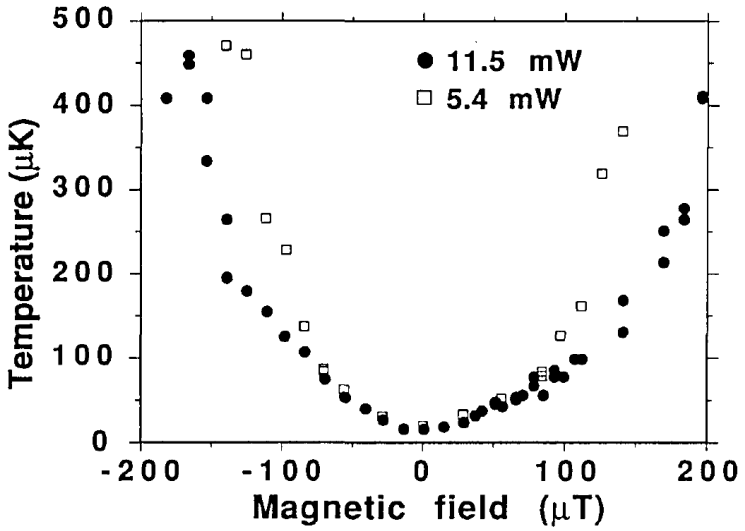

Figure 4.7: Graph taken from one of the first studies of optical molasses by Lett et al [70]. Demonstrates the effect of magnetic field on the cooling of sodium atoms in optical molasses.

4.2.3 Cancellation Coils

Cancellation coils were made to minimise the magnetic field in the laboratory. The earth's magnetic field is approximately 600 mG, and other sources such as the ion pump and the structure of the building have significant effects on the magnetic field in the experiment. A set of three coil pairs were designed and built to cancel the magnetic field over the path of the falling atom cloud. A secondary is to provide a small magnetic field in the axis the atoms fall in, i.e. a quantisation axis for the atom cloud during the interferometry sequence. Thus the vertical set of coils will be controllable by the timing sequence, with the ability to create a bias field by reducing the vertical cancellation coils current.

Helmholtz or Maxwell coils are commonly used produce a uniform magnetic field, but circular coils would be difficult to construct and to implement. Over the whole experiment circular coils would have to be large, and would obstruct access. With the requirement for the field to be uniform to within 10 mG from the MOT location to the detection chamber, using the Biot-Savart law it was calculated that square coils would produce a field with sufficient uniformity. A cuboidal design was made with dimensions 80 cm by 80 cm by 180 cm, with the x and y cancellation coils going the full height of the cuboid, and the z coils being placed at 50 cm and 105 cm. These coils can be seen in figure 4.8. This covers the trap region to the bottom of the detection area.

Figure 4.9 shows magnetic field maps for the three components of the magnetic field from these computations. Figure 4.10 shows a plot along the experimental axis of the experiment for the three components of the magnetic field. These calculations

Figure 4.8: Photo of the cancellation coils assembled for testing.

are overlaid on the Earth's magnetic field in Liverpool [71] (which are North/South 184 mG, East West -8 mG, Up/Down 456 mG) , so the cancellation can be seen.

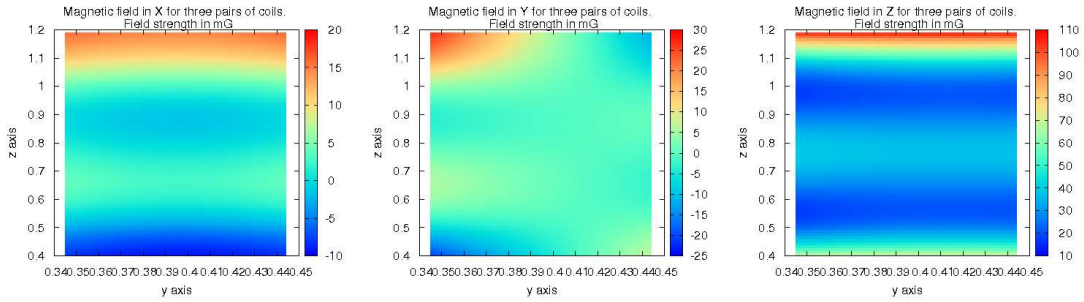

Figure 4.9: Colour maps of the x, y and z components of the cancellation coils magnetic field, calculated from Biot-Savart's law. The field from the coils is over laid on the Earth's magnetic field to demonstrate the cancellation. For all three plots, the x-axis is the y-position, centred at x = 0.4 m showing a range from 0.35-0.45 m in y. The z-axis is the z position from 0.4-1.2 m. The colour represents the strength of the magnetic field, with the scale in mG to the right of each plot.

It is important to cancel the magnetic field for the volume which is addressed by the interferometry pulses. Looking at the colour maps figure 4.10, horizontally the field is mostly constant in B_x and B_z components, varies less than 5 mG for the B_y component. Vertically, in the experimental range of $0.55 - 1$ m, the B_x and B_y components have variations of order 5 mG. In the B_z component there is a 20 mG variation. This can be seen clearer in the plots along the atom paths in figure 4.10. This design would

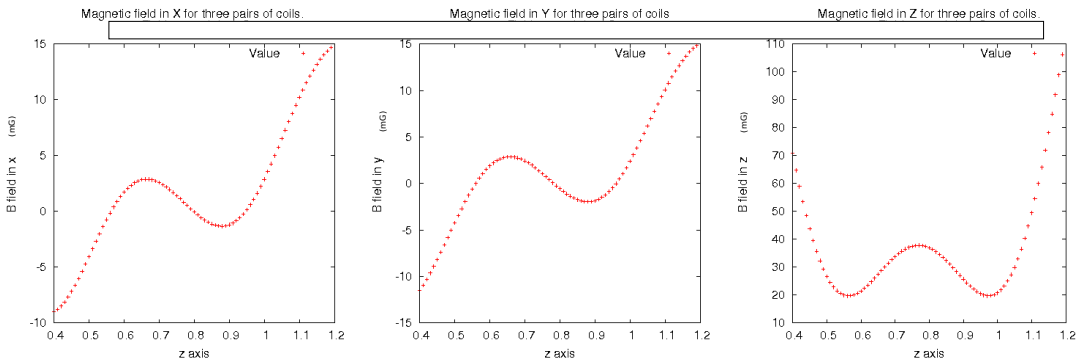

Figure 4.10: 1-D plots of the x,y, and z components of the cancellation coils magnetic field, calculated from Biot-Savart's law. The field from the coils is overlaid onto the Earth's magnetic field to demonstrate the cancellation. For all three plots, the x-axis is the z-position in the range 0.4-1.2 m. The y-axis is the magnetic field strength for the three components in mG.

lower the field to below 50 mG in the trapping region, and the Earth's magnetic field has been reduced by an order of magnitude.

The current required to cancel the field in the calculations are north/south $+16.15\ A$, east/west $+0.68\ A$ and up/down $-24.69\ A$. The coils to produce these were constructed from 20 conductor ribbon cable, terminated by IDC connectors with the ribbon cable displaced by one strand along on one of the terminations. One loop was required for east/west with two coils in parallel for the north/south and up/down coils, with the two pairs run in series. Power was supplied with constant current power supplies.

The cancellation coils cannot compensate for large anisotropies in the magnetic field. Whilst the Earth's magnetic field was the main source of field, other sources, such as the ion pump, rebar in the building, steel of the optical table and the vacuum chamber were significant and had variations in field of the order 100 mG. As the vacuum chamber was sealed, measurements along the clouds path was not possible without disassembling the vacuum. It was decided to set the coils to roughly cancel the magnetic field based on magnetic measurements around the MOT region, and they would be fine tuned by varying them to minimise the temperature in the future.

4.2.4 Atom Drop

To release atoms from the optical molasses, there is a common procedure to achieve this [35] [25]. First the MOT anti-Helmholtz coils must be turned off. The sudden change in magnetic field will induce eddy currents in the vacuum chamber. These will induce magnetic fields of their own, until they have decayed, which takes of order ten milliseconds. Next the MOT laser frequency should be further detuned to the molasses frequency, and a molasses cooling stage should last for a few milliseconds. Increasing the detuning decreases the equilibrium temperature that is reached which is described

by equation 4.1.

From the optical molasses, the beam intensity should be ramped down adiabatically over the course of another few milliseconds. Finally the pumping frequency should be left on longer than the molasses frequency to ensure the atoms are in the F=3 state. A provisional sequence for the release of the atoms can be seen in figure 4.11. After this sequence the atoms are free to fall under gravity.

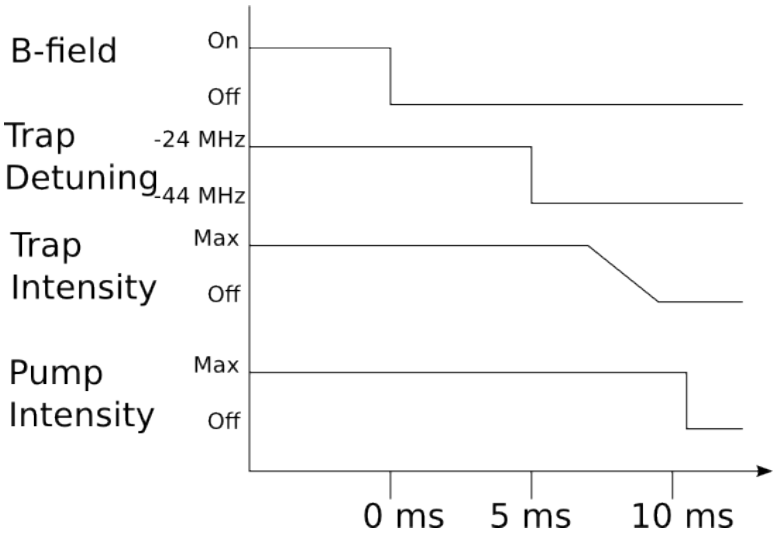

Figure 4.11: An illustration of the timing sequence for forming molasses.

4.2.5 Frequency Requirements and Optics

The optical molasses requires the trapping frequency to be further detuned, and to release the atoms from the optical molasses, the laser beams need intensity control on the millisecond time scale. These can be seen in figure 4.12.

The molasses and MOT frequencies are generated from the same source. Both the MOT/molasses frequency and the pump frequency are collimated to 4 mm diameter beams, and combined on a PBS. After this, the beam is split into three, two making up the horizontal counter-propagating pair, carrying one sixth of the trap beam power each, with the remaining two thirds of the trap beam power for the diagonal beams. These beams are then sent up to the MOT breadboard, where the beam carrying two thirds of the trap beam power is split into four equal parts. The final splitting for each pair of counter-propagating beams is done on one PBS, so the balance along that axis can be altered. It was found necessary to use precision rotation mounts for the half wave-plates to allow fine tuning of the power balance. To minimise differences in the trap beams in the MOT, care was taken to make all of the beam paths pairs the same length, by 'dog-legging' the beam where necessary. To achieve this, 90° prism's were mounted on translation stages so the length could be altered with minimal disruption to the MOT alignment. A schematic of the optical circuit can be seen in figure 4.13

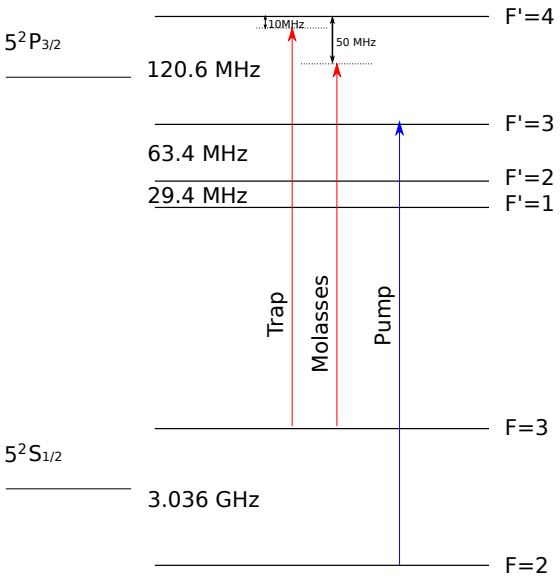

Figure 4.12: Rubidium energy level diagram with the required frequencies for the MOT and the optical molasses.

with a photograph of a segment of the optical circuit in figure 4.14.

4.3 State Selection

The effect of magnetic fields on an interferometer can be reduced by preparing the atoms in the $m_F = 0$ state, which to first order is unaffected by magnetic fields. The released atoms are distributed amongst the magnetic sub-states of the $5S_{\frac{1}{2}}$ F = 3 state. A magnetic field in the vertical direction of order one hundred milli-Gauss is created by the cancellation coils to provide a quantisation axis.

To prepare the atoms in the $m_F = 0$ state, an optical pumping method was chosen, as illustrated in figure 4.15. First, the magnetic sub-states are split by the magnetic field. This splitting is 160 kHz/G per m_F for the F=2 state [50] with the bias field in the vertical direction having a value of up to 450 mG. A beam stimulating the $S_{\frac{1}{2}}F = 2 \rightarrow P_{\frac{3}{2}}F = 2$ transition is inserted with its polarisation carefully tuned to be perpendicular to the magnetic field. This excites dipole transitions, which are forbidden for the atoms in the $S_{\frac{1}{2}}F = 2, m_F = 0$ state. The atoms may then de-excite from $P_{\frac{3}{2}}F = 2$ state into either the $S_{\frac{1}{2}}$ F = 2 or 3 states.

The hyperfine frequency beam stimulating the $S_{\frac{1}{2}}F = 3 \rightarrow P_{\frac{3}{2}}F = 2$ transition passes along the same path as the the optical pumping frequency, and recycles any atoms that fall into the $S_{\frac{1}{2}}$ F = 3 state. These beams are pulsed alternatively for 10 μs several times, and the atoms accumulate in the $S_{\frac{1}{2}}$ F = 2, $m_F = 0$ state. These beams are retro-reflected to minimise any momentum imparted on the atoms by this method. Finally a blow-away pulse from the MOT beams will be applied to remove any atoms left in the $S_{\frac{1}{2}}$ F = 3 state. This will be achieved by shuttering off all but one of the

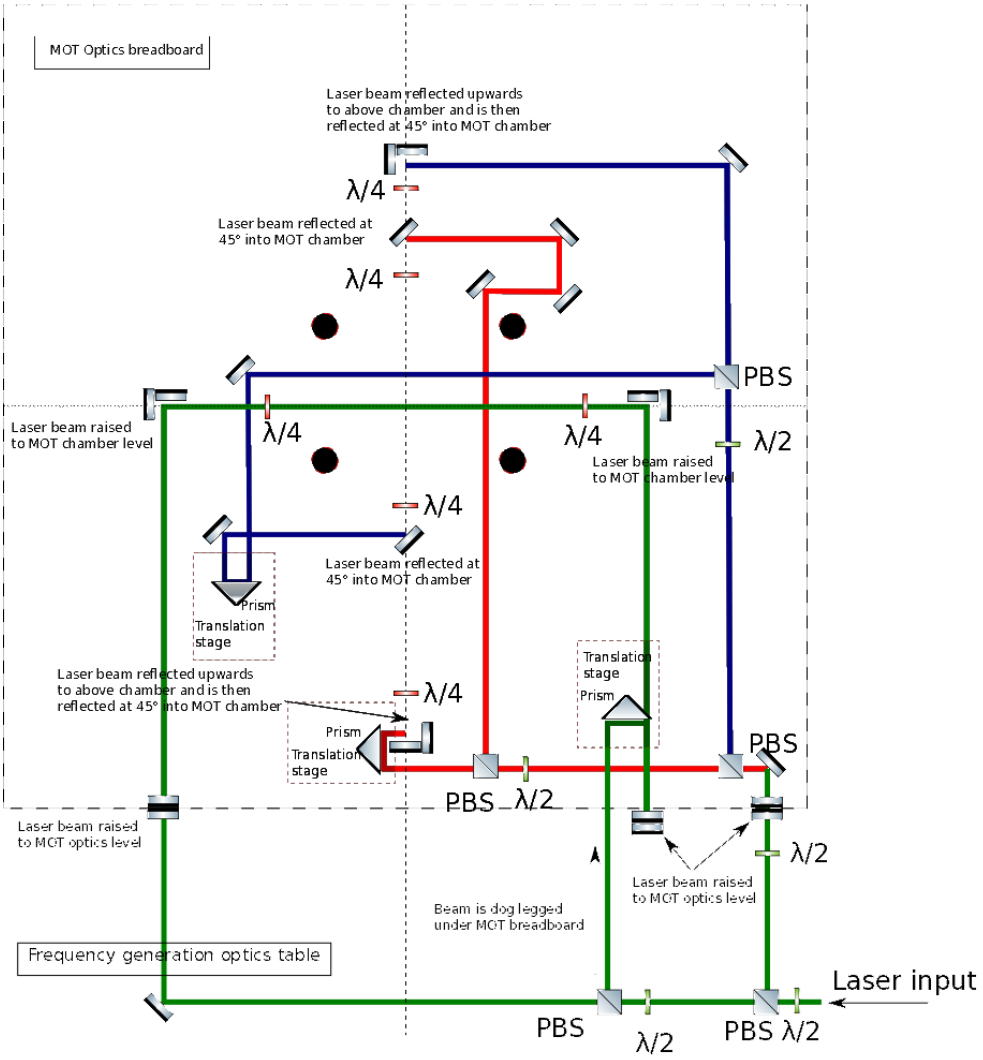

Figure 4.13: Schematic of the MOT optics for the prototype atom interferometer.

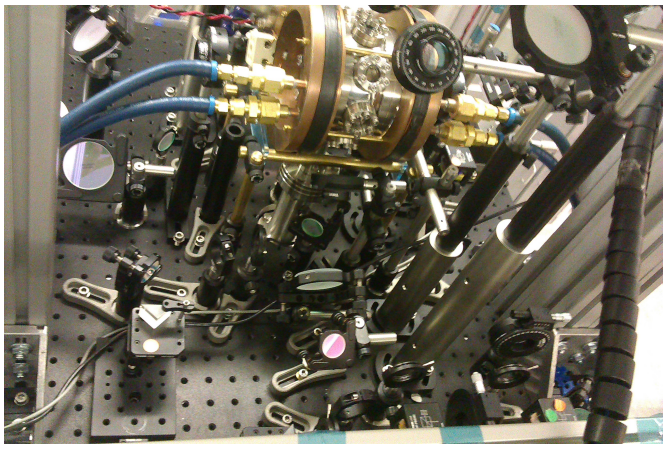

Figure 4.14: Photograph of the MOT optics for the prototype atom interferometer.

MOT beams.

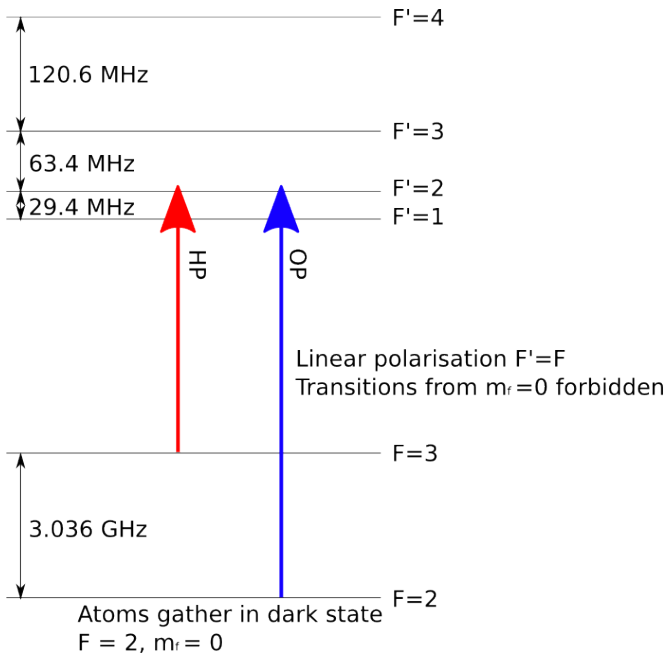

Figure 4.15: Energy level diagram for optical state selection. Atoms gather in the dark state, F = 2, $m_F = 0$.

4.4 Raman Pulses

The Raman pulses are used in both the 1-D velocity selection and in the interferometry sequence. Two laser frequencies stimulate transitions between the ground states of the rubidium atoms via a virtual state. The required laser frequencies are outlined in a sketch of the energy levels in figure 4.16.

The polarisation is important to limit the Raman transition stimulated. As the atoms are already prepared in the $m_F = 0$ state (the bias field first applied in the state selection is still on at this stage to split the Zeeman states), it is also a requirement to keep the atoms in a $m_F = 0$ state. The only two polarisation combinations that achieve this are if Raman 1 and 2 are identically circular polarised and they are counter propagating, or if Raman 1 and 2 are linearly polarised and they are retro-reflected in the orthogonal polarisation as well as the atoms having a non-zero velocity [72]. The former choice of polarisations was selected, due to our combination of Raman beams on a PBS, dictating that they have orthogonal polarisations.

After the Raman beams are combined on a PBS, they are delivered to the experimental chamber by a 10 m polarising maintaining fibre. This is done to produce the cleanest possible Gaussian laser beam. Some non-Gaussian type behaviour persists due to cladding modes, in which light propagates down the fibre cladding, not the fibre core. This is attenuated by using longer fibres. The beams are expanded to 10.8 mm

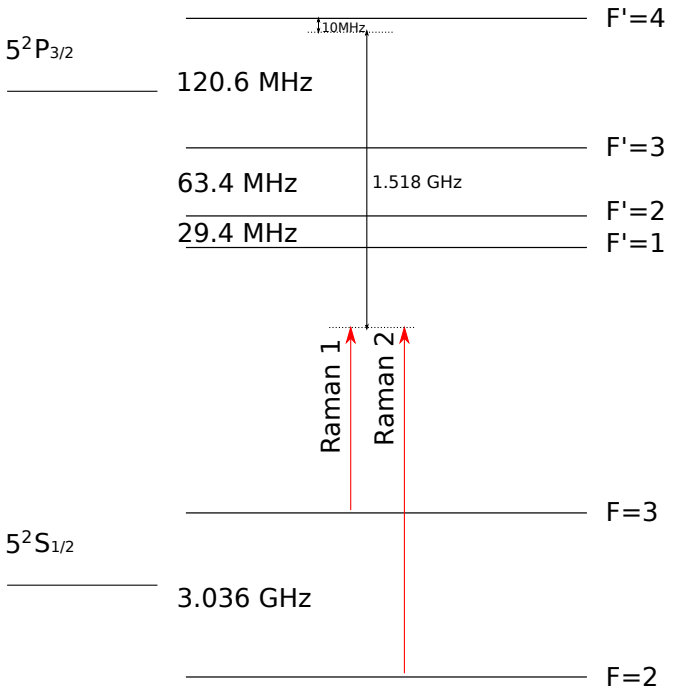

Figure 4.16: Energy levels for the Raman transitions.

diameter by the fibre optic collimator, with the two components having orthogonal linear polarisation. The beam travels down through a quarter wave-plate, and then through the vacuum chamber. The beam then passes through a quarter wave-plate and is retro reflected off a mirror. The collimator, quarter wave-plate and mirror were chosen to be as flat as possible to minimise the wave-front aberration of the Raman beam. This is important so that the whole atom cloud has the same phase imparted on them by the laser. However the two window ports on the vacuum system were not chosen for flatness, and will need to be upgraded. The collimator is a Sulkhamburg 60FC-L-0-M60L, with a $\frac{\lambda}{20}$ wave-front aberration. The mirror is a Newport 10Z40BD.2, with a $\frac{\lambda}{20}$ wave-front aberration. The quarter wave-plate is a Edmund Optics 46-410, with a $\frac{\lambda}{10}$ wave-front aberration.

The launch platform for the Raman launch can be seen in figure 4.17. The fibre is mounted on a x-y micrometer stage in a tip/tilt mount. The x-y micrometer stage can be used to move the beam to coincide with the trapping point of the MOT. The tip/tilt mount is used to align the measurement axis of the interferometer, which to measure gravity should be vertical. Any angle between the Raman axis and vertical will reduce the phase difference measurement as such,

$$\Delta\phi = \mathbf{g}.\mathbf{k_{eff}}T^2 = gk_{eff}T^2 cos\theta \approx gk_{eff}T^2(1-\theta^2) \tag{4.2}$$

An angular alignment tool is used to minimise the angle to the vertical axis [73]. Figure 4.18 illustrates this tool. The alignment tool utilised a beam sampler (Laser 2000

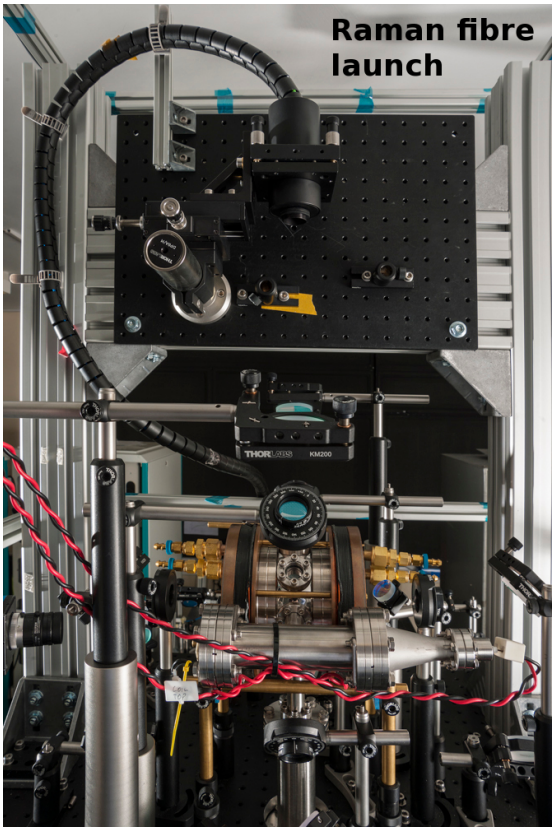

Figure 4.17: Photo of the Raman launch platform.

BS4-25.4C03-10-550, parallelism of 24 μrad), and corner cube (Thorlabs PS976M-B, beam deviation of 14 μrad) and a lens to focus a pair of counter propagating beams onto a CCD with pixel size 5 μm. The downwards travelling beam is split by the beam sampler and retro-reflected by the corner cube back through the beam sampler and then focused onto the CCD by the lens.

The upward travelling beam is split by onto the CCD by the lens. If both beams are perfectly parallel then they will be focused onto the same point on the CCD.

To align the downward propagating beam to the vertical, the mirror at the bottom is replaced by liquid surface of paraffin. This forms a mirror perpendicular to the vertical. The angle of downwards travelling beams may then be optimised to overlap with the beams in the CCD, which aligns the downward travelling beam vertically.

Replacing the mirror at the bottom and using the tool to ensure both beams are parallel completes the angular alignment. This gives an estimated angular error of 27 μrad and a systematic error in phase of 7.7×10^{-10}, limiting the accuracy of gravity measurements. The constructed tool can be seen in figure 4.19.

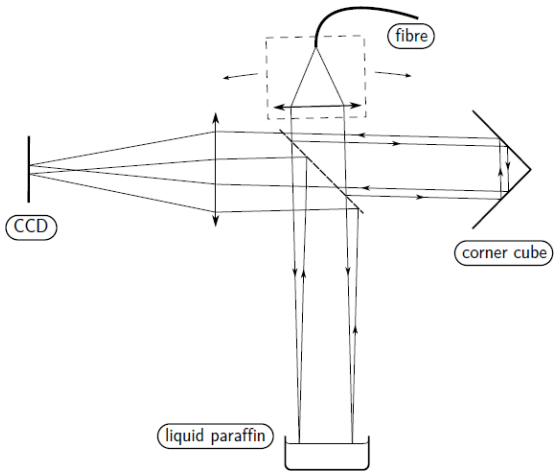

Figure 4.18: Sketch demonstrating the geometry of the alignment tool [73].

Figure 4.19: Photo of the alignment tool.

4.4.1 1-D Velocity Selection

The Raman beams will address a smaller velocity profile than that described by atoms at micro-Kelvin temperatures, with a velocity width

$$\Delta v/c = \Delta\nu/(\nu_1 + \nu_2), \tag{4.3}$$

where $\Delta\nu$ is the Raman linewidth, and ν_1 and ν_2 are the two frequencies of the Raman beam. Thus, a Raman selective pulse sequence will be applied before the interferometry sequence.

This increases the contrast of the interferometry fringes. The required laser frequencies are shown in figure 4.20.

Figure 4.21 summarises the method. First a blow-away pulse, $S_{\frac{1}{2}}F = 3 \rightarrow P_{\frac{3}{2}}F' = 4$ is applied from just one of the six MOT beams, pushing any atoms remaining in $S_{\frac{1}{2}}$ F = 3 away from the main cloud. Using just one beam, momentum is applied to the atoms and they are pushed out of the region. Next a Raman π pulse is applied to the cloud, transferring atoms with the limited velocity range into the $S_{\frac{1}{2}}$ F = 3 state. A blow-away pulse $S_{\frac{1}{2}}F = 2 \rightarrow P_{\frac{3}{2}}F' = 1$ is then applied pushing atoms in the $S_{\frac{1}{2}}$ F = 2 state remaining away from the cloud. At this point the atoms can be used in the $S_{\frac{1}{2}}$ F = 3 state, or another Raman π pulse can be applied followed by a blow-away from $S_{\frac{1}{2}}$ F = 3, for a better velocity selection. Figure 4.22 summarises the state selection sequence.

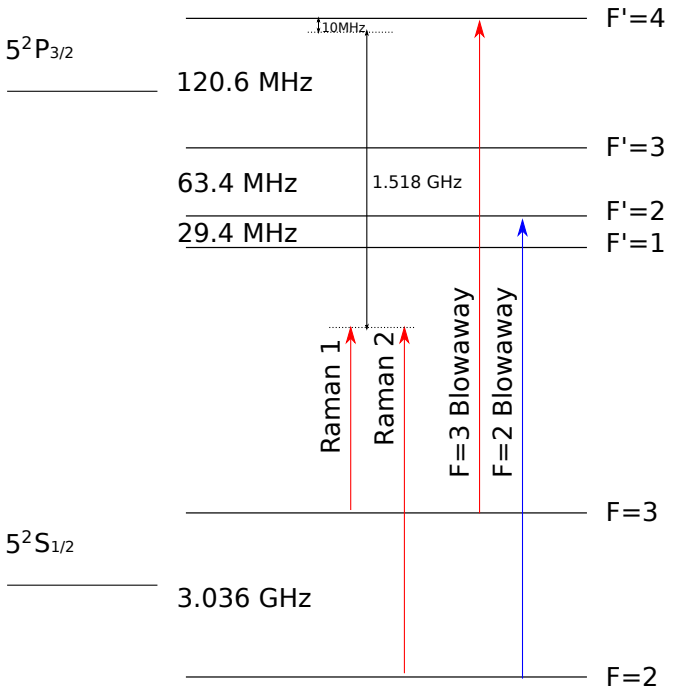

Figure 4.20: Energy level diagram showing the required frequencies for the 1-D velocity Raman selection.

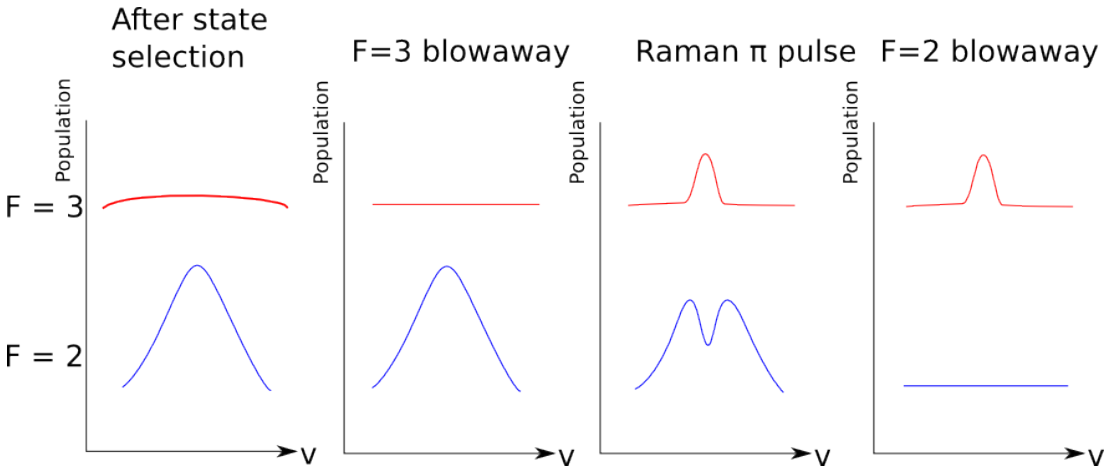

Figure 4.21: Raman 1-D velocity selection. Populations of the atoms between the two ground states as a function of velocity.

4.4.2 Raman Pulse Sequence

To maximise the contrast of the interferometry fringes, the ideal length of $\frac{\pi}{2}$ and π pulses must be determined. By altering the Raman pulse duration and measuring the number of atoms in the $S\frac{1}{2}$ F = 3 state, the Rabi cycles may be measured and the Rabi frequency may be determined, giving the length of $\frac{\pi}{2}$ and π pulses. Raman pulses of different durations will be applied after state selection and velocity selection, and the proportion of atoms in the F=3 state is measured. Doing this for different times T

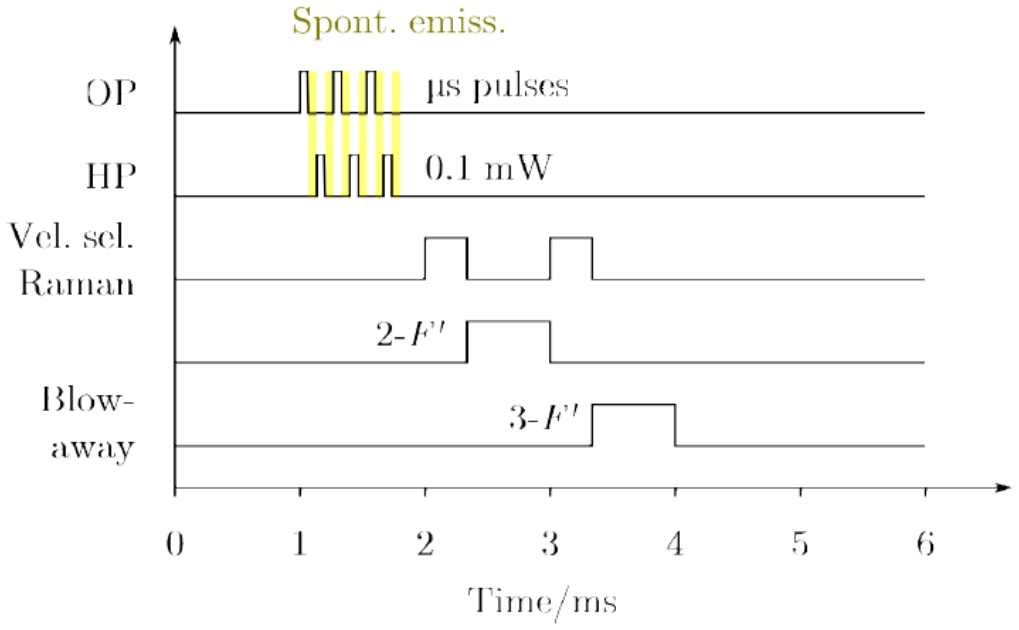

Figure 4.22: Sequence for state selection.

traced out the Rabi cycle, for which half of one is the time of a π pulse, and a quarter of a cycle, the duration of $\frac{\pi}{2}$.

The interferometry sequence will be applied, of a $\frac{\pi}{2}$ pulse, π pulse and then a $\frac{\pi}{2}$ pulse, each separated by time T. The Doppler shift experienced by the atoms as they accelerate under gravity is counteracted by chirping the RF generator, to change the frequency difference of the two Raman beams.

4.5 State Detection

The state populated by the atoms is measured using fluorescence techniques [74]. The two frequencies required for the state detection are shown in the energy level diagram figure 4.23.

The detection and repump frequencies are expanded to 4 mm, combined on a PBS, and inserted through the detection chamber normal to the window, and retro-reflected to increase intensity. A PMT is positioned at an angle (to prevent reflections), with a lens system to focus the fluorescence of the atoms passing through the detection beam. A sketch of this can be seen in figure 4.24. The whole of the optics table will be surrounded by a cage with blackout material attached.

Blackout material is necessary as the PMT used is very sensitive (Hammamatsu R943-02). This was chosen because of its low dark photon count of less than 20 photons per second, enabling single photon counting to minimise the statistical error.

A detection sequence such as the following will be applied [25]. A detection fre-

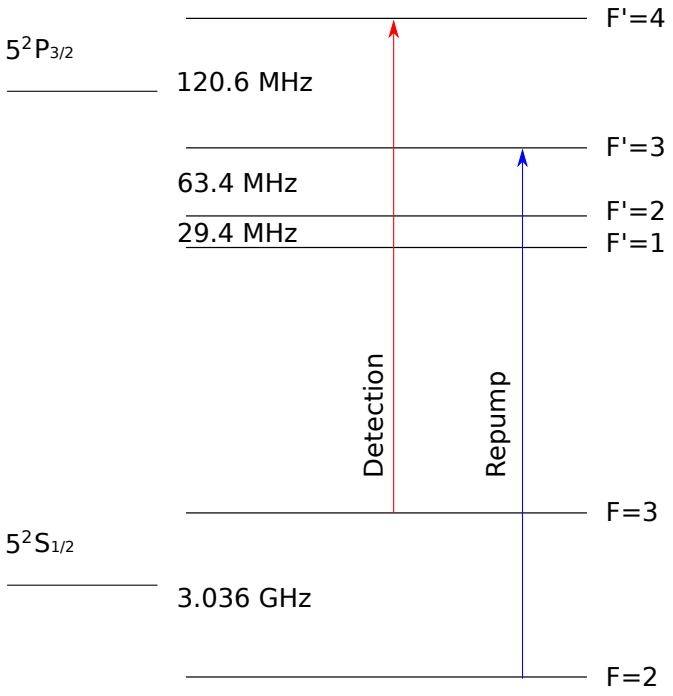

Figure 4.23: Energy level diagram for the state detection.

quency pulse fluoresces the atoms for $\sim$ 400 μs. The integrated PMT signal in this duration is proportional to the number of atoms in F = 3 plus the background vapour fluorescence. Then the repump pulse fluoresces the atoms for 200 μs pumping all the atoms into the F = 3 state. Finally a detection frequency pulse fluoresces the atoms again for 400 μs. The integrated PMT signal in this duration is proportional the total number of atoms plus the background vapour fluorescence. The background count of the PMT can be measured and subtracted from these two signals. The result of the interference is a fraction of atoms in F = 3 after the interferometry pulses. The fraction of atoms left in state F = 3 can be related to the gravitational strength using equation 2.25, which has been modified here to account for an non-idealised contrast C,

$$P_{F=3} = \frac{1}{2}(1 + Ccos(k_{eff}gT^2 + \phi)), \tag{4.4}$$

and ϕ is the total phase due to the lasers. The contrast in a real interferometer is limited by imperfect Raman population transfer and fluorescence of background atoms.

At the end of the interferometry sequence, the atoms wave-packets are spatially overlapped. However they differ in momentum by $\hbar k_{eff}$, so between the last interferometry pulse and the detection pulse, the wave-packets accumulate a spatial separation. The timing of the detection pulse needs to be timed to reach the best possible contrast.

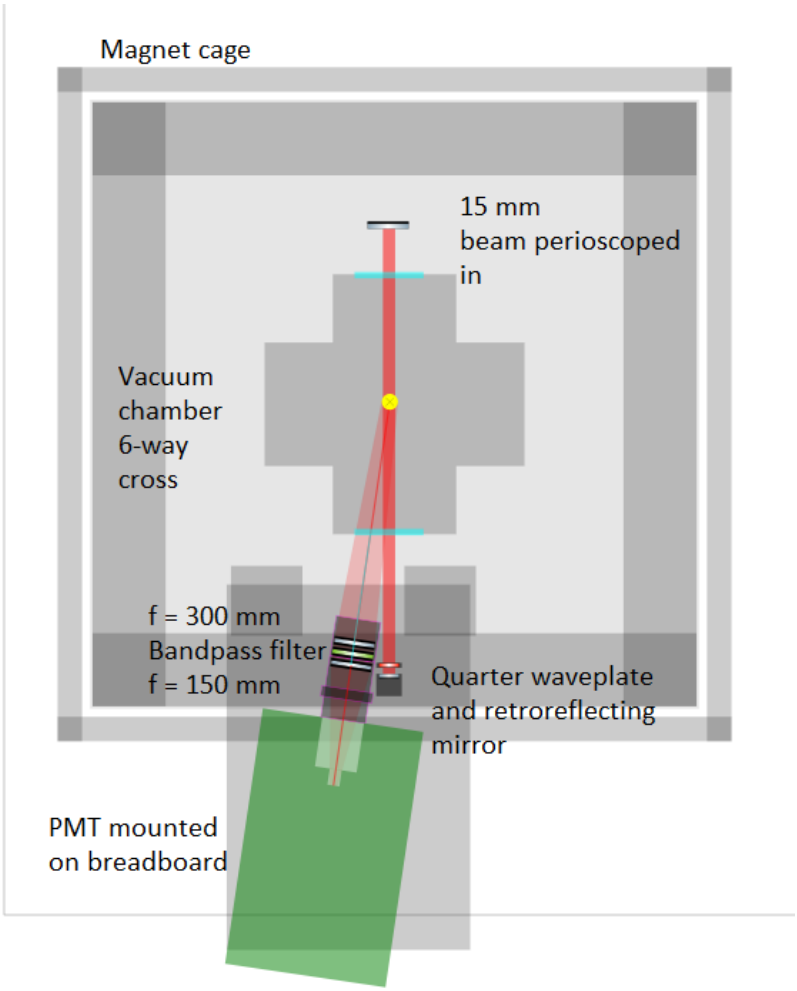

Figure 4.24: Sketch of detection system.

4.6 Summary

The design of a prototype atom interferometer has been presented, which has been constructed and is being commissioned. This involved constructing a new vacuum chamber, which had the MOT developed in the previous chapter at the top as a ultra-cold atomic source for a atom drop interferometer. Magnetic coils were designed and implemented to cancel the background magnetic field for the MOT, to allow for polarisation gradient cooling as a further cooling mechanism for the cold atomic source. An optical state selection method was discussed, as well as a one dimensional velocity selection along the interferometry axis, which will make the atoms magnetically insensitive and improve the contrast from the interferometry pulses respectively. The generation of the Raman interferometry pulses, and a state detection scheme was also discussed. With all of these methods, the laser frequency, polarisation and delivery requirements were discussed. The following chapter will describe how all of these requirements are met with a unique laser frequency generation scheme.

Chapter 5

Laser System

5.1 Laser System

The previous chapter outlined all the required frequencies to implement the atom interferometer. These are summarised in figure 5.1.

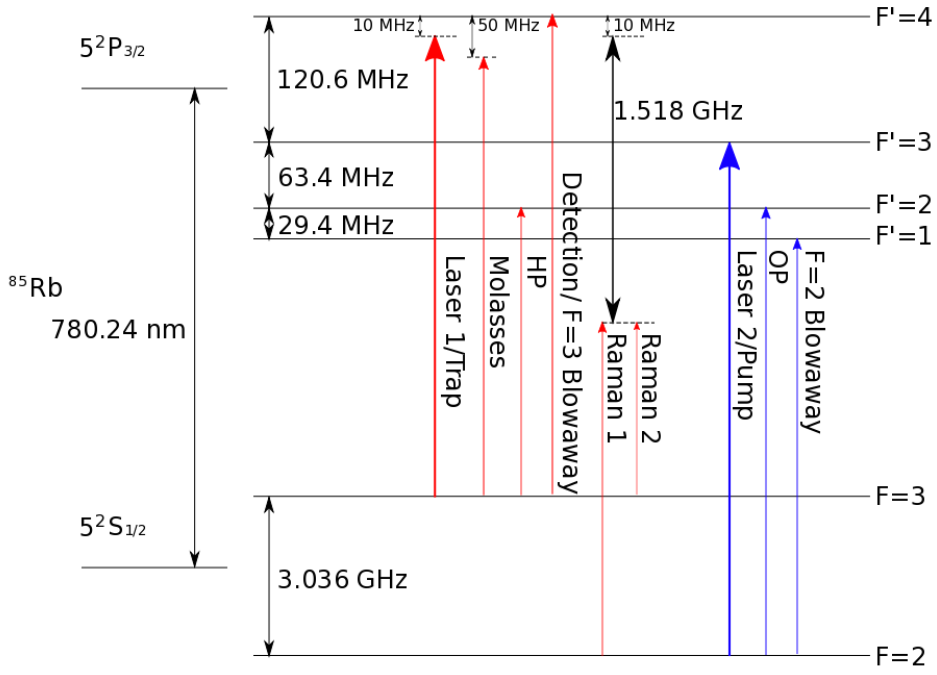

Figure 5.1: Energy level diagram with required transitions for the atom interferometry with ^{85}Rb. Frequencies derived from the trap laser are illustrated with red arrows, and those derived from the pump are blue.

It was desired for the sake of simplicity to use as few lasers as possible for the laser system. The ^{85}Rb ground state splitting is $\sim$ 3 GHz, with the difference in frequency between hyperfine states being no more than 200 MHz. AOM's able to shift

the frequency of the laser beam by 3 GHz have low efficiency and are expensive, AOM's of up to 200 MHz are more efficient and affordable. Because of this, the laser system requires two ECDL's, one to start from each of the two ground states of ^{85}Rb. Using AOM's all the required frequencies can be generated from two ECDL's, which can be seen in figure 5.1.

All of the required frequencies for the atom interferometer are generated in a system based on the two ECDL's described in section 3.2.2 and five AOMS. The AOMs are three 80 MHz AOM's (Gooch & Housego 3080-122), one 200 MHz AOM (Crystal Tech 3200 124) and one 1.5 GHz AOM (Brimrose 410-472 7070). As well as frequency control, AOM's allow for timing and intensity control of the beams.

5.1.1 Gaussian Optics

Geometric optics is not sufficient to describe the properties of lasers. The properties of laser beams are described well by the paraxial approximation of the Helmholtz equation [75]. The lowest order solution gives Gaussian TEM_{00} beam modes. A consequence of this is that laser beams will always have some divergence or convergence. A laser beam focused with a convex lens does not focus down to a point but to a minimal width. If this minimal width occurs in both x and y at the same position, it can be said to be a beam waist. At a beam waist laser beams have a flat wave-front [57]. Figure 5.2 illustrates this.

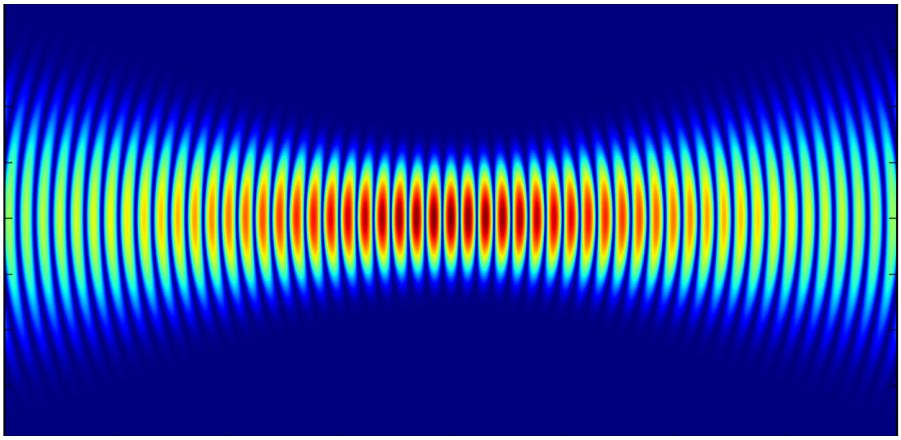

Figure 5.2: An illustration of a Gaussian beam being focused into a beam waist [76]. Colour represents intensity. Only at narrowest point is the wave-front flat.

The laser beam emitted from ECDL's is elliptical and thus astigmatic, diverging at a different rate on its fast and slow axes, as discussed in section 3.2.1. Whilst this was used for the MOT in chapter 3, this was not suitable for the laser system for the atom interferometer, nor many of the techniques used in the interferometer. For example, the AOM's used in the laser system perform optimally when the beam waist is formed in the active region of the AOM. However, an elliptical beam will not form a beam

waist.

This can be seen by taking a beam profile along the beam propagation axis. After reducing the intensity of the laser beam with neutral density filters, a bare CCD camera was inserted into the laser beam to directly image the beam. Typically the beam had to be attenuated by a factor of at least 10^5, which was done to prevent overexposing the CCD. The images were converted into the pixel values using CImg, and histograms of the sum of columns and sums of the rows were fitted with a Gaussian plus background for the x and y fits respectively. Errors on the Gaussian widths were given by the error on the fit. An example of this can be seen in figure 5.3, which is a beam profile of the trap ECDL after a f = 200 mm lens. The beam minimal in y occurs 23 mm before the beam minima in x.

The lines fitted to figure 5.3 is for the equation describing Gaussian beam widths [57], which is

$$w(z) = w_0 \left[1 + \left(\frac{\lambda z}{\pi w_0^2}\right)^2\right], \tag{5.1}$$

where $w(z)$ is the $1/e^2$ beam radius at z, z is the axial distance from the laser beam-waist, w_0 is the beam-waist radius and λ is the wavelength of the laser.

Around the beam waist the beam profile curvature significantly diverges from the description given by geometric optics. This region is called the Rayleigh range, and is characterised by z_R and

$$z_R = \frac{\pi w_0^2}{\lambda}. \tag{5.2}$$

This Rayleigh range can extend for significant distances. For example, a beam-waist $1/e^2$ diameter of 1 mm at wavelength of 780 nm, the Rayleigh range extends to 1 m, so Gaussian optics needs to be taken into account.

Laser beams are not quite Gaussian TEM_{00}, and have other modes present. To take this into account, equation 5.1 is modified with a beam quality factor M^2 as

$$w(z) = w_0 \left[1 + \left(\frac{M^2 \lambda z}{\pi w_0^2}\right)^2\right]. \tag{5.3}$$

This beam quality factor is a coefficient to take into account the beam higher order modes that occur in laser beams. By definition a $M^2 = 1$ is a perfect Gaussian mode, whilst $M^2 > 1$ describes any differences from this [77]. The further a beam diverges from $M^2 = 1$, the larger divergence and beam waist it has. These higher order modes focus after the TEM_{00} modes, which can be seen effecting the accuracy of the Gaussian fit after the focal point in figure 5.3

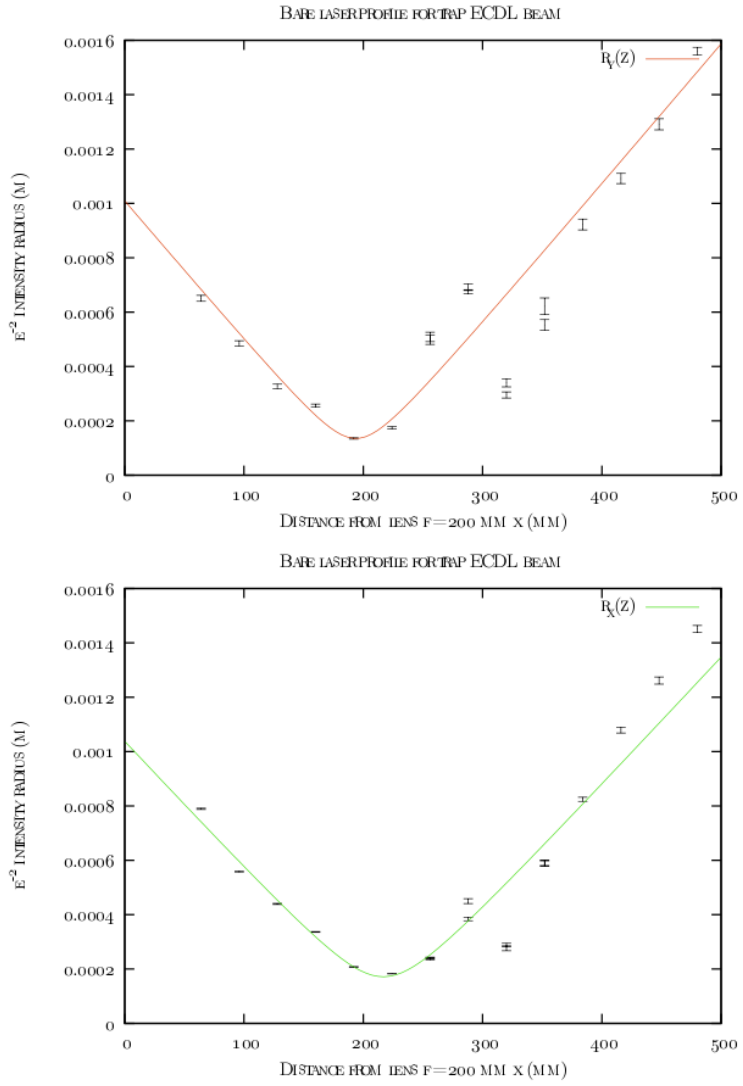

Figure 5.3: Graph of beam profile for the trap ECDL. The widths were measured by fitting a Gaussian to images of the beam taken. The beam-waists position on the z axis differ by 23 mm, much larger than AOM the beam-waist is supposed to be located in. The lines are fits of a Gaussian beam profile.

5.1.2 Acousto Optical Modulators

An acousto-optical modulator (AOM) is a telecommunications device, containing a birefringent crystal, whose refractive index changes with pressure. A constant frequency sound wave created by a piezoelectric electric transducer travels through the crystal creating periodic variations in refractive index and hence a diffraction grating. Light incident on the AOM may be optically diffracted at the Bragg angle by the diffraction grating, which is given by

$$sin\theta = \frac{m\lambda}{\Lambda}, \tag{5.4}$$

where θ is the angle of deflection, λ is the wavelength of the laser, Λ is the wavelength of the sound waves and m is the order of diffraction [78]. As the sound wave is travelling through the crystal, the laser is diffracted by a moving diffraction grating. As a result of this, the laser beam is Doppler shifted by the frequency of the sound wave F,

$$f \rightarrow f + mF. \tag{5.5}$$

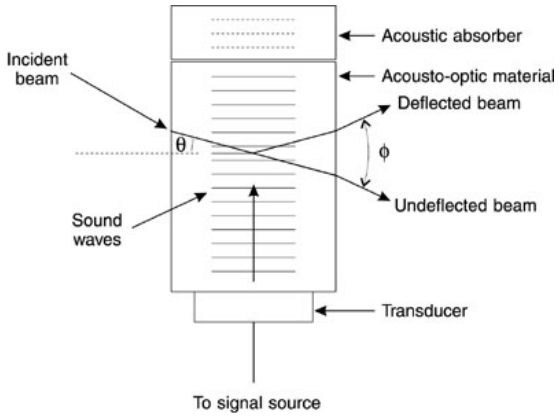

Figure 5.4: Sketch of an acoustic optical modulator. The angle θ is the Bragg angle, and ϕ is twice that value. In this example the diffracted laser beam is increased in frequency. If the AOM was rotated so that incident beam is at minus the Bragg angle as this diagram shows, the frequency would be decreased.

The efficiency of AOM's are dependent by the angle the beam passes through the device, the RF power and the RF driving frequency. As well as passing the beam through at the Bragg angle, the AOM have an active area, 500 μm for the Gooch & Housego, 150 μm for the Crystal Tech AOMs, but much smaller at 76 μm for the Brimrose. This requires precision Gaussian optics to match the beam waist size with the active aperture size of the AOM, at the exact location of the active region.

5.1.3 Alignment and Characterisation of an 80 MHz AOM

For the purpose of the commissioning of the AOM's, the beam was fibre launched to correct the astigmatism and provide a beam with M^2 close to 1. Initially the beam profile of the laser was taken. The beam was aligned to travel directly over the holes on the optical table, at a constant height. A convex lens was inserted into the beam, taking care not to divert the beam from its previous path. The beam was then attenuated several orders of magnitude (4-7), so a CCD camera could be safely inserted image the beams. This CCD was mounted on an optical rail, so that the CCD could be translated along the beam length using the rail. Images were taken along the length of the beam,

as the beam focused the attenuation was increased to account for a more intense beam, to avoid overexposing the images and also damaging the CCD. Each image was fitted with a Gaussian width along the x and y axis, and these data points were used to fit a Gaussian width profile to extract the $1/e^2$ width. Figure 5.5 shows one of these profiles for one of the AOMs.

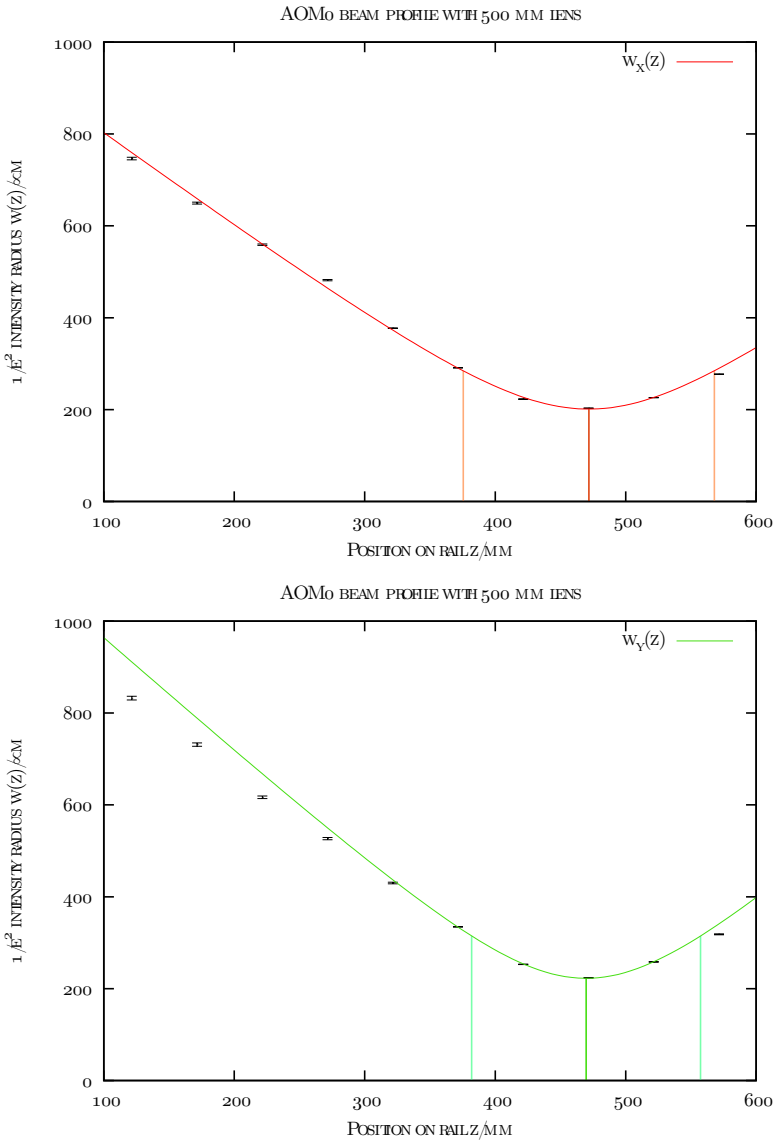

Figure 5.5: Beam profile for the beam at AOM0's location with a f=500 mm lens, in x and y. Both are fit to a Gaussian beam radius.

The data points are fit with equation 5.3. The beam profile identifies the beam waist position and puts it at between 400-440 μm which matches well with the active region of the AOM.

Once the location of the beam waist of the beam was identified, the AOM's are mounted on micrometer rotation stages. Rotating the beam to the Bragg angle, the beam can be seen to be diffracted at twice the Bragg angle. This can be seen in figure

5.6. It is visible that the centre of the zeroth order is missing intensity, which has been diffracted into the first order. Multiple orders m can be diffracted, and the fraction diffracted into each is dependent on the angle the beam crosses the AOM.

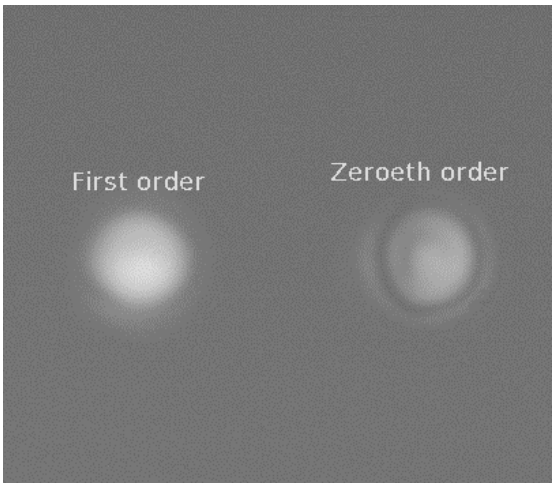

Figure 5.6: Photo of the first and zeroth order diffraction from the AOM.

The AOM is most efficient at the Bragg angle and the micrometer rotation stages were used to optimise this angle. This can be seen in figure 5.7, with the $\pm$ 1 diffracted orders. This data was acquired at 0.2 W RF power.

The power supplied by the RF driver can be varied. Increasing the RF power initially increases the efficiency of the AOM, linearly at first, but the device saturates at high power. Increasing the power past this point will damage the device, with the maximum power of approximately 1 W, which can be seen in figure 5.8. The diffraction efficiency achieved was slightly more than the stated efficiency of 85%.

Finally, AOM's are optimised at a particular design frequency, but will operate within a bandwidth. The effect of this can be seen in figure 5.9. The peak efficiency as expected is at 80 MHz. The efficiency either side of 80 MHz is unsymmetrical, which is particular to the exact alignment. These AOM's have a quoted bandwidth $\pm$ 20 MHz from the central frequency to -3 dB.

5.1.4 Double Pass AOMs

An AOM can diffract the laser beam on multiple passes to achieve frequency shifts of multiples of the driving frequency. Double passed AOM's are used, as they eliminate the change in laser beam path when the driving frequency is changed [79]. Figure 5.10 is a sketch of the basic optical principle. The incoming beam passes through a PBS with a defined linear polarisation. It is then focused to form a beam-waist in the AOM, which diffracts the beam into the first order mode. A second lens then re-collimates the beam, which is retro-reflected through a quarter wave-plate to rotate the polarisation of the beam to be perpendicular to the input beam. This retro-reflected beam retraces

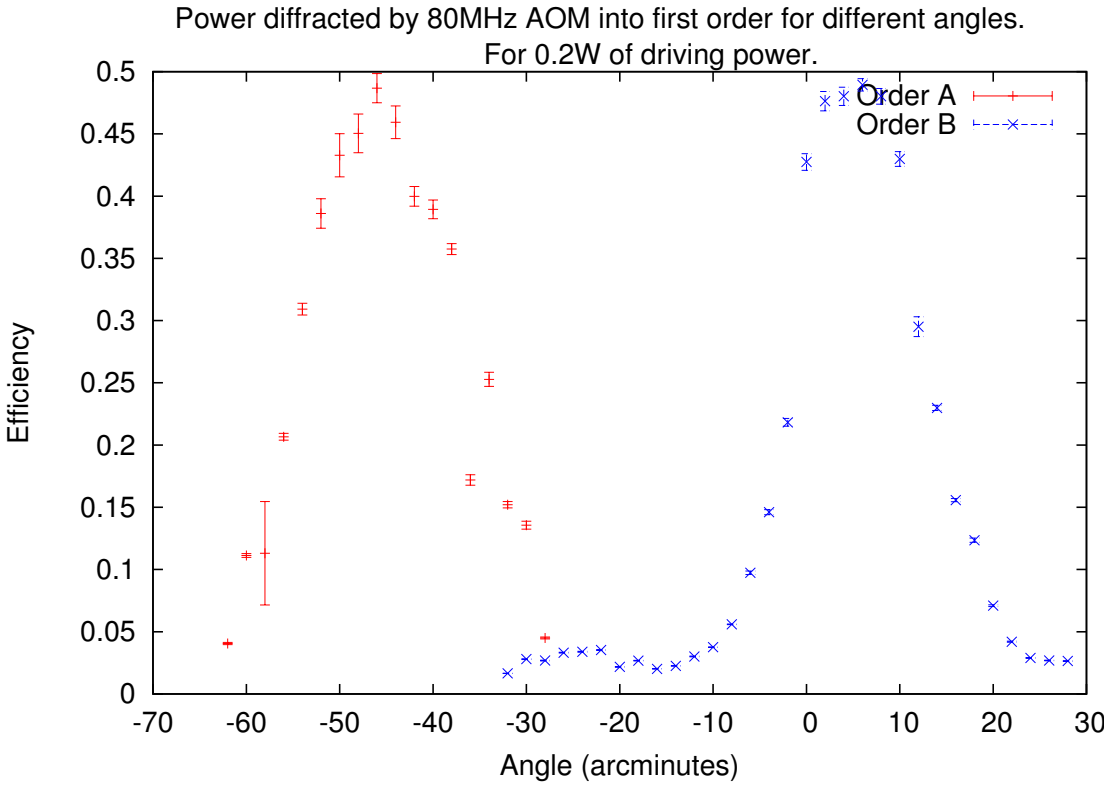

Figure 5.7: Graph of AOM efficiency with angle for a Gooch & Housego 80 MHz AOM. The angle of the AOM was rotated and the fraction of the power diffracted into the $m \pm 1$ orders was measured. At this stage the sign of the order was unknown, so they are labelled A and B.

the path and is re-focused into the AOM and is diffracted a second time, shifting the frequency again. The beam is then refocused and reflects off the PBS, with a frequency shift of double of the driving frequency of the AOM.

The Gooch & Housego AOMs are driven by a Novatech 409B DDS, outputting up to +4 dBm, which is amplified up to +30 dBm by a Minicircuits amplifier. The Brimrose AOM is driven by a Rohde Schwartz SMA100a signal generator which outputs +10 dBm, and another Minicircuits amplifier is used to raise the power to +30 dBm. Both drivers are controlled by the FPGA system, which allows control of RF power and frequency control. The Crystal Tech 200 MHz AOM was controlled by a fixed frequency VCO, which allows RF power control via the FPGA system.

The characteristics of the AOMs are summarised in table 5.1.

5.1.5 Trap Derived Frequencies

The frequencies required for the two parts of the Raman beams, trapping, molasses, optical pumping, detection and blow-aways are derived from the trap laser. This is done with a series of AOM's, illustrated in figure 5.11.

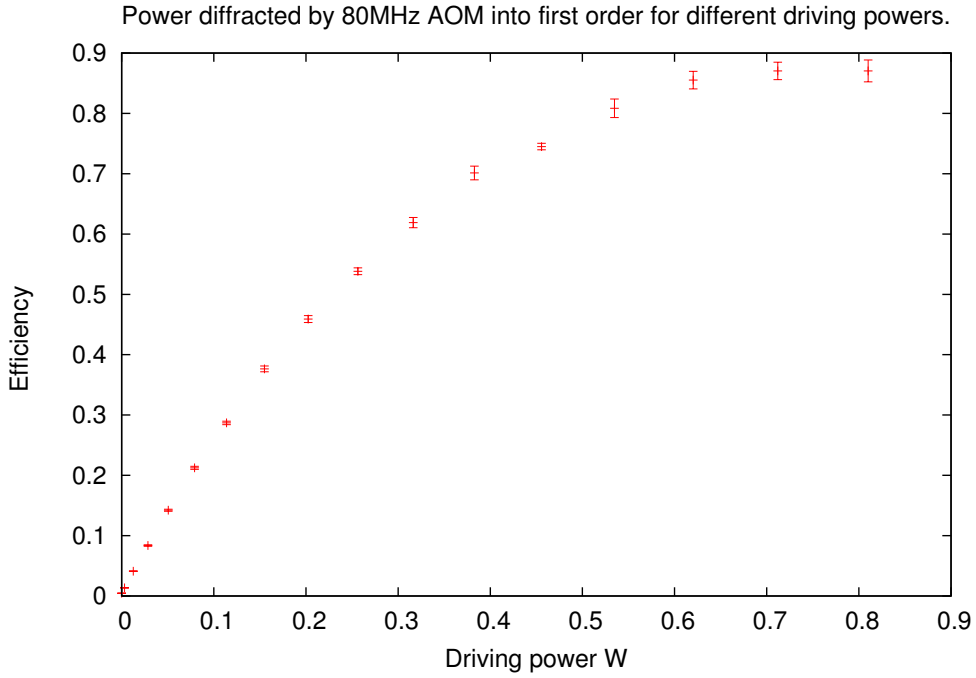

Figure 5.8: Graph of AOM efficiency with RF power for a Gooch & Housego 80 MHz AOM. The data is taken for the same diffraction order as order A in 5.7.

	Gooch & Housego	Crystal Tech	Brimrose
Active aperture (μm)	500	150	76
Bragg angle (°)	0.83	2.0	15.6
Bandwidth (3 dB)	$\pm$ 20 MHz	N/A	200 MHz
Peak efficiency (%)	85	70	30

Table 5.1: Table summarising AOM characteristics.

First the laser is passed through a second optical isolator, and coupled into a fibre, using two lenses to mode match. The second optical isolator is required as reflections from the fibre face destabilised the ECDL with just one optical isolator. The fibre was used to clean the modes of the laser, producing a spherical beam with an $M^2 \approx 1.1$.

To create the trap beam, the beam is focused into AOM0 via a steering mirror and PBS 1. When AOM0 is activated, the beam is double passed through the AOM and then is transmitted through PBS 1. The beam is collimated by a lens and retro-reflection off a mirror and through a quarter wave-plate. The beam then has the same profile as it did before the double pass of AOM0, but an orthogonal polarisation, so that it is reflected off PBS 1 and PBS 2 to form a beam waist in AOM1. When AOM1 is activated the beam is double passed through the AOM and transmitted through PBS 2.

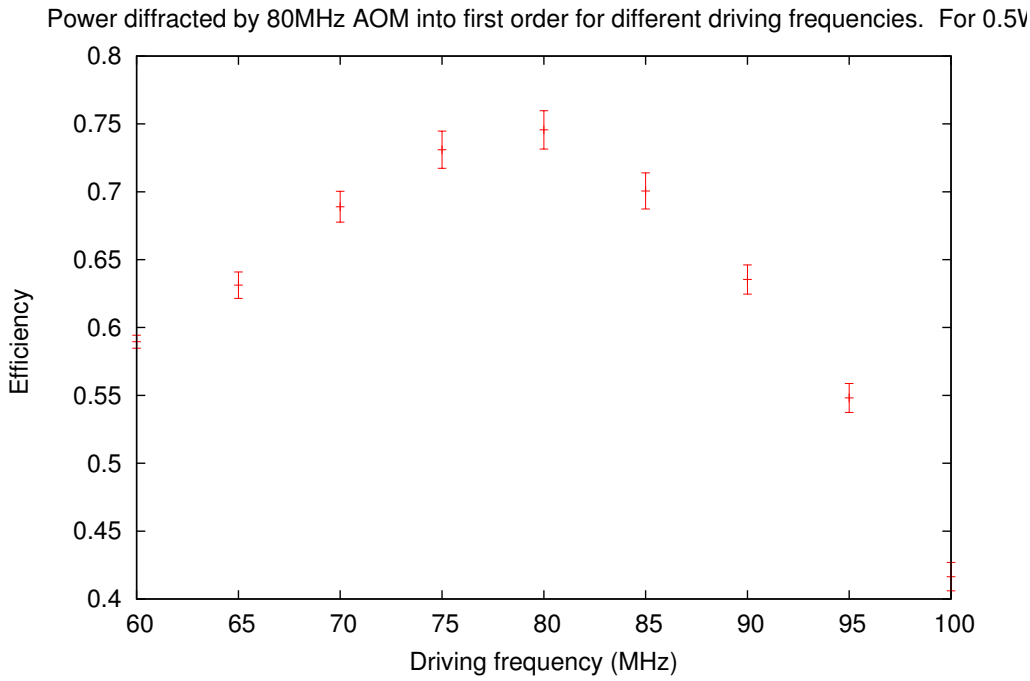

Figure 5.9: Graph of AOM efficiency with frequency for a Gooch & Housego 80 MHz AOM. The data is taken for the same diffraction order as order A in 5.7.

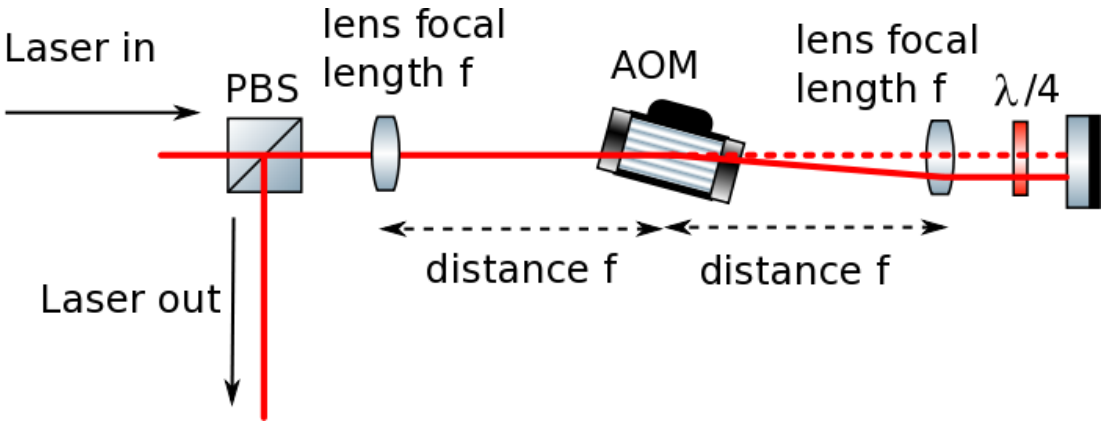

Figure 5.10: Sketch of a typical AOM double pass.

The beam collimated and then refocused to form a beam waist in AOM4. When AOM4 is not activated the beam passes through AOM4 and PBS 3, where it is re-collimated and used as the trap beam. AOM0 provides a nominal down-shift of 160 MHz and AOM1 provides a nominal up-shift of 160 MHz, resulting in no net frequency shift. The trap beam laser intensity may be modulated by these AOMs and the frequency may be adjusted by ± 80 MHz, which is used to create the molasses frequency.

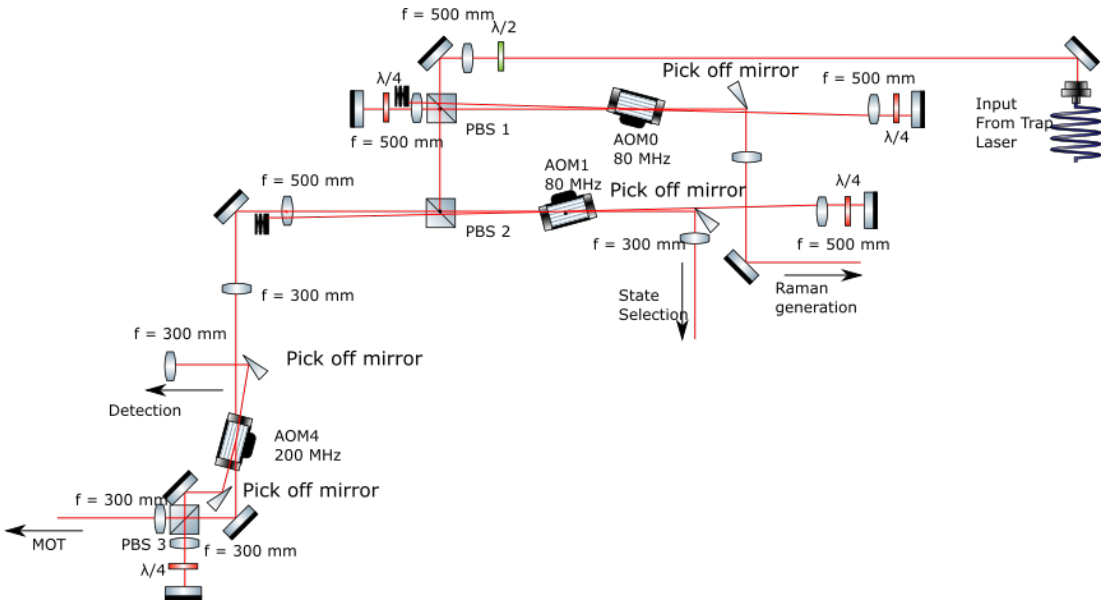

Figure 5.11: Sketch of the AOM frequency generation circuit for the trap derived frequencies.

The detection beam may be created by additionally enabling AOM4, which implements a frequency shift cancelling double pass, in which the first pass is at the Bragg angle down-shifting the beam and the return pass is at the opposite Bragg angle up-shifting the beam. The state selection beam is provided by enabling AOM0, but not AOM1. In this case the beam passes through AOM1 undeflected and a pick off mirror diverts the beam to the state selection system. Driving AOM0 at 85 MHz provides the 170 MHz detuning required for the state selection beam.

When AOM0 is not activated, the beam is picked off and sent to the Raman system. A controllable beam waist, in size and position, is formed by a system of four convex lenses, so the position and size of the beam waist can be optimised for maximum efficiency of AOM3. This is illustrated in figure 5.12. Lens 1 and 2 forms a composite lens, adjusting the separation of the lenses alters the beam waist size and position. Lens 3 is positioned to collimate the beam and lens 4 recreates the same beam waist in the centre of AOM3.

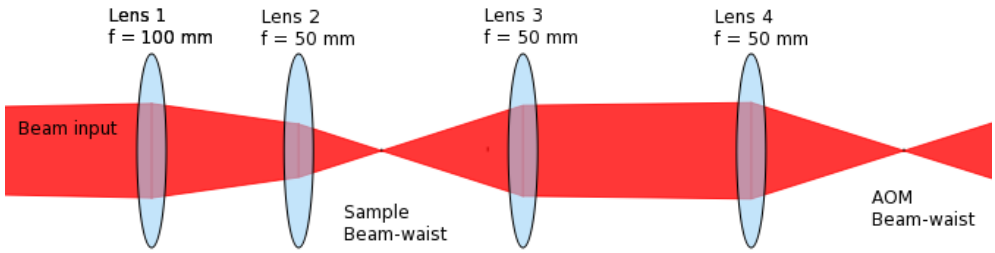

Figure 5.12: Illustration of the lens system that form the beam-waist in AOM3.

When AOM3 is activated, on the first pass part of the beam is diffracted and down-shifted in frequency by 1.5 GHz. See figure 5.13. The remaining beam is retro-reflected off a concave mirror reforming the beam waist in the AOM. This beam is diffracted and up-shifted in frequency by 1.5 GHz. These two diffracted beams are the two components of the Raman beams, which can be seen as R1 and R2 in figure 5.1. These beams are collimated with a 50 mm lens and separately passed through a heated Rb cell to reduce any frequency component resonant with Rb. Additionally the beams are passed through an iris to reduce unwanted reflections. Then the two frequencies are combined on a PBS, and launched into a 10 m fibre. The beam's spatial modes are cleaned by the fibre, and delivers the beam to the experiment. The fibre launch is illustrated in figure 5.14.

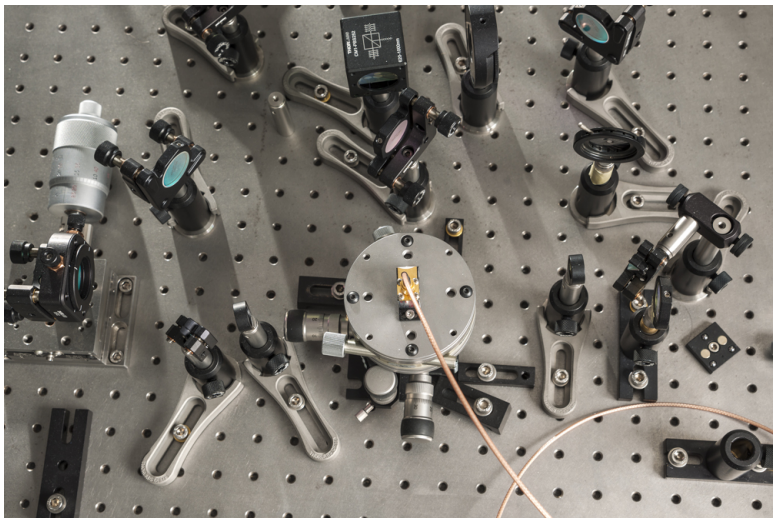

Figure 5.13: Photo of AOM3. AOM3 is on a precision rotation mount like the other AOM's to get the angle, but also a 2-D precision mount to maximise the efficiency of the AOM. This is required because of the small 76 μm active aperture of the AOM. The concave mirror is also on a 1-D precision translation for similar reasons.

The combination on a PBS dictates that the polarisations of the two frequencies must be perpendicular. To stimulate Raman transitions the two frequencies must be either identically circularly polarised and propagating in opposite directions, or orthogonally linearly polarised and the atoms have a non-zero velocity [72]. The constraint of combining on a PBS restricts us to the latter, with the two frequencies being retro-reflected through a quarter wave-plate to form the Raman beam.

The combined Raman frequency beam was analysed with a scanning Fabry-Perot interferometer. The frequency spectrum of the Raman beams was compared to the trap beam to confirm the separation in frequency of the Raman beams. Figure 5.15 shows this spectrum. The two Raman beams can be seen 1.518 GHz either side of the trap frequency. The linewidth of the frequencies is limited by the resolution of the Fabry-Perot, and the true linewidth of the beam is sub 100 kHz, from the ECDL's.

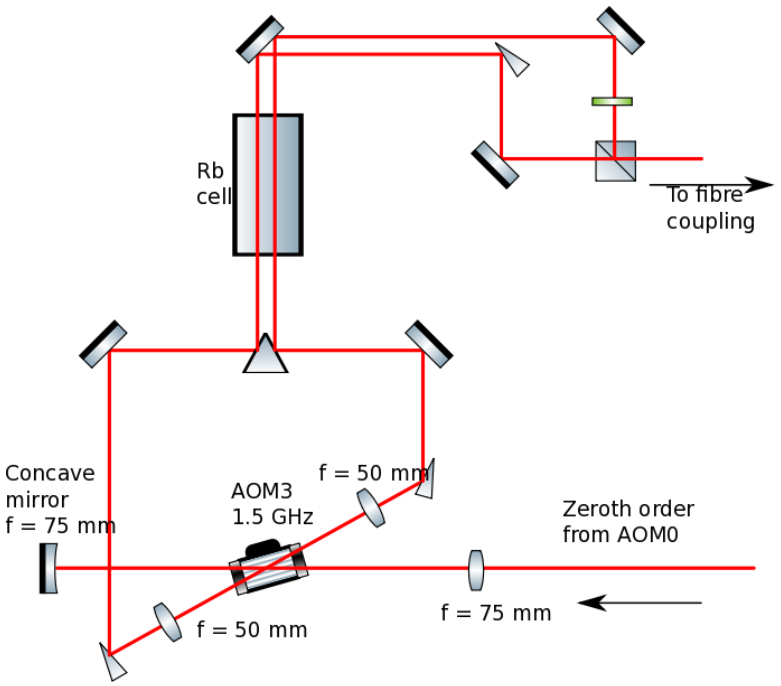

Figure 5.14: A diagram showing how the Raman beams are launched into a fibre.

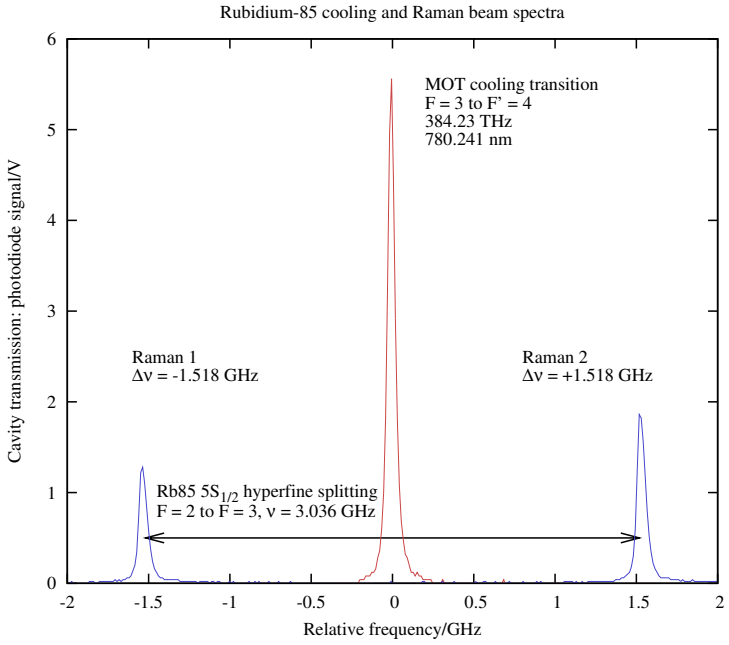

Figure 5.15: Plot of the Raman beams spectra compared with that of the trap beam.

The frequency difference between the Raman beams needs to be chirped at $\frac{df}{dt} \approx \frac{2g}{\lambda} = 25.1 MHz/s$ to maintain resonance with the atoms as they fall. As the AOM frequency is chirped, the angle of deflection alters, and this will change the path length difference of the two beams to the fibre. This change in path-length difference will affect the phase of the Raman pulses. This is expected to be linearly proportional to

angle. The phase shift due to chirping can be measured using a fast photo-diode, and included into the laser phase term in equation 4.4.

5.1.6 Pump Derived Frequencies

The other frequencies are derived from the pump laser and are shown in figure 5.16. The beam is passed in free space from the ECDL to AOM2, an 80 MHz AOM. Passing the laser in free space was deemed acceptable, as the requirements for the beam quality is less for the pump beams applications, and this avoids the inefficiencies associated with fibre coupling. This AOM is set up in a frequency shift cancelling double pass arrangement like AOM4, with the beam waists being formed by a f = 300 mm lens. This allows the pump beam to be turned on and off with the timing of an AOM. To produce the pump beam AOM2 is operated at 80 MHz, and the desired beam unshifted in frequency is picked off. The beam is split by a 50:50 beams-splitter creating the pump beam for both the MOT and detection.

The optical pumping state selection beam requires little power and is split off the first order diffraction by a a 8:92 pelicle beam-splitter when AOM2 is operated at 63 MHz If necessary a blow-away beam from F = 2 can be produced in a similar way, by operating AOM2 at 92 MHz.

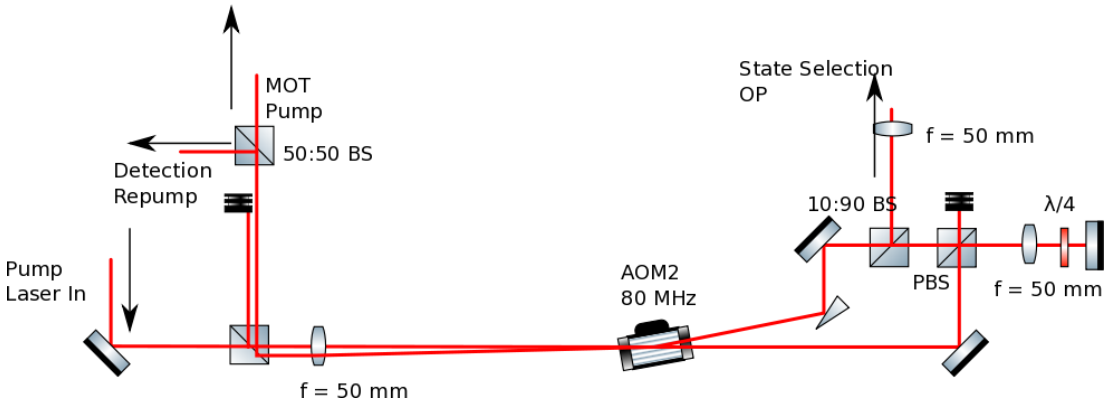

Figure 5.16: Sketch of the AOM frequency generation circuit for the pump derived frequencies.

5.1.7 Summary of Frequency Generation and Laser Power

A photograph of the laser system can be seen in figure 5.17. The trap laser produces 105 mW under normal use. The two optical isolators, fibre coupling, transmission through PBS's and the efficiency of the AOM passes should account for most of the power loss. However further inefficiencies are accumulated particularly on lenses. The pump laser produces 70 mW, which again is reduced to similar inefficiencies to the trap laser.

The logic for each frequency generation is summarised in table 5.2.

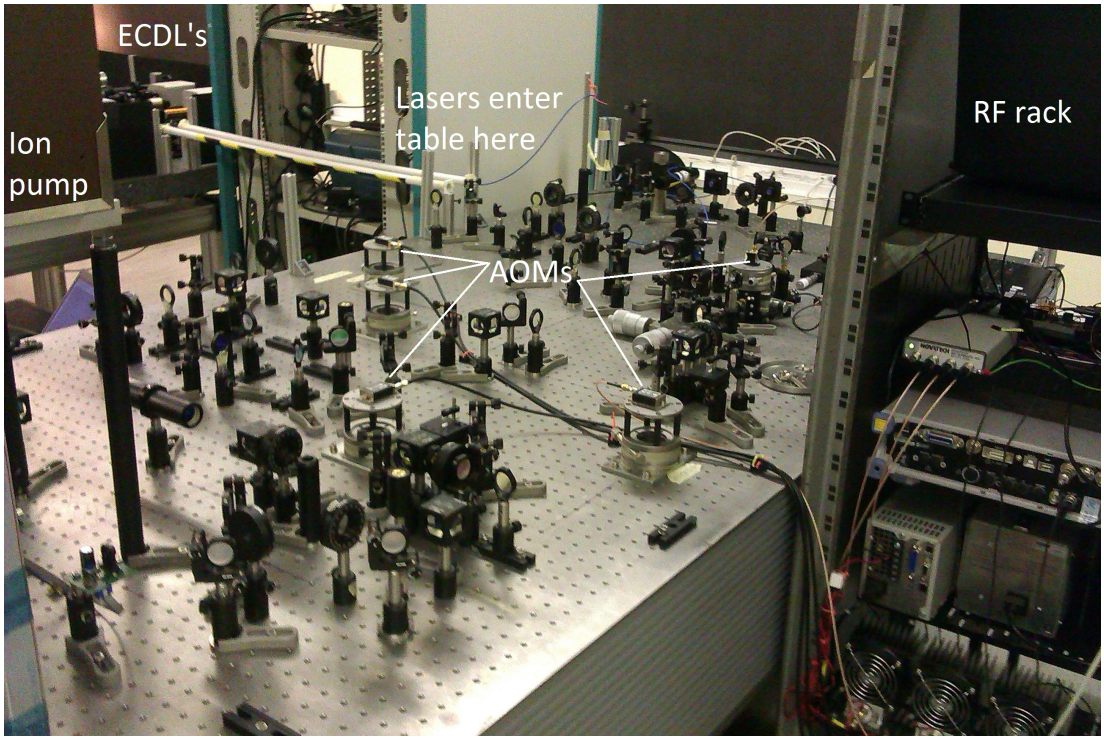

Figure 5.17: Photo of the laser system. All five AOM's can be seen on rotation mounts on the optical table, with the lasers coming in from the laser table towards the back of the picture.

5.2 Timing System

The experiment is controlled by an FPGA board. The use of a FPGA allows the sequence to be preloaded into the RAM of the board and commands are implemented without latency. The board sequences together the RF signal generators, power supplies controlling the magnetic coils and optical shutters.

The AOM's are controlled by driving them with RF signals. All three of the 80 MHz AOM's are driven by a Novatech 409B, which is implemented to drive the AOM's independently at different voltages and frequencies between 60-100 MHz. The voltage can continuously ramped. Similarly the 1.5 GHz AOM is driven by a Rohde & Schwartz SMA 100A. This was implemented to drive the AOM with a chirped frequency, with a specific phase. The shutters and the magnetic field power supplies were controlled by the FPGA via digital to analog converters.

The communication between the FPGA and the hardware was programmed in xml. Sequences could be flexibly programmed by calling on these files.

5.3 Summary

In this chapter, a unique laser system, consisting of two ECDL's and five AOM's, capable of generating all of the required frequencies for the prototype atom interferometer

	AOM0	AOM1	AOM2	AOM3	AOM4
Trap	80 MHz	80 MHz	N/A	Off	N/A
Molasses	Up to 100 MHz	80 MHz	N/A	Off	N/A
HP	87 MHz	Off	N/A	N/A	N/A
Detection / F = 3 Blow-away	80 MHz	85 MHz	N/A	N/A	200 MHz
Raman 1	Off	N/A	1.518 GHz + Chirp	N/A	N/A
Raman 2	Off	N/A	1.518 GHz + Chirp	N/A	N/A
Pump	N/A	N/A	80 MHz	N/A	N/A
OP	N/A	N/A	63 MHz	N/A	N/A
F = 2 Blow-away	N/A	N/A	92 MHz	N/A	N/A

Table 5.2: Summary of the AOM logic, the frequencies they operate at, to produce different beams, and the output power of the laser system.

was presented. The need to view the laser beams using Gaussian optics was presented and the characterisation of an AOM was discussed. The optical circuit and it's corresponding logic was described, detailing how each of the required laser beams required, as described in the previous chapter, is generated.

Chapter 6

Optical Molasses, Temperature Measurements and Releasing Atoms

This chapter describes the work done on the atom interferometer MOT, and the development of the optical molasses cooling and release of the atoms. The apparatus used for this was described in chapter 4 using the laser system from chapter 5.

The quality of the optical molasses is a diagnostic of the MOT alignment [65]. When a cloud of atoms are released from a MOT by switching off the anti-Helmholtz coils, the atom cloud should expand uniformly, with a slower expansion indicating a more optimal molasses. Poor alignment, remaining magnetic fields, incorrect polarisations or a beam intensity imbalance may also cause the atom cloud to move in one direction.

The first step to creating a well aligned MOT is balancing the intensity and polarisation of the counter-propagating laser beams. Two optical power meters were used to balance the beam power by simultaneously measuring the beams and using the half wave-plates to control the splitting at the PBS's. Secondly to correctly set the circular polarisations, a PBS was temporarily inserted and the beams were retro-reflected through the quarter wave-plate. When the quarter wave-plate was creating circularly polarised beam without ellipticity the laser beams, the reflection off the PBS is maximal, as measured by a power meter.

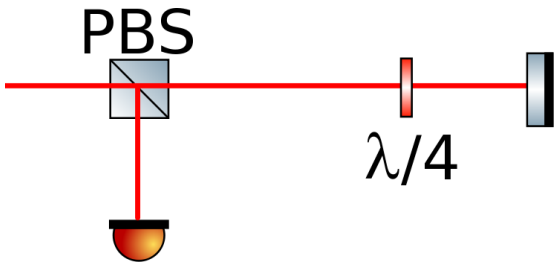

Figure 6.1: Optical circuit for correctly aligning circular polarisations.

To align the beams, plastic discs with a 1 mm hole in the centre were designed to

fit over the vacuum windows. These were used to guide the beams to be geometrically centred on the vacuum chamber within 1 mm. The anti-Helmholtz coils were moved to create a uniform expansion of the cloud. Adjustments were then made to the beam alignment to optimise the cloud expansion. The magnetic coils position and beam alignment were adjusted to first create a uniformly expanding atom cloud by eye, and then to create the longest living molasses. This was measured by analysing video of the MOT expanding, plotting the integrated pixel intensity of each frame over time. A plot of the intensity over time for the optical molasses can be seen in figure 6.2, with three different examples of the molasses as the alignment improved.

As the alignment was further improved the duration of the optical molasses improves from about 100 ms to 300 ms. Figure 6.3 shows frames from the videos used for figure 6.2. The first example of molasses can be seen to decay quickly, no longer visible after 100 ms. Example two lasts much longer, but the atom cloud move in bulk to the top right of the image. The third example improves on this with a more uniform expansion.

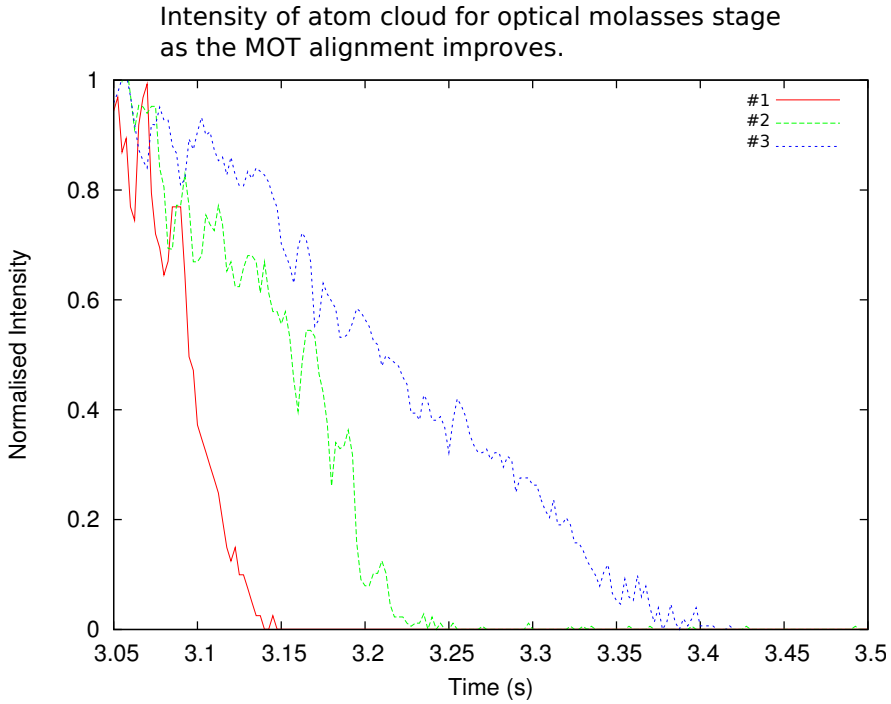

Figure 6.2: Intensity of optical molasses over time, as alignment improved.

6.1 MOT Measurements

With the new MOT apparatus, quantitative measurements were made. The laser system described in section 5 allowed for more measurements to be made, in particular with finer frequency control, and timing control of the laser beams made release/recapture temperature measurements possible.

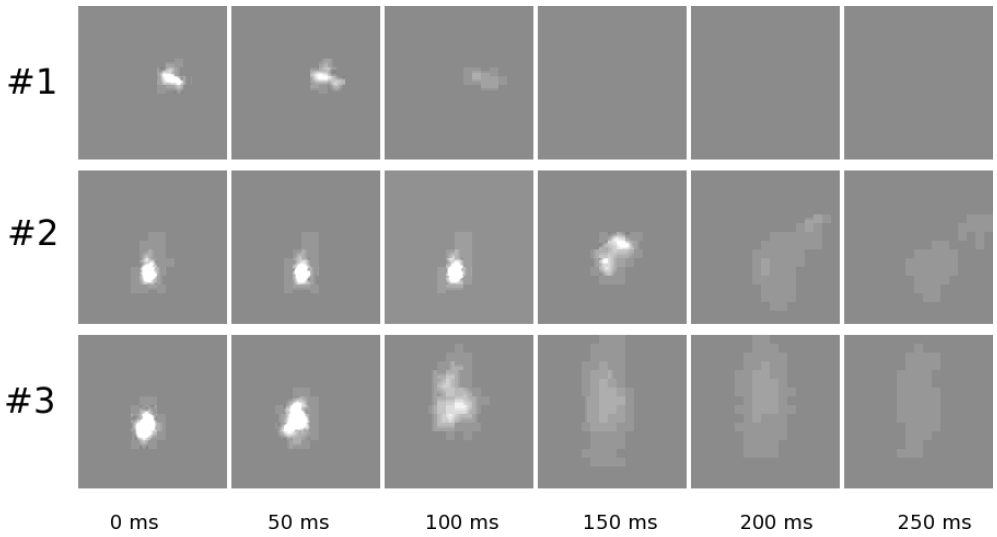

Figure 6.3: Frames for the videos of the optical molasses corresponding to those in figure 6.2. Each frame is 5.6 mm square.

6.1.1 Atom Number

The number of atoms was measured for the MOT, with characterisation plots made for trap and pump beam intensities, trap beam detuning and magnetic field gradient. The first step was to produce a power calibration plot of the camera, as seen in figure 6.4. It is fit with a quadratic, $f(x) = Ax^2 + Bx + C$, with A $= -5.74 \times 10^{-10}$, $B = 0.000154$ and $C = -0.290$

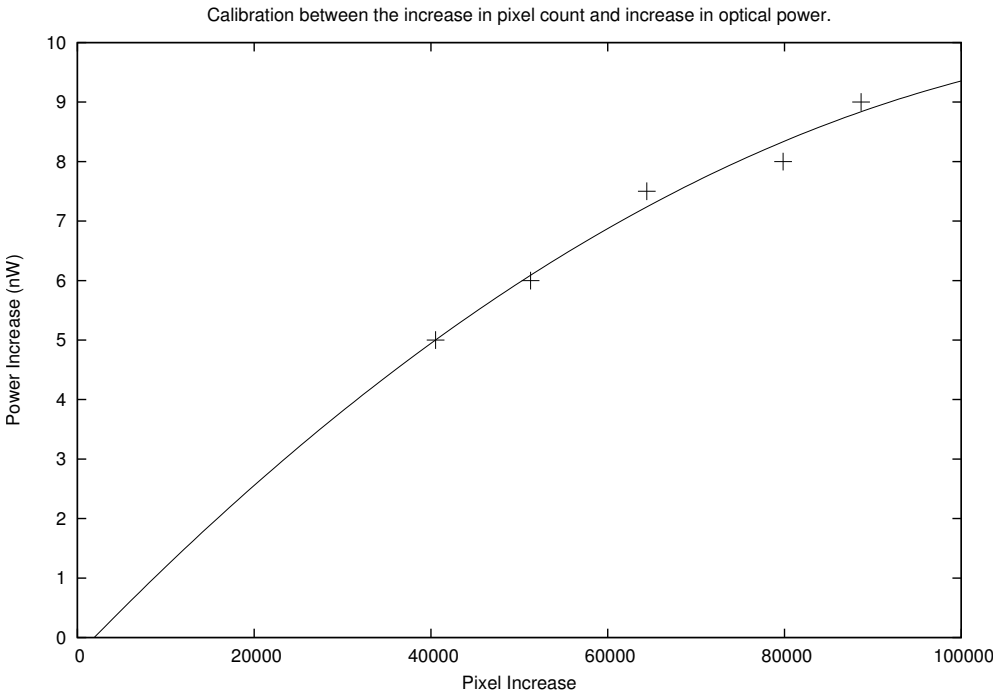

Figure 6.4: Calibration plot between pixel increase and power increase of a power meter mounted adjacent to the MOT chamber.

For these measurements, the standard magnetic field gradient was 16.3 G/cm with an estimated accuracy of $\pm 0.2\ G/cm$ from the initial measurement of the coils gradient. The trap laser was locked with a detuning of $10.8 \pm 0.4\ MHz$, which was determined from an oscilloscope readout of the locking point. The power in each beam was measured at 0.96 mW per beam, giving a total maximum intensity of $27 \pm 1.7\ I_{sat}$. The pump beam was typically used on maximal power.

The number of atoms increases with magnetic field gradient, as in the first MOT set up, although the gradient seems to have started to flatten. This can be seen in figure 6.5.

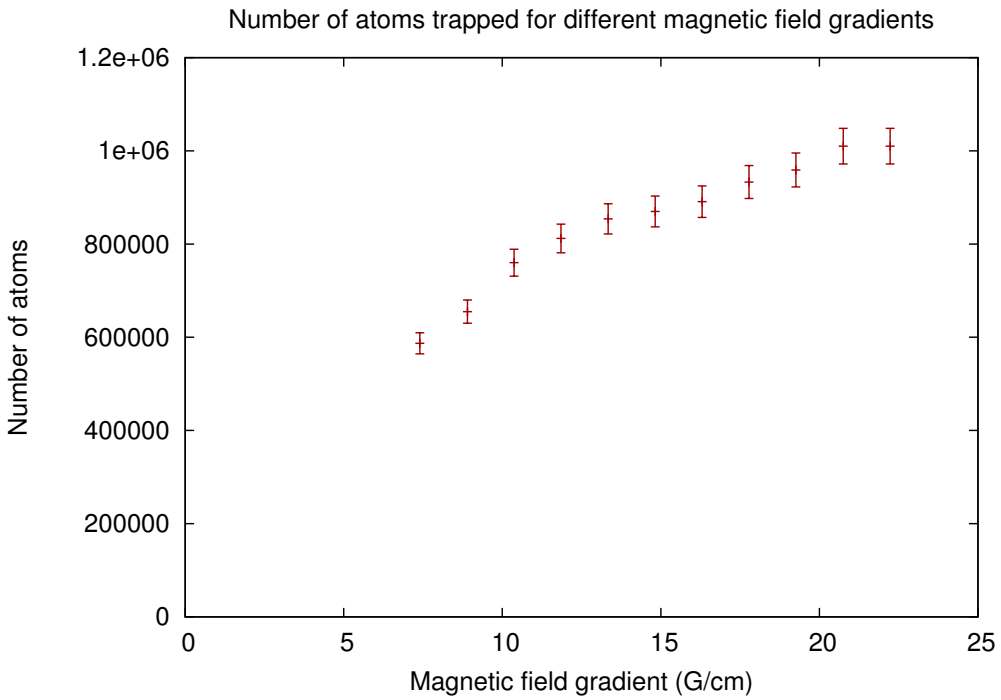

Figure 6.5: Plot of number of atoms trapped vs magnetic field gradient.

Figure 6.6 shows a slightly larger detuning of 12.8 MHz would be preferential for trapping more atoms in this configuration. The number of atoms increases with trap beam intensity, which can be seen in figure 6.7. The pump intensity could be decreased to 40 % of the maximum power without affecting the number of trapped atoms, as seen in figure 6.8.

6.1.2 Release and Recapture Temperature Method

Temperature measurements were made using the release recapture method [80]. These measurements required the ability to turn the lasers on and off at the millisecond level, made possible by the laser system described in chapter 5.

The MOT was observed with a CMOS camera focused on a 2 mm square region of interest with the MOT in the centre. The pixel values for each frame were summed

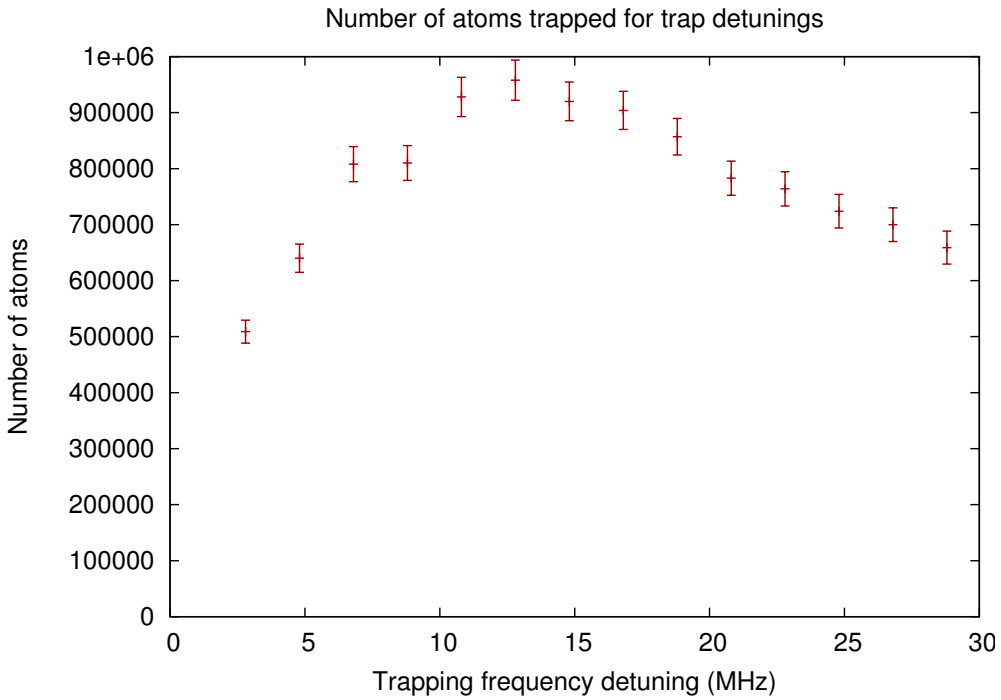

Figure 6.6: Plot of number of atoms trapped vs detuning frequency.

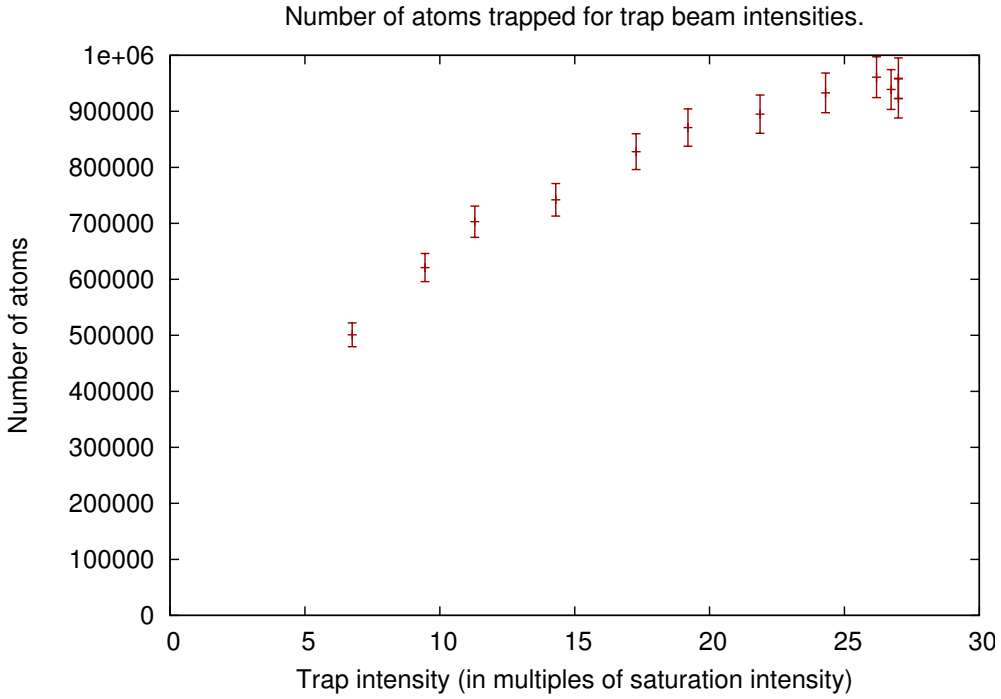

Figure 6.7: Plot of number of atoms trapped vs total trap beam intensity.

as they were in the atom number measurements, to give an intensity value for each frame of the video. The lasers are turned off at $t = 0$, the atoms thermally expand, and are observed by turning the pump and trap beams back on. This was observed by recording a video of the atoms at 400 fps. The fraction of atoms remaining in the

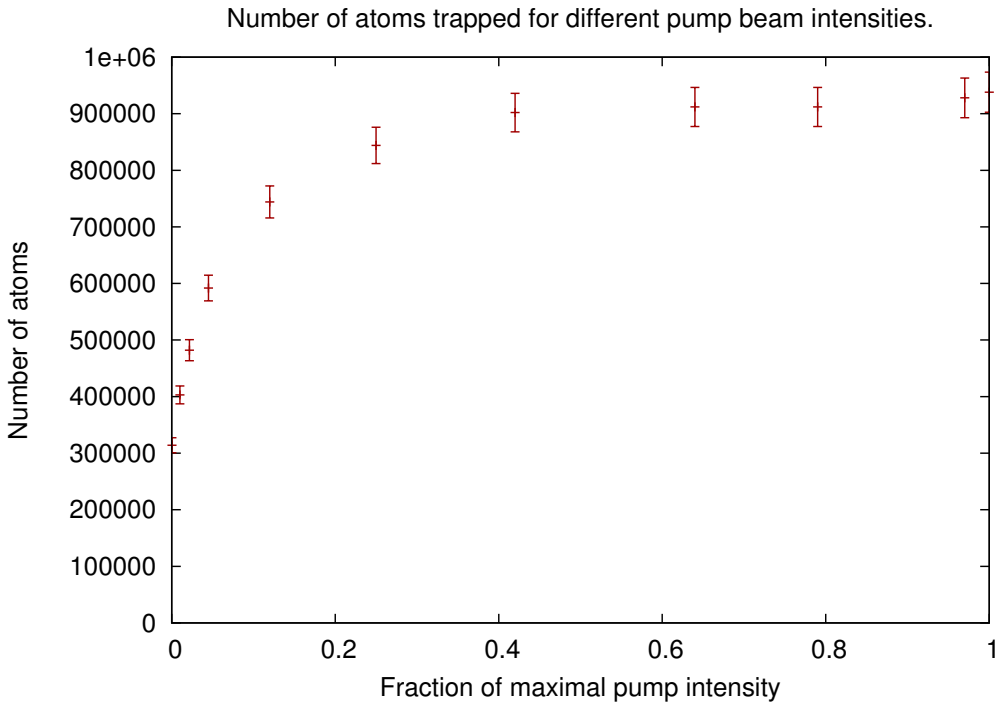

Figure 6.8: Plot of number of atoms trapped vs pump beam intensity as a fraction of the maximal value.

observed region was measured for different times of thermal expansion.

The density distribution of the atom cloud as observed by a camera can be modelled as a Gaussian in the horizontal component x and vertical component y, and has a width $\sigma(t)$ which is a function of time. The normalised density is

$$\rho(x,y,t) = \frac{1}{2\pi\sigma^2(t)} exp[\frac{-\left(x^2+y^2(t)\right)}{2\sigma^2(t)}] \tag{6.1}$$

where x is the radial position of the cloud and t is time. The cloud will fall under gravity so $y(t) = y + \frac{1}{2}gt^2$, where (x, y) is the position of the cloud at time $t = 0$ and g is the gravitational acceleration. The cloud width expands thermally depending on the temperature T, $\sigma(t) = \sqrt{(\sigma_0^2 + \frac{2k_BT}{m}t^2)}$. The parameter σ_0 is the clouds width at $t = 0$, k_B is the Boltzmann constant and m is the atomic mass of ^{85}Rb.

The fraction of atoms left in an area viewed by the camera at time t is given by

$$f(t) = \int \rho(x,y,t)dxdy = \int_{-L}^{L} dx \int_{-L}^{L} dy\rho(x,y,t), \tag{6.2}$$

where the area of integration is a square field of view, centred on the atom cloud at time t=0, side length $2L$. This can be written

$$f(t) = 2\int_0^L dx(\int_0^L dy - \int_0^{-L} dy)\rho(x,y,t)$$
$$= \frac{1}{2}erf(\frac{L+}{\sqrt{2}\sigma(t)})\left(erf(\frac{L+\frac{1}{2}gt^2}{\sqrt{2}\sigma(t)}) - erf(\frac{-L+\frac{1}{2}gt^2}{\sqrt{2}\sigma(t)})\right), \tag{6.3}$$

where erf is the error function. Observing the proportion of atoms left in the frame after time t, the fractions of atoms as a function of t can be plotted and fitted to obtain the cloud temperature.

An example of turning off the lasers for time 10 ms and observing the recapture can be seen in figure 6.9. The point before observing a large drop in intensity was taken to be the initial number of atoms. The recaptured atoms were probed by a 5 ms laser pulse; the second frame of the pulse was taken as the recapture intensity because the video and the script controlling the lasers were not synchronised, so the first point may not have a full exposure of the recaptured atoms. These two values were compared to the background fluorescence rate, also marked on the graph. The error on the initial number of atoms was taken to be the standard deviation of the 10 previous points before the release of the MOT, which was also assumed to be the error on the atoms recaptured. The background fluorescence error was taken from the standard deviation of a 25 ms laser pulse at the end of the sequence.

The initial size of the atom cloud was taken from the image of the atom cloud before the lasers were turned off. The rows in the image were integrated and fitted with a Gaussian plus a linear function as background to obtain the input value of the fit. An example fit can be seen in figure 6.10.

The data points were taken and fit with the function in equation 6.3. An example fit can be seen in figure 6.11.

6.1.3 Temperature Measurements

From the plot in figure 6.12, no evidence the magnetic field gradient effecting the MOT temperature can be concluded. The relationship between frequency and temperature in figure 6.13 shows a decrease in temperature with an increase in the trap beam detuning. This relationship follows equation 4.1 in that high detunings reach a lower equilibrium temperature from polarisation gradient cooling.

Figure 6.14 show the MOT temperature shows a linear relationship with trap beam intensity. This shows that a colder MOT is achieved at lower intensity, at the price of lower atom number. As the pump intensity is high, it is shown to have little effect on MOT temperature, as shown in figure 6.14

Therefore magnetic field gradient, trap intensity and detuning all have to be optimised for optimal atom number and cloud temperature.

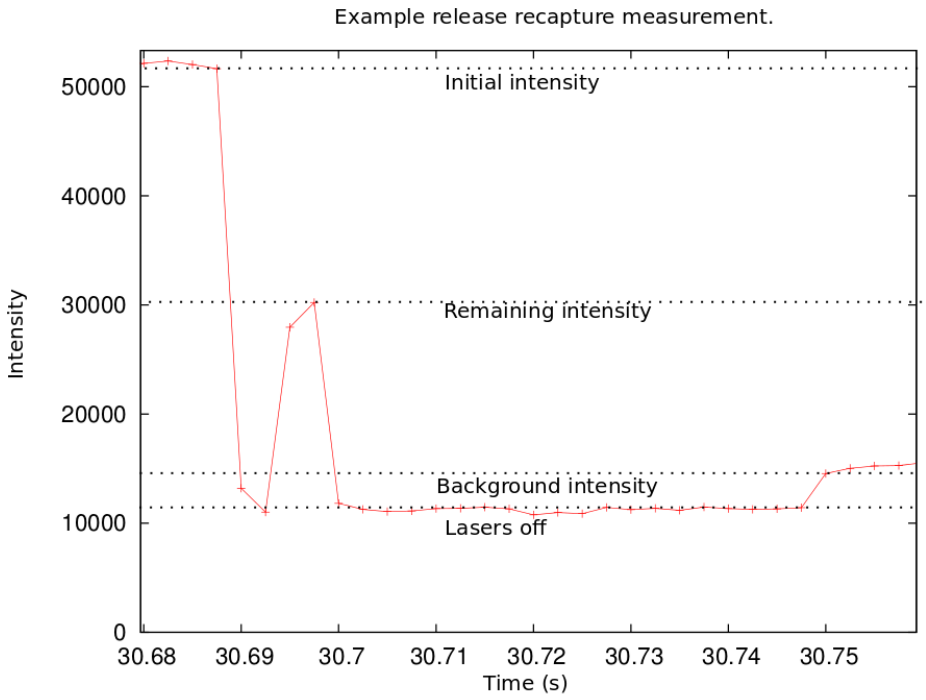

Figure 6.9: An example of a release recapture measurement. Each point represents the integrated pixel values in a video frame taken at 400 fps.

Increasing the magnetic field gradient would increase the number of atoms, at a slight cost in temperature. There is a 23% increase in atom number from operating the MOT at 22.2 G/cm instead of the standard 16.3 G/cm. However a continuous current safety limit of 10 A was placed on the coils restricting them to 16.3 G/cm.

A more significant decrease in temperature would be found by decreasing the intensity of the trap beam, which could lower the temperature from 231 μK to 102 μK in the extreme case. This would decrease this number of atoms by 52%.

Increasing the detuning to the extreme would further cool the atoms by approximately 50 μK from the standard settings, reducing the number of atoms by 71%. The pump laser intensity needs to be kept above 40% of the initial value to maintain high atom number. Given that the MOT is followed by an optical molasses stage to further cool the atoms, the settings will be set to maximise atom number.

6.1.4 Optical Molasses and Releasing atoms

The release of the atoms from the MOT into free fall is accompanied an optical molasses stage. This is standard procedure in atom interferometry, with the steps being broadly the same across different apparatus [25] [72] [46]. With a fully filled MOT, the anti-Helmholtz coils are turned off. This rapid change in magnetic field stimulates eddy currents in the vacuum chamber, which must decay before the next step. This depends

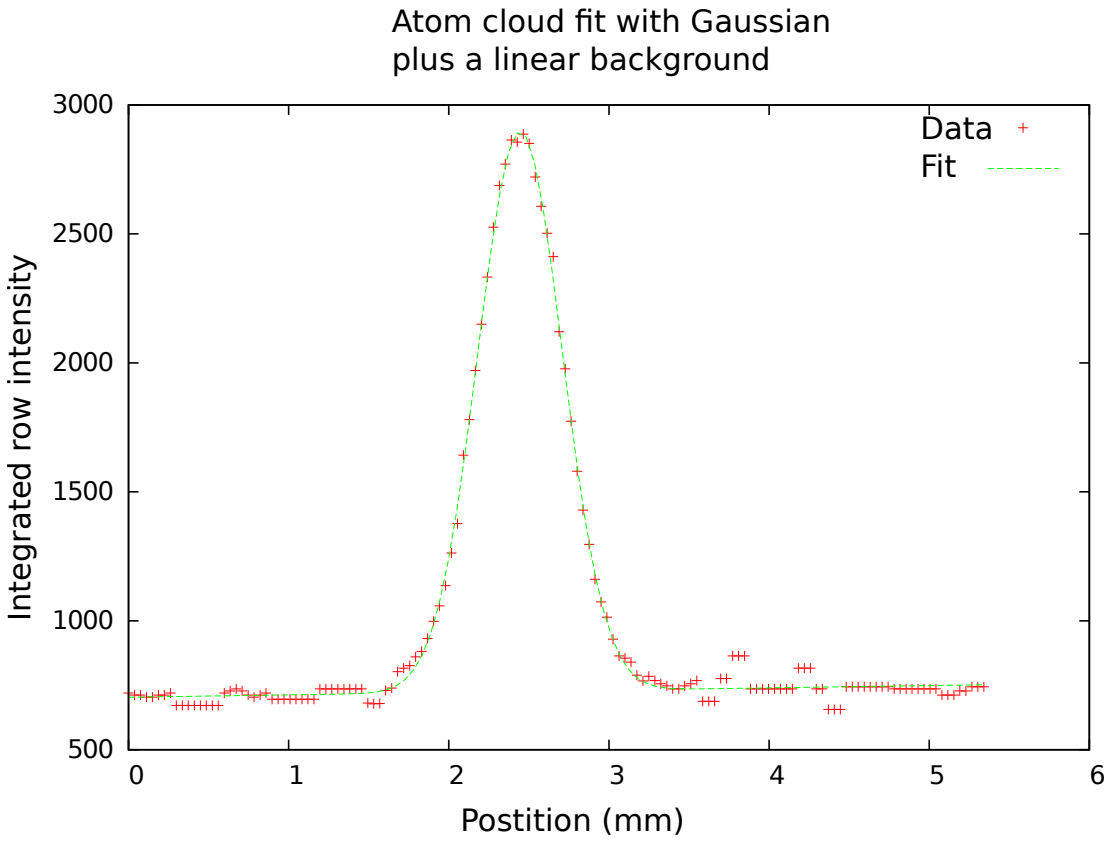

Figure 6.10: The initial atom cloud size was found by fitting an image of the MOT before each release. The cloud was fit with a Gaussian plus a linear function to account for background. For this fit $\sigma_0 = 0.26\ mm$.

on the the amount and the type of material the vacuum chamber is constructed from, and is of order ten milliseconds. This length of time given for the eddy currents to decay is defined as Δt_{eddy}. Next the detuning is increased, to increase the effect of polarisation gradient cooling. The magnitude of the detuning for ^{85}Rb is limited to less than 60 MHz to not excite transitions to the $5^2P_{\frac{3}{2}}F = 3$ state, which decays to the $5^2S_{\frac{1}{2}}F = 2$ by a dipole transition. Atoms in this state would not be cooled. This increase in the detuning frequency is defined as Δf_{det}

This detuned optical molasses is allowed to cool the atoms on order of one millisecond. This length of time is defined as Δt_{cool}. The trap beam intensity must be ramped down to zero, on the order of a millisecond, in time Δt_{ramp}. The pump beam is left on for some time of order a millisecond pump all atoms into the $5^2S_{\frac{1}{2}}F = 3$ state. This length of time is defined as Δt_{pump}.

Optical molasses with differing detunings were investigated. When the detuning is increased there is a large drop in fluorescence intensity. These drops in intensity were used to sync the measurements for comparison. The anti-Helmholtz coils were turned off and after a 20 ms delay the detuning of the trap laser beam was increased. Figure 6.16 shows the intensity of molasses for different sizes of detuning. Increasing

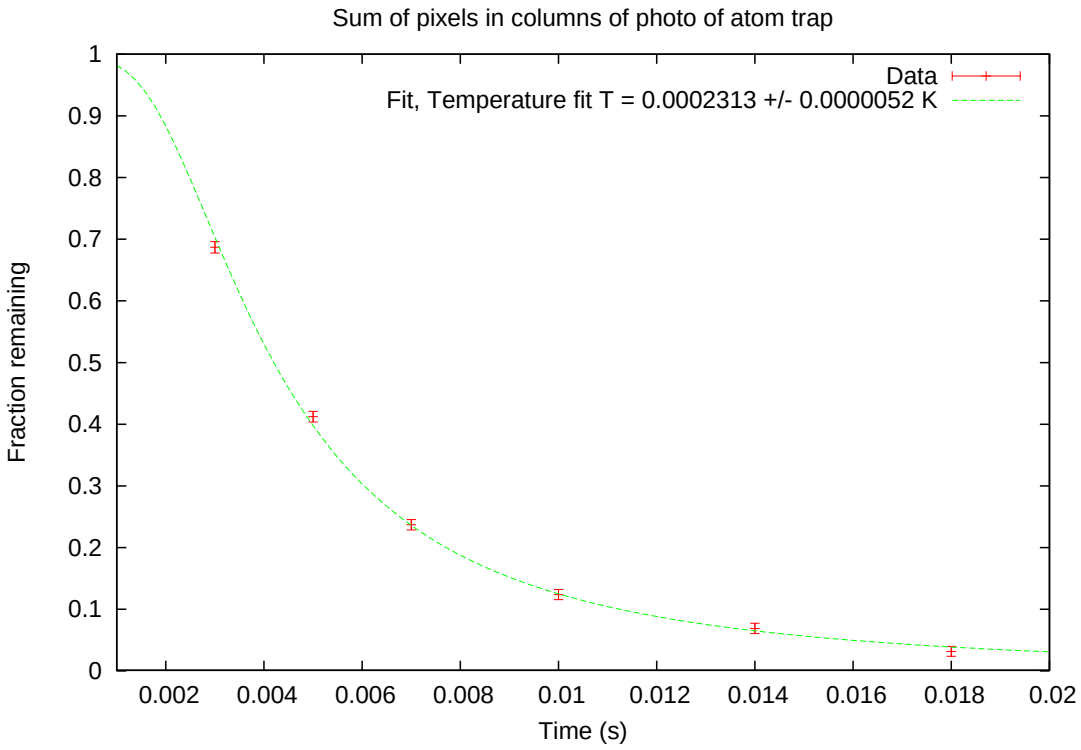

Figure 6.11: Graph of temperature measurement using the release recapture technique.

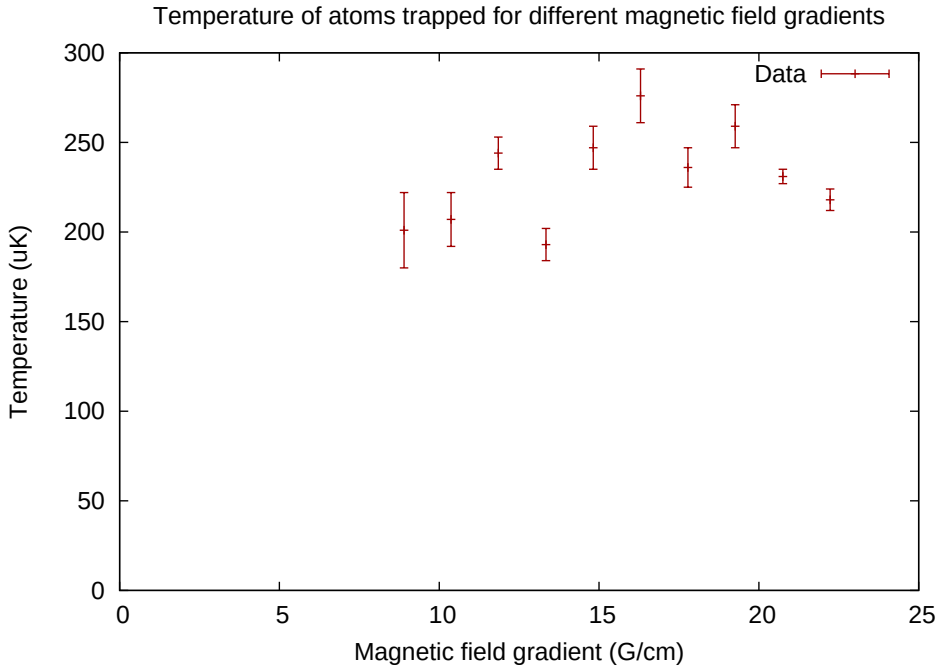

Figure 6.12: Plot of temperature of atoms trapped vs magnetic field gradient.

the detuning creates a longer lived molasses. The fluorescence intensity became too dim to measure for detuning greater than 25 MHz.

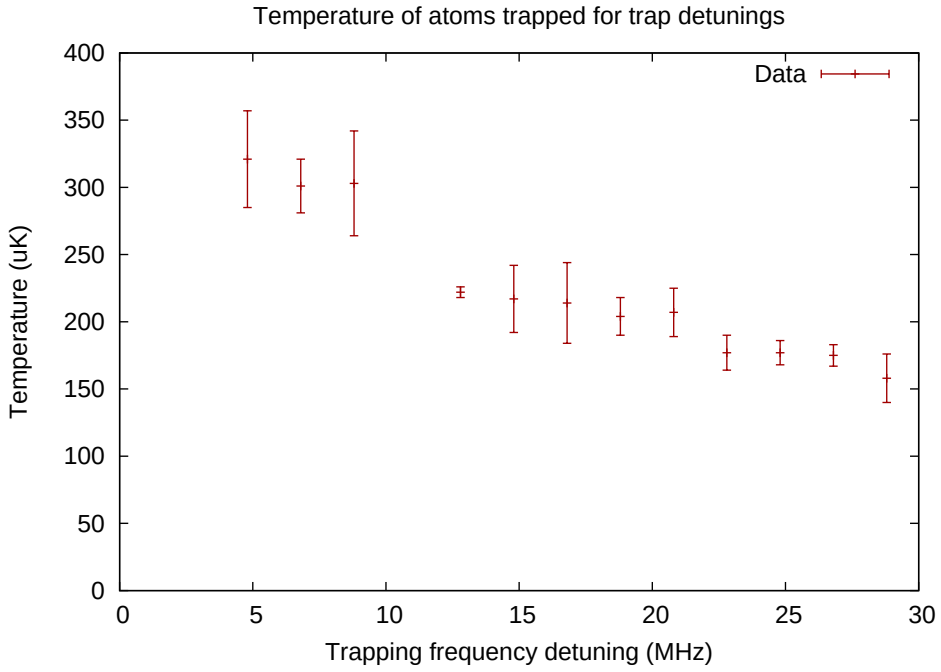

Figure 6.13: Plot of temperature of atoms trapped vs detuning frequency.

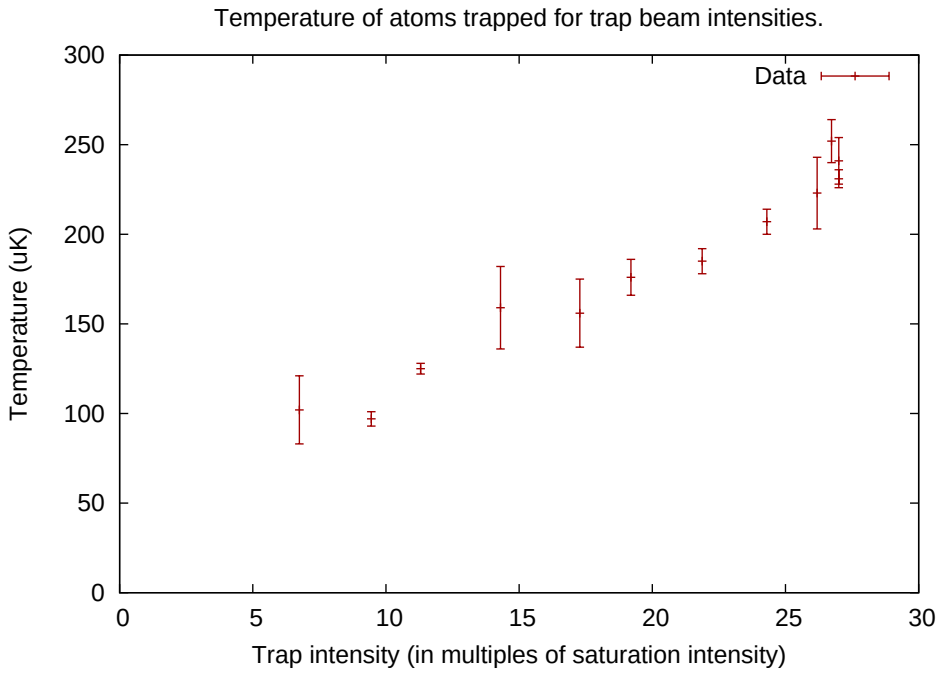

Figure 6.14: Plot of temperature trapped vs total trap beam intensity.

Different Δt_{eddy} times were tested. These can be seen in figure 6.17. For $\Delta t_{eddy} = 10, 20\ ms$ the molasses decay are the same. Waiting 40 ms however does have a negative effect, as the molasses decays quicker.

The effect of different Δt_{ramp} was investigated, with $\Delta t_{eddy} = 10ms$, $\Delta f_{det} = 20$

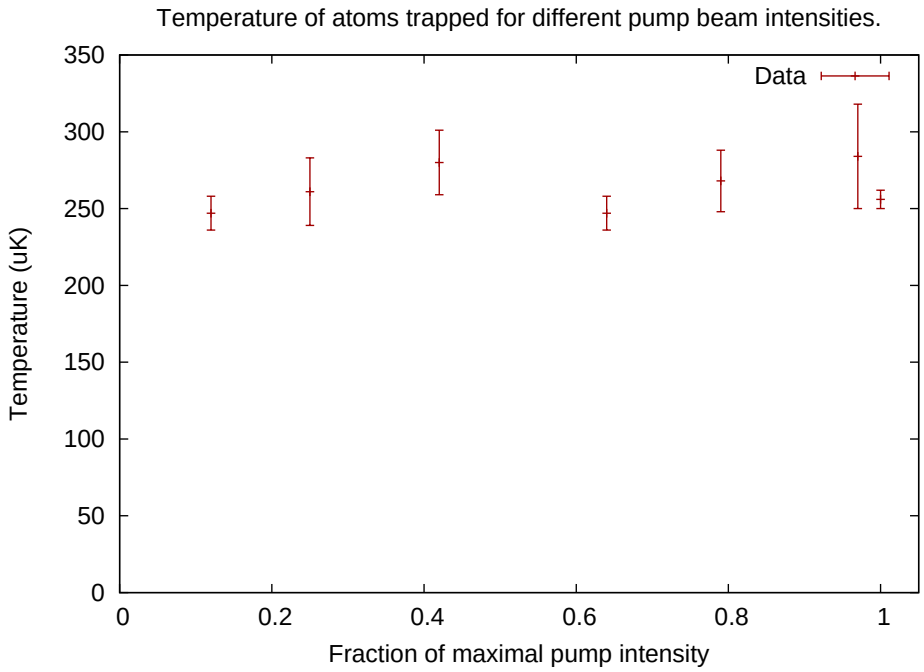

Figure 6.15: Plot of temperature trapped vs pump beam intensity as a fraction of the maximal value.

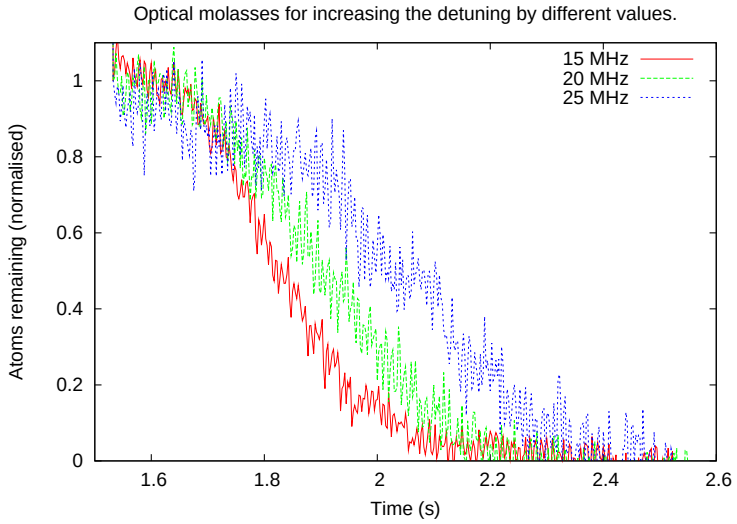

Figure 6.16: Normalised intensity plot for different detunings.

MHz, $\Delta t_{cool} = 2\ ms$ and $\Delta t_{cool} = 1\ ms$. The trap beam was ramped down in intensity using AOM1. The trap beam was turned back on 10 ms later to observe the remaining atoms. This time was chosen so approximately half the atoms remained. The frequency of the trap beam was reset to the MOT detuning so a direct comparison could be made. Figure 6.18 is an intensity plot for different ramping times. There is a slight increase in the fraction of atoms recaptured with longer ramp times.

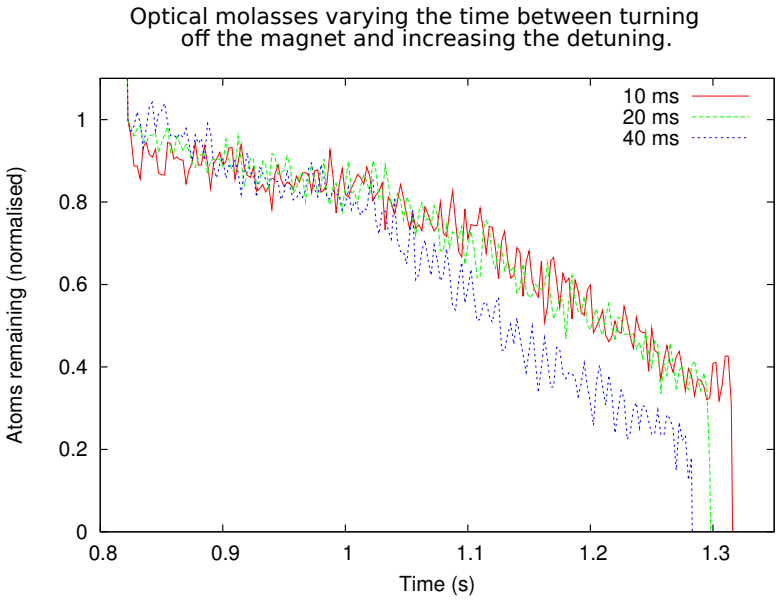

Figure 6.17: Normalised intensity plot for different Δt_{eddy}.

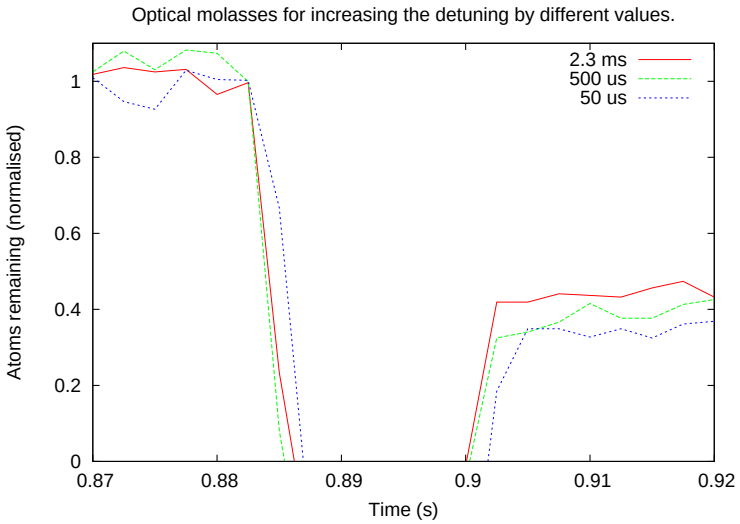

Figure 6.18: Normalised intensity plot for different Δt_{Ramp}.

6.1.5 Molasses Temperature Measurement

The temperature of the atom cloud after a molasses is released was measured. The time differences were taken from when the trap beam is extinguished at the end of the ramp, after this point the atoms are no longer under any laser forces and are in free fall. At this stage, due to the atoms not being fluoresced, the size of the cloud could not be measured. To account for this the cloud size was used as a second fitting parameter, using the size before the molasses sequence as an input value. The trap beam was initially detuned 10.8 MHz at full intensity. The magnetic field gradient was 16.3 G/cm.

Δt_{eddy}	5 ms
Δf_{det}	20 MHz
Δt_{cool}	2 ms
Δt_{ramp}	2.3 ms
Δt_{pump}	1 ms

Table 6.1: Molasses sequence settings for the temperature measurement

The resulting temperature measurement can be seen in figure 6.19. The fit gives a temperature of 96 ± 5 μK. At this temperature the atoms have an RMS velocity of 9.6 cms^{-1}. These techniques have been used to produce temperatures of 30 μK with ^{85}Rb [46].

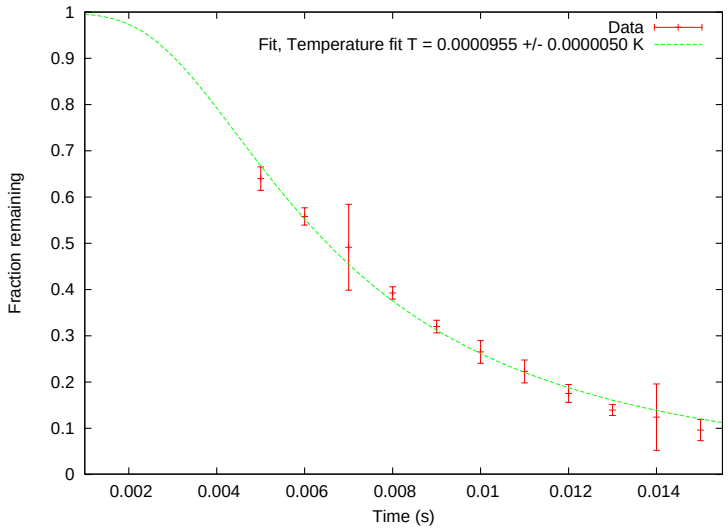

Figure 6.19: Temperature measurements of the atom cloud after the molasses release sequence.

When observing a well aligned molasses for a long time, the atom cloud appeared to be experiencing a torque causing the cloud to spiral, and not expand uniformly. This can be seen in figure 6.20. By frame 6, the atom cloud can be seen to have entered a spiral.

This was attributed to the MOT beams not being spatially uniform. The beam was found to suffer from astigmatism, which can be seen in figure 6.21. The beam divergence is 2.25 times more in the y-axis than the x-axis. As the beams propagate to the trap, the laser will diverge, and the beam intensities in the MOT will not be balanced.

Whilst beam intensities may be balanced at the MOT trapping location, as the cloud expands the ratio of counter-propagating beam intensities becomes unbalanced, due to the spatial inhomogeneities in the beam intensity.

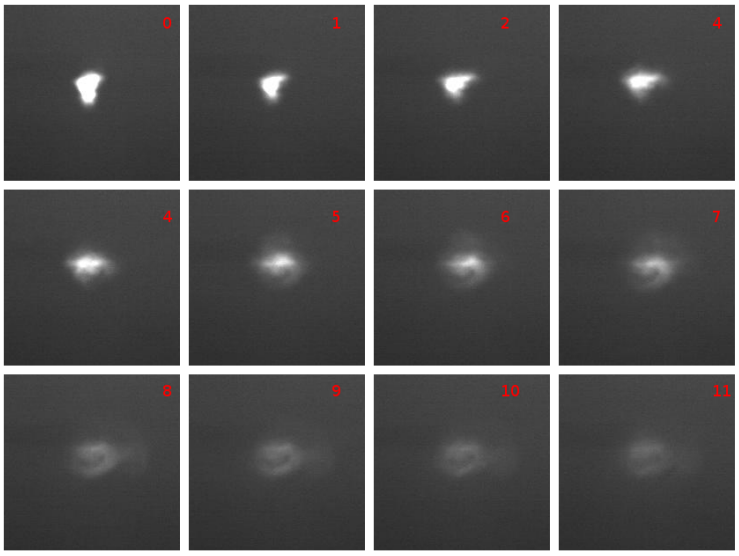

Figure 6.20: Stills of the optical molasses. Image marked 0 is the MOT, and each image after is 50 ms after.

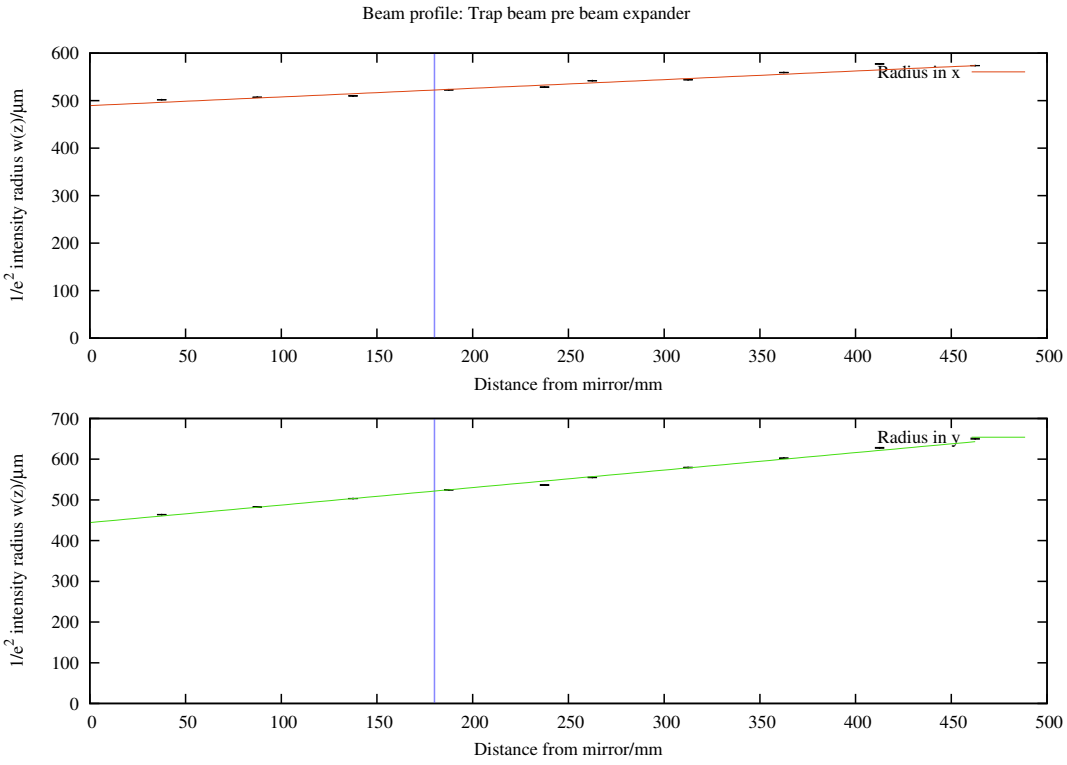

Figure 6.21: Beam profile of the trap laser before the beam expander, demonstrating it's astigmatism. The beam is diverging with an angle of 180 $mrad$ in the x-axis and 406 $mrad$ in the y-axis. The vertical line marks the point at which the beam is equal radius in the x and y-axes.

6.2 Current Status

At this stage, modifications to the MOT circuit were made. The trap beam is mode cleaned through an optical fibre, producing a Gaussian beam. The efficiency of the

fibre coupling is 70%, reducing the trapping power to 670 mW per beam. Initially a 4 mm collimator was used to create a similar MOT as before.

Two additional cameras were introduced to observe the MOT chamber to aid alignment. One was placed on the above the horizontal beam axis (camera 2), and another was displaced horizontally to the side (camera 3), as to observe the trap region. With these and the initial camera (camera 1), which observed the MOT through the free smaller window of the spherical octagon, the fluorescence created by the beams was used to align the beams. The positions of these three cameras are illustrated in figure 6.22.

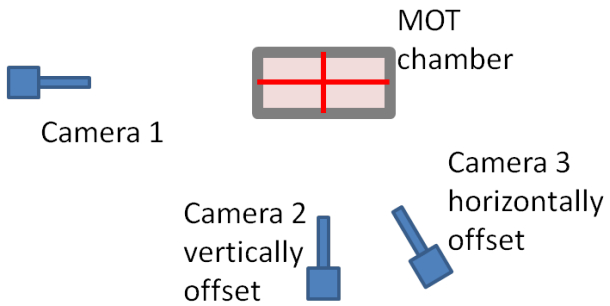

Figure 6.22: Sketch illustrating the position of the three cameras.

To align the beams, images of the beam fluorescing the background vapour are taken. The beam width was fit in the central trapping region, with a Gaussian plus a linear background, for the columns of the image. The central position of these Gaussians were used to fit a linear function to the beam, which was used to describe it's vector. From an initial alignment of the beams using the plastic discs, the beams vectors were determined and used to geometrically align them. Initially one of each beam pair was aligned using these beam vectors, and the remain three beams were brought into to match their vectors. From the fits to the images, it was estimated that the beams could be placed with an accuracy of 10 μm in position and 10 $mrad$ in angle

6.2.1 Optical Amplification with a Tapered Amplifier

Another upgrade to improve the prototype interferometer is the introduction of a tapered amplifier (TA). TA's amplify the input laser beam to powers that surpasses that of normal laser diodes and outputs a beam with the same spectral properties. The tapered amplifier is seeded by a laser beam input through a facet of order 5 μm to ensure single mode behaviour [81]. As the beam passes through the gain medium of the diode, it tapers towards the output facet of about 200 μm to reduce the intensity as not to damage the facet [82]. With an input beam of 10 mW, an output beam of up to 2 W can be produced.

A TPA780P20 TA was purchased from Thorlabs, with associated LDC2500B TA

controller. The TA controller maintains the temperature of the TA through peltier coolers and delivers the driving current for the TA. The TA input is fibre coupled which eases alignment. The trap laser was coupled into a fibre after the locking circuit, and used as the input beam for the TA.

The output of the TA is elliptical due to the cubic shape of the diode facet. The beam is focused in y with a cylindrical mirror, and then a spherical mirror focuses the beam in both x and y. An optical isolator prevents reflections back into the TA.

Further optics shape the the beam for fibre coupling, where it is taken to the experimental table. This circuit is illustrated in figure 6.23, and a photograph of it can be seen in figure 6.24. The camera in the photo is temporarily in place to implement beam profiling for efficient fibre coupling.

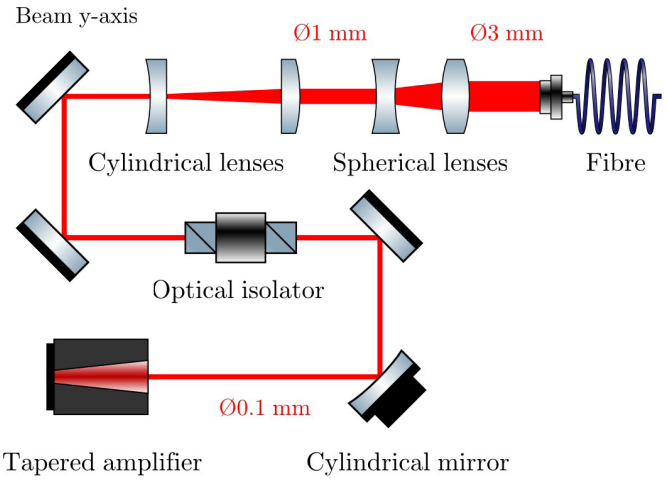

Figure 6.23: Sketch of the optical circuit for the tapered amplifier.

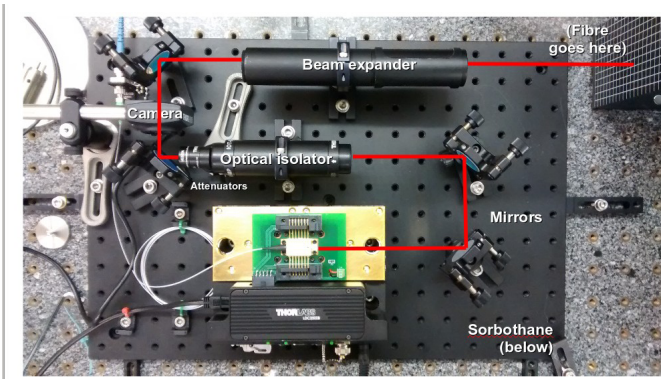

Figure 6.24: Photo of the optical circuit for the tapered amplifier.

The optical power output as a function of current can be seen in figure 6.25. An output power of 1.1 W is delivered by the TA for a driving current of 1.8 A. This is for an seeding power of 5.2 mW.

The TA beam passes through an optical isolator, and is coupled into a single mode

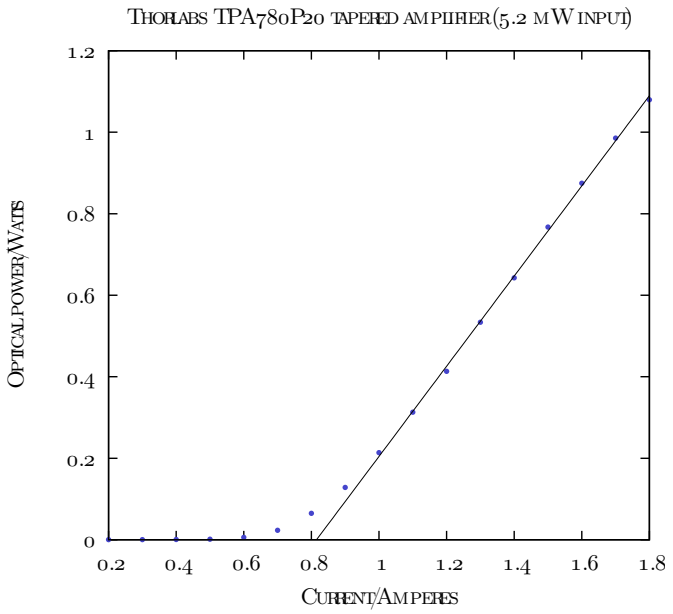

Figure 6.25: Graph of TA optical power as the driving current is varied, for a seeding power of 5.2 mW.

fibre to be taken to the experimental table. Figure 6.26 is the power fibre delivered onto the optical table as a function of current. The graph is not linear and the TA output beam changes shape as the current is varied, with the major axis of the ellipse reducing at higher currents. Therefore the fibre coupling can only be optimal at one current for ideal mode matching (optimised for 1.5 W here).

Currently the TA provides a trap beam with 300 mW of usable power on the experimental table. With the spatial mode output of the TA a function of both the seed power and the driving current, improvements in this power output likely can be made.

With the increased power available, the fibre collimator used to launch the MOT beam has been increased from a 4 mm diameter beam to 7.8 mm. This will make the MOT less sensitive to alignment, and increase the amount of atoms trapped.

6.3 Summary

In this chapter, characterisation of the prototype atom interferometers MOT is presented, with atom number measurements of one million, and release recapture temperature measurements, made capable by the new laser system. The development of a release sequence, which further cooling the atoms in an optical molasses, before turning off all the lasers to allow the atoms to enter free fall is discussed. This resulted in an atomic source at 96 $/muK$. Whilst below the Doppler cooling limit, it is still too large a temperature for the interferometer. Upgrades to the beam quality and intensity are described and are currently being implemented.

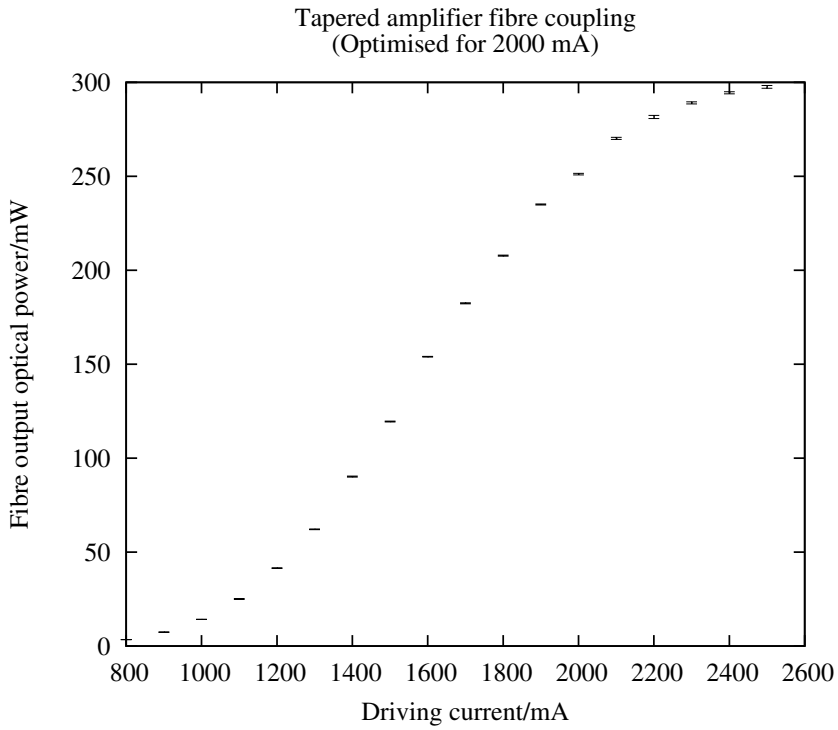

Figure 6.26: Graph of TA optical power launched onto the optical table as the driving current is varied.

Chapter 7

Next Steps to Commissioning the Interferometer and Future Improvements.

The apparatus presented is currently in the commissioning stages. A MOT has been implemented, and further cooled in an optical molasses. The upcoming milestones are discussed here.

Demonstrate Dropping the Atom Cloud. Before any further techniques can be tested, the optical molasses must be released without reheating the atoms and dropped without any initial momenta. Optimisation of the release procedure will allow for colder atoms to be dropped and improved beam alignment and balancing will facilitate a release without initial velocity. The recently introduced fibre cleaning of the MOT beams will provided well balanced beam profiles. The introduction of a TA allows the use of larger beam diameter, which will make the MOT less sensitive to the beam alignment.

Another upgrade currently being implemented is an additional set of coils. Three pairs of square Helmholtz like coils are being built to enable shifting the zero point of the MOT magnetic field by up to 2 mm. Currently the anti-Helmholtz coils have been placed by eye to be geometrically centred to the vacuum chamber and then adjusted to move the MOT to the centre of the beams. The additional coils will enable the centre of the magnetic field to be translated with more precision.

With these upgrades, the MOT should be recommissioned and re-characterised, including temperature measurements for a molasses cooled MOT. The parameters likely to be most significant to the molasses released atoms are the trap intensity, the ramping down time of the trap beams and the optimisation of the magnetic field cancellation coils. Whilst increasing the trap beam intensity will trap more atoms, but has been shown to be detrimental to the temperature of the atoms (see 6.14. Some experiments use multiple staged intensity ramping in their molasses

stage, which may need investigating [40]. The cancellation of the magnetic fields is only down to 100 mG, and further optimisation will lead to colder atoms [70].

When the temperature has been lowered sufficiently, it will be possible to image that atoms have entered free fall. Temperatures as low as 30 μK have been achieved with ^{85}Rb [46]. This could be done initially in the MOT chamber much like a temperature measurement, pulsing the lasers back on to observe the molasses for varying time t, up to 28 ms where the atoms will have left the trap beam. Using the three cameras available, the cloud could be fit for each frame, and the trajectory could be determined from the centre of the cloud over time.

Detection of the atoms in the bottom chamber would be a more significant milestone, and would allow a time of flight temperature measurement to be done using the detection beam [83]. Another camera installed here would allow first measurement without commissioning the PMT.

State Detection and Rabi cycle. Once there is a cloud of freely falling atoms, Raman beams may be used to manipulate the state populations. Raman pulses on the tens of microseconds time scale should transfer the atoms between the two ground states, and the Rabi cycles may be traced out [25]. Initially this could be done immediately after the molasses stage, and the MOT beams and cameras could be used for detection. The MOT trap beam would behave as the detection beam and the MOT pump beam as the pump beam, as described in section 4.5.

State preparation. Applying a bias field to free falling atoms will split the magnetic sub-states of the atoms by 160 kHz/G [50]. Individual magnetic sub-states will be addressed by the Raman beams. If the Rabi frequency of the Raman transitions is determined, π pulses can be applied to the individual sub-states, transferring them to the other ground-state. If a detection pulse was then applied, their absence would be detected, and the fraction of atoms in each state could be measured. This may be used to test and optimise the state selection method via optical pumping as describe in section 4.3.

Similarly the Raman beams may be used to implement the 1-D velocity selection on the atoms. This will reduce their velocity profile along the interferometer beam axis. The slower expansion of the atom cloud in this direction may be imaged.

Interferometer Fringes. After applying the state preparation to free falling atoms, the interferometry sequence can be applied, and the state ratios can be detected. This will initially be easier to do in the upper chamber, using a time between the pulses of the order milliseconds. When the atoms are being successfully interfered, the blackout cage for the PMT should be installed, and precise measurements of the atoms in the detection chamber with the PMT should be attempted.

Local Gravitational Acceleration Measurement. With successful interference detected, the device should be benchmarked, with a measurement of the gravitational acceleration of the atoms. Measuring the fraction of atoms in $5S_{\frac{1}{2}}$ F = 3, as a function of chirp rate of the Raman beams will trace out interferometer fringes. Repeating this for different time periods between pulses T will trace out more fringes. For the chirp rate that exactly cancels out the Doppler affect due to the gravitational acceleration of the atoms, all of the fringes will have a maxima that coincide.

Tidal Measurements of Local Gravitational Acceleration Measurement Once gravity measurements can be made, a demonstration of the device running repeatedly for a long time would be good milestone. Typically these types of devices are not operated continuously for more than a period of a week. The proposed parameter space search for DCV would need continuous running for maximal statistics.

The gravitation strength varies due to various parameters, such as the position of the Moon and tides, atmospheric pressure and the amount of ground water. If the gravitational measurements can be automated, these variations in gravitational accelerations could be tracked as a benchmark of the device.

7.1 Future Upgrades.

Several improvements are planned for the device but were not implemented in this iteration of the apparatus. These included launching the atoms into a fountain, a 2-D MOT as a cold atom source for the interferometer, state selection using microwaves, active vibration isolation and magnetic shielding. Optical amplification of the trap beam is also discussed, which is currently being implemented

7.1.1 Optical Amplification.

The trap beam has been amplified using a TA, producing 300 mW of usable optical power in the frequency generating circuit from a previous value of 40 mW. More power is believed possible with further optimisation. The power amplification is done immediately after the locking circuit, so that the increase of power benefits all of the trap derived intensities.

The MOT and the Raman beams would both be improved by an increase in optical power. The MOT would benefit from higher beam intensity, as the number of atoms trapped is proportional to the intensity of the trap beams, at least in the current regime (where trap beam intensity and saturation intensity are approximately the same) see figure 6.7. A better way to increase the number of atoms would be to increase the beam diameter, whilst maintaining maximum beam intensity. It is discussed in [84] that the

trapping rate is proportional the trapping beam diameter to the 4th power, d^4. This is by increasing the trapping volume, which increases the capture velocity, which is also a function of beam diameter. Increasing the trapping rate increases the number of atoms trapped by a MOT, which is $N = \frac{R}{\Gamma_c}$, where Γ_c is the MOT atom loss by collision.

Assuming a linear relationship between intensity and atom number, increasing the diameter should increase the number of atoms with a d^2 relationship. This can be used to speculate about improvements in the number of atoms trapped.

It is estimated with larger beams and more beam power, atom numbers as high as 10^8 may be realised, commensurate with existing atom interferometers.

High transfer efficiency of the Raman beams is achieved with high Raman Rabi frequency. The effective Rabi frequency of the two photon transitions is

$$\Omega_{eff} \equiv \frac{\Omega_1 \Omega_2}{2\Delta} \approx \frac{\Gamma^2 I}{4 I_{sat} \Delta}, \tag{7.1}$$

where Ω_i is the Rabi frequency of the individual beams for both beams, Γ is the natural linewidth, I is the intensity, Δ is the detuning from the higher energy ground state, in ^{85}Rb, F = 3 [36] [25]. Higher Rabi frequency could be achieved by decreasing the detuning, however this would increase spontaneous emission. This leaves increasing the intensity of the beams as the best solution to increase the frequency, which would require an increase in trap laser power.

7.1.2 Active Vibration Isolation.

The Raman beam is comprised of two frequencies, and the beam is counter-propagating. Both frequencies originate from the fibre and launched down where the beam is retro-reflected on a mirror. Vibrations on this mirror changes the path length of the reflected beam, changing the phase imprinted on the atoms. Vibrations on the fibre length changes the path length of both the Raman beams equally, so no phase shift is seen by the atoms. The optics generating the Raman frequencies are much less sensitive to vibration as they are closely spaced on the optical table and to first order unaffected to vibrations in the vertical direction. The interferometer would therefore benefit from vibration isolation of the retro-reflecting Raman beam mirror.

Vibrations below the $1/T$ frequency effect the interferometer the most. Higher frequency vibrations than this average out, and frequencies above 1 Hz are also more easily passively absorbed. Frequencies below 1 Hz are usually seismic in nature and are harder to passively remove. The amplitude of these vibrations are dictated by the choice of experiment. Currently the experiment is located on the second floor of the Oliver Lodge laboratory. Moving to the ground floor would minimise any building vibrations. A better site for the experiment would be at the Cockcroft institute, which is built directly onto the ground rock, which is some of the most stable in the country. A comparison between the Cockcroft MEIS room laboratory with the Oliver Lodge clean

room floor, and also an passive vibrationally isolated table also at the Oliver Lodge laboratory, can be seen in figure 7.1. In the sub-Hertz regime, vibrations sourced from micro-seismic events can be seen as a peak. These would be a significant noise source for atom interferometers with time scales longer than a second.

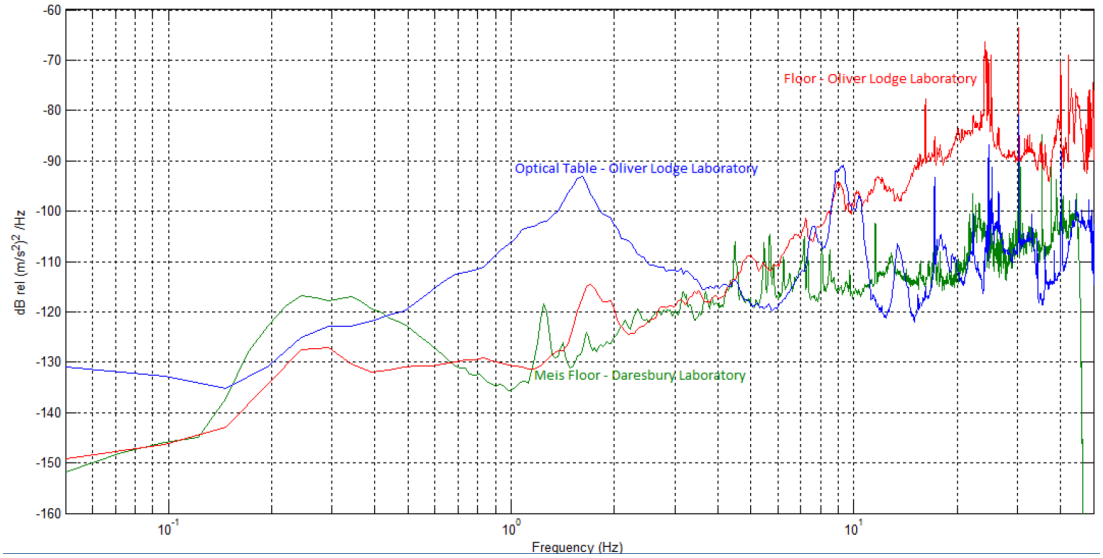

Figure 7.1: A comparison between the Cockcroft MEIS room laboratory with the Oliver Lodge clean room floor, and also an passive vibrationally isolated table also at the Oliver Lodge laboratory.

The vibrations are likely to be cause fluctuations larger than the phase shift due to the tidal variations [73]. Work on vibration isolation has been done by a Masters student. Vibrations are measured by a seismometer, which provided proportional feedback to a Minus-K vibration isolation platform modified with actuators to minimise vibrations, and an active vibration isolation platform has been tested. However the footprint of the isolation device is too large to be placed under our experiment, so it's integration into the interferometer will have to wait until the next vacuum restructure.

7.1.3 Microwave State Selection

The planned method of state selection is an optical pumping method. Alternative state selection methods using microwave pulse are possible. These operate by transferring atoms from one ground state to the other using microwave pulses, at the frequency of the splitting of the states.

The simplest of these uses microwaves in the following way [25]. As in the optical state selection, a bias field is applied to split the magnetic sub-states. Then all atoms in $5S_{\frac{1}{2}}$ F = 2 are blown away using an optical beam. Then a microwave pulse with a duration of a π pulse transfers the atoms from $5S_{\frac{1}{2}}$ F = 3 $\rightarrow$ $5S_{\frac{1}{2}}$ F = 2. Finally, another optical blow away pulse removes atoms left in the F = 3 pulse. The advantage of this technique is that is doesn't incur any heating of the atoms, which the optical

method might. The disadvantage of the technique is that only atoms from the $5S_{\frac{1}{2}}$ F $= 3, m_F = 0$ state are transferred to the $5S_{\frac{1}{2}}$ F $= 2$, $m_F = 0$ state. This means that $\frac{6}{7}$ of the atoms are discarded (atoms in $m_F = \pm 1, \pm 2, \pm 3$ will be blown away by the final pulse), not factoring in the efficiency of the microwave π pulse.

More complex microwave comb techniques can be used to transfer atoms from all of the magnetic sub-states [85] [86].

7.1.4 Atomic Fountain

The accuracy of the interferometer is proportional to $T^2 \propto Z$. Increasing the height of the experiment means increasing the height of the interferometry tube, which is constrained by the size of the vacuum chamber and eventually the laboratory. The laboratory in Liverpool can accommodate an experiment of height about one metre. As the experiment is associated with the Cockcroft Institute at Daresbury, there may be opportunity to use the old MEIS experiment room, approximately ten metres, and the Daresbury tower which is one hundred metres [1], both located at the Cockcroft Institute. Atom interferometers built to full height in these room would improve the sensitivity of the experiment by one or two orders of magnitude respectively.

Moving to either of these sites would involve a large rebuild of the experiment, and continuous running a ten metre atom interferometer has yet to be demonstrated. A smaller upgrade, would be to turn the experiment into an atomic fountain instead of a drop. By trapping atoms at the base of the experiment, launching them upwards at the correct velocity so they enter a parabolic flight making the most of the experimental chamber, the time of flight T can effectively be doubled, increasing the sensitivity by a factor of 4.

To implement a fountain, the atom cloud must be launched vertically. This means locating the cold atom source at the bottom of the vacuum chamber and a modifying the diagonal molasses beams. The two downward propagating beams would be detuned an extra δ_{launch} and the upward beams would be blue tuned by the same amount. Effectively this shifts the inertial frame where the laser beams have the same frequency to one that is moving upwards. This launches the atoms in a moving optical molasses, and this skewed detuning is normally done after the initial molasses detuning step. In a 1,1,0 beam geometry, the velocity achieved by an asymmetric detuning of δ_{launch} is

$$v = \sqrt{2}\delta_{launch}\lambda, \tag{7.2}$$

where λ is the wavelength. For a 1 m launch, a velocity of 4.4 m/s is reached with a $\delta_{launch} = 4\ MHz$. This could be achieved by modifying the frequency generation circuit by splitting the beam into three after the double pass of AOM0 and introducing two

[1] There is currently one functioning 10 m interferometer in the world, functioning in single shot mode, a 100 m interferometer would be far in the future.

further 80 MHz AOM's. These AOM's would perform the same function as AOM1, but would allow three different frequencies for the MOT beams. The spherical octagon would have to be mounted at the base of the vacuum chamber, with the associated MOT optics to implement a fountain.

7.1.5 2-D MOT

It is desirable for the parameter search of the vacuum to have a high repetition rate, to acquire high statistics. Currently the MOT is loaded from a diffuse background vapour, and only the low velocity end of the Boltzmann velocity distributed atoms are captured in the MOT. To increase the repetition rate of the experiment, the MOT loading time needs to be decreased. Without changing the current apparatus, the only way to decrease the loading time would be to increase the background vapour pressure. This would be undesirable, as it would increase the background fluorescence, decreasing the contrast of the interferometer.

One way to load the trap faster without increasing the background vapour pressure is a 2D-MOT [87]. This is like a regular 3D-MOT, but the topology of the magnetic field has a line of zero magnetic field, and there are only two cooling beams, orthogonal to the zero of magnetic field. This creates a line of laser cooled atoms, which can be pushed into the 3-D MOT. An illustration can be seen in figure 7.2. It is planned that this occurs in a side chamber attached to the main chamber by a differential pumping tube. The pressure in the main chamber can be 10^{-11} $mbar$ whilst in the 2D-MOT chamber it is 10^{-8} mbar. When atoms are required in the main chamber, they are trapped in the 2D-MOT and a beam pushes the atoms through the differential pumping tube, into the main chamber, to be trapped by the 3D-MOT. These cold atoms are rapidly loaded into the 3D-MOT.

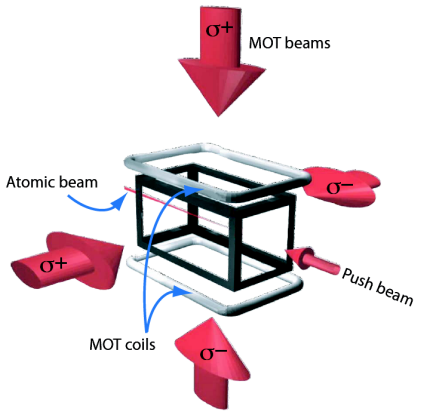

Figure 7.2: Illustration of a 2-D MOT [88].

A 2-D MOT has been developed in Liverpool using a glass pyrex square cell. Permanent magnets were used to simplify the sub-system. The rubidium is loaded into

the cell using the same getters used in the 3-D MOT. A photograph can been seen in figure 7.3. To integrate the sub-system into the interferometer, the vacuum chamber needs to replace the current getter source in the MOT and the frequency requirements need addressing in the laser system.

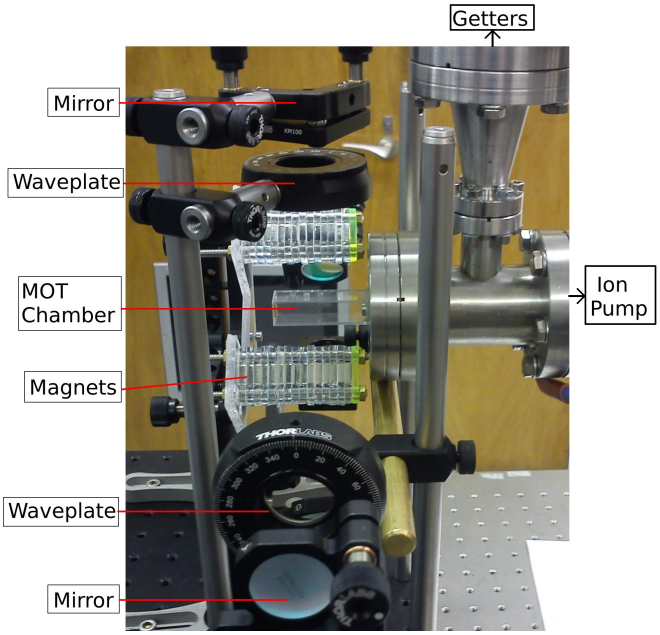

Figure 7.3: Photograph of the 2-D MOT.

7.1.6 Magnetic Shielding

Whilst the atoms are in the magnetically insensitive state $m_F = 0$, they are still effected by the second order Zeeman effect. Also any magnetic gradients will accelerate the atoms. To minimise this, the interferometry region can be magnetically shielded. This would consist of several layers of μ-metal around the interferometry region. This would typically be done with concentric cylinders [89]. Each cylinder will shield the region one radius from the end of the cylinder. The bias coil needs to be wound on the inside of this shielding. Currently this has not been implemented, but in a future implementation a 1 m titanium vacuum tube 4" diameter is ready to act as the interferometry region, and a design for the magnetic shielding is in place.

7.2 Systematic Sensitivity Limits to a Measurement of $\Delta\phi$

Once a working prototype has been developed, and measurements have been made, the next step is to investigate the sensitivity limits of the device. These systematic errors come in through the detection method, phase and frequency fluctuations on the Raman beams, and vibrations. A detailed study into the noise limitations to the sensitivity of gravity measurements with atomic interferometers is presented by Gouet et al [29].

The noise on the detection signal at low atom number will be dominated by instrumentation noise in the detector. With higher atom number this is limited by fluctuations on the laser beams frequency and intensity. This can be minimised by using more sophisticated detection schemes, which detect both states simultaneously and for longer durations [90]. Schemes such as this can be used to reach the shot noise limit.

The noise from the detection is measured with atoms prepared in a 50:50 population ratio with a microwave $\pi/2$ pulse. The error on the population measurements, σ_P is the Allan standard deviation. This gives an error on phase of $\sigma_\phi = \frac{2\sigma_P}{C}$, where C is the contrast. With a detection scheme limited by the shot noise, $\sigma_P = \frac{1}{2\sqrt{N}}$.

Noise on the RF generator, fluctuations in the Raman fibre length, fluctuations in path difference of the Raman beams before combination, fluctuations in laser intensity, magnetic fields and vibrations in the retro-reflecting mirror can all impart phase noise onto the atoms. The phase noise can be calculated using the following prescription. The Allan variance of the interferometric phase is given by

$$\sigma_\phi^2(\tau) = \frac{1}{\tau}\sum_{n=1}^{\infty} |H(2\pi n f_c)|^2 S_\phi(2\pi n f_c), \tag{7.3}$$

where τ is a multiple of the time an interferometry sequence takes, T_c. The frequency f_c is the repetition rate of the interferometer. The values S_ϕ is the noise power spectral density of the noise source the contribution is being calculated for, which would be experimentally measured. The function $H(2\pi n f_c)$ is the transfer function, given by $\omega G(\omega)$, where $G(\omega)$ is the Fourier transform of the sensitivity function,

$$G(\omega) = \int_{-\infty}^{\infty} e^{i\omega t} g(t) dt, \tag{7.4}$$

where the sensitivity function $g(t)$ for a $\pi/2 - \pi - \pi/2$ sequence is an odd function,

$$g(t) = \begin{cases} sin\Omega_R t & 0 < t < \tau_R \\ 1 & \tau_R < t < T + \tau_R \\ -sin\Omega_R(T-t) & T + \tau_R < t < T + 2\tau_R, \end{cases} \tag{7.5}$$

where Ω_R is the Rabi frequency of the Raman pulses, τ_R is the duration of a $\pi/2$ pulse, and T is the time between pulses. For the range $t > |T + 2\tau_R|$, $g(t) = 0$.

The noise power spectral density for the RF generator, fluctuations in the fibre length and path differences before the Raman beam combination can all be measured using a fast photo-diode. Measuring the beat frequency between the two Raman beams as they're launched from the fibre measures the effect of these three sources in one. From this the noise power spectral density can be measured using a spectrum analyser, and the effect of phase noise on the Raman beams is given by equation 7.3. The power

spectral densities for phase shifts imparted by the mirror vibration can be measured using a seismometer and the phase noise can be calculated in a similar way.

The relative intensity of the Raman beams is set to cancel the AC Stark shift. The two parts of the Raman beam should have an intensity ratio of 1:3.67 to cancel the AC Stark effect for ^{85}Rb atoms with a 1.5 GHz detuning [91]. Fluctuations in the intensity balance of the Raman beams can causes fluctuating AC Stark shifts, which in turn causes small phase shifts on the atoms. Measuring the intensity power spectral densities for the two parts of the Raman beams the noise on the phase can then determined, again is described in [29]. These shifts only effect the interferometer during the interferometry pulses.

Magnetic fields will produce a quadratic Zeeman shift in the atoms. Measuring the magnetic field along the path of the atoms allows the phase shift to be calculated. It can also be measured by reversing the k_{eff} vector, where the phase shift will be the opposite sign. If the short term fluctuations in the magnetic field can be determined, the effect on the phase can be calculated.

With a full systematic study of the interferometer, the weakest component in the experiment can be identified and improved.

Chapter 8

Summary

This work has been the development of a ^{85}Rb atom interferometer for a parameter space search for Dark Contents of the Vacuum. Magneto-optical trap apparatus was designed and implemented. This involved constructing an ultra-high vacuum chamber with an integrated warm atom source, suitable for implementing laser cooling. The required electro-magnets were commissioned and frequency controlled ECDL sources were implemented. This apparatus was used with two optical circuits, initially a retro-reflecting trap, which was later developed into a six beam power balanced trap. Atom number measurements were made on this system, trapping 6.6×10^6 atoms.

The group designed a prototype atom interferometer, and my contribution was to the magneto-optical trap and optical molasses system, which involved creating cancellation coils to minimise the background magnetic fields. A laser frequency generation scheme was implemented to create all of the required laser frequencies for the interferometer.

Using the timing and frequency control of the laser system, I characterised the MOT, performed initial optimisation of the optical molasses stage, creating optical molasses with lifetimes of order half a second and developed a molasses release sequence. Cold atom sources of with 10^6 atoms at 96 μK have been created in the interferometer MOT apparatus.

From starting on the experiment as the first PhD student, the team has grown, and we have progressed from a nearly empty lab, to a prototype atom interferometer, creating optical molasses cooled atom sources. Upgrades to the laser system and MOT beam delivery system are expected to increase the number of atoms to order 10^8 atoms at lower temperatures. This will be achieved by optically amplifying the trap beams with a TA, and fibre cleaning the trap beams to improve intensity balancing in optical molasses [1]. With these atomic samples, the state selection, interferometry Raman pulses and state detection can be developed into an working atom interferometer, and benchmarking measurements of gravity and systematic limitations studies can be

[1] 10^8 atoms has been achieved during the writing of this document

performed.

Beyond this, future upgrades are planned to upgrade the device to a 1 m precision device, equivalent similar international research devices. The next step from here would be a two atom interferometer system, capable of performing a parameter space search for dark contents of the vacuum.

Bibliography

[1] P.A.R. Ade et al. Planck 2013 results. XVI. Cosmological parameters. *Astron.Astrophys.*, 571:A16, 2014.

[2] P.A.R. Ade et al. Joint Analysis of BICEP2/*KeckArray* and *Planck* Data. *Phys. Rev. Lett.*, 114:101301, 2015.

[3] W. J. Percival, B. A. Reid, D. J. Eisenstein, N. A. Bahcall, T. Budavari, J. A. Frieman, M. Fukugita, J. E. Gunn, Ž. Ivezić, G. R. Knapp, R. G. Kron, J. Loveday, R. H. Lupton, T. A. McKay, A. Meiksin, R. C. Nichol, A. C. Pope, D. J. Schlegel, D. P. Schneider, D. N. Spergel, C. Stoughton, M. A. Strauss, A. S. Szalay, M. Tegmark, M. S. Vogeley, D. H. Weinberg, D. G. York, and I. Zehavi. Baryon acoustic oscillations in the Sloan Digital Sky Survey Data Release 7 galaxy sample. *MNRAS*, 401:2148–2168, February 2010.

[4] Saul Perlmutter. Nobel lecture: Measuring the acceleration of the cosmic expansion using supernovae*. *Rev. Mod. Phys.*, 84:1127–1149, Aug 2012.

[5] K.A. Olive and Particle Data Group. Review of particle physics. *Chinese Physics C*, 38(9):090001, 2014.

[6] PRISM Collaboration. PRISM (Polarized Radiation Imaging and Spectroscopy Mission): A White Paper on the Ultimate Polarimetric Spectro-Imaging of the Microwave and Far-Infrared Sky. *ArXiv e-prints*, June 2013.

[7] LSST Dark Energy Science Collaboration. Large Synoptic Survey Telescope: Dark Energy Science Collaboration. *ArXiv e-prints*, November 2012.

[8] F. Arneodo. Dark Matter Searches. *ArXiv e-prints*, January 2013.

[9] A. d. C. o. b. o. t. CMS and ATLAS collaborations. LHC results for dark matter from ATLAS and CMS. *ArXiv e-prints*, October 2015.

[10] T. Marrodán Undagoitia and L. Rauch. Dark matter direct-detection experiments. *Journal of Physics G Nuclear Physics*, 43(1):013001, January 2016.

[11] LIGO collaboration. Observation of gravitational waves from a binary black hole merger. *Phys. Rev. Lett.*, 116:061102, Feb 2016.

[12] The LIGO Scientific Collaboration and the Virgo Collaboration. Characterization of transient noise in Advanced LIGO relevant to gravitational wave signal GW150914. *ArXiv e-prints*, February 2016.

[13] VIRGO collaboration. Advanced virgo: a second-generation interferometric gravitational wave detector. *Classical and Quantum Gravity*, 32(2):024001, 2015.

[14] R. J. Adler, H. Mueller, and M. L. Perl. a Terrestrial Search for Dark Contents of the Vacuum, such as Dark Energy, Using Atom Interferometry. *International Journal of Modern Physics A*, 26:4959–4979, 2011.

[15] REINHOLD KLEINER, DIETER KOELLE, FRANK LUDWIG, and JOHN CLARKE. Superconducting quantum interference devices: State of the art and applications. *Proceedings of The IEEE*, 92:1534–1548, 2004.

[16] Mark Kasevich. *Atom interferometry in an atomic fountain*. PhD thesis, Stanford, 1992.

[17] A Peters, K Y Chung, and S Chu. High-precision gravity measurements using atom interferometry. *Metrologia*, 38(1):25, 2001.

[18] P. Berg, S. Abend, G. Tackmann, C. Schubert, E. Giese, W. P. Schleich, F. A. Narducci, W. Ertmer, and E. M. Rasel. Composite-light-pulse technique for high-precision atom interferometry. *Phys. Rev. Lett.*, 114:063002, Feb 2015.

[19] M. Prevedelli, L. Cacciapuoti, G. Rosi, F. Sorrentino, and G. M. Tino. Measuring the newtonian constant of gravitation g with an atomic interferometer. *Philosophical Transactions of the Royal Society of London A: Mathematical, Physical and Engineering Sciences*, 372(2026), 2014.

[20] M. Cadoret, E. de Mirandes, P. Clade, S. Guellati-Khelifa, C. Schwob, F. Nez, L. Julien, and F. Biraben. Determination of the fine structure constant with atom interferometry and bloch oscillations on 87rb atoms. In *Precision Electromagnetic Measurements Digest, 2008. CPEM 2008. Conference on*, pages 38–39, June 2008.

[21] M. Hauth, C. Freier, V. Schkolnik, A. Senger, M. Schmidt, and A. Peters. First gravity measurements using the mobile atom interferometer gain. *Applied Physics B*, 113(1):49–55, 2013.

[22] M. Kasevich. Atom interferometric navigation sensors. In *Sensors, 2010 IEEE*, pages 15–16, Nov 2010.

[23] Mark Kasevich and Steven Chu. Atomic interferometry using stimulated raman transitions. *Phys. Rev. Lett.*, 67:181–184, Jul 1991.

[24] Kathryn Moler, David S. Weiss, Mark Kasevich, and Steven Chu. Theoretical analysis of velocity-selective raman transitions. *Phys. Rev. A*, 45:342–348, Jan 1992.

[25] Malte Schimdt. *A mobile high-precision gravimeter based on atom interferometry.* PhD thesis, Humboldt Universitat, 2011.

[26] E. L. Raab, M. Prentiss, Alex Cable, Steven Chu, and D. E. Pritchard. Trapping of neutral sodium atoms with radiation pressure. *Phys. Rev. Lett.*, 59:2631–2634, Dec 1987.

[27] J. Dalibard and C. Cohen-Tannoudji. Laser cooling below the doppler limit by polarization gradients: simple theoretical models. *J. Opt. Soc. Am. B*, 6(11):2023–2045, Nov 1989.

[28] S. M. Dickerson, J. M. Hogan, A. Sugarbaker, D. M. S. Johnson, and M. A. Kasevich. Multiaxis Inertial Sensing with Long-Time Point Source Atom Interferometry. *Physical Review Letters*, 111(8):083001, August 2013.

[29] J. Le Gouët, T. E. Mehlstäubler, J. Kim, S. Merlet, A. Clairon, A. Landragin, and F. Pereira Dos Santos. Limits to the sensitivity of a low noise compact atomic gravimeter. *Applied Physics B: Lasers and Optics*, 92:133–144, August 2008.

[30] Pippa Storey and Claude Cohen-Tannoudji. The feynman path integral approach to atomic interferometry. atutorial. *J. Phys. II France*, 4(11):1999–2027, 1994.

[31] Ch. J. Bord. 5d optics for atomic clocks and gravito-inertial sensors. *The European Physical Journal Special Topics*, 163(1):315–332, 2008.

[32] Christian J. Bord. Theoretical tools for atom optics and interferometry. *Comptes Rendus de l'Acadmie des Sciences - Series {IV} - Physics*, 2(3):509 – 530, 2001.

[33] Ch.J. Bord. Atomic interferometry with internal state labelling. *Physics Letters A*, 140(12):10 – 12, 1989.

[34] *Laser Spectroscopy X*. World Scientific, 1992.

[35] Achim Peters. *High precision gravity measurements using atomic interferometry.* PhD thesis, Stanford University, 1998.

[36] Grant Biedermann. *Gravity tests, differential accelerometry and interleaved clocks with cold atom interferometers.* PhD thesis, Stanford University, 2007.

[37] C. Antoine. Matter wave beam splitters in gravito-inertial and trapping potentials: generalized ttt scheme for atom interferometry. *Applied Physics B*, 84(4):585–597, 2006.

[38] Giacomo Lamporesi. *Determination of the gravitational constant by atom interferometry*. PhD thesis, Universit degli studi di Firenze, 2006.

[39] Sheng-wey Chiow, Sven Herrmann, Steven Chu, and Holger Müller. Noise-immune conjugate large-area atom interferometers. *Phys. Rev. Lett.*, 103:050402, Jul 2009.

[40] A. Bertoldi, G. Lamporesi, L. Cacciapuoti, M. de Angelis, M. Fattori, T. Petelski, A. Peters, M. Prevedelli, J. Stuhler, and G. M. Tino. Atom interferometry gravity-gradiometer for the determination of the newtonian gravitational constantg. *The European Physical Journal D - Atomic, Molecular, Optical and Plasma Physics*, 40(2):271–279, 2006.

[41] Sheng-wey Chiow, Tim Kovachy, Hui-Chun Chien, and Mark A. Kasevich. $102\hbar k$ large area atom interferometers. *Phys. Rev. Lett.*, 107:130403, Sep 2011.

[42] E Rocco, R N Palmer, T Valenzuela, V Boyer, A Freise, and K Bongs. Fluorescence detection at the atom shot noise limit for atom interferometry. *New Journal of Physics*, 16(9):093046, 2014.

[43] *Proceedings of the International School of Physics "Enrico Fermi"*, chapter Matter wave interferometry beyond classical limits. IOS Press, 2014.

[44] A. Peters, K. Y. Chung, B. Young, J. Hensley, and S. Chu. Precision atom interferometry. *Philosophical Transactions of the Royal Society of London A: Mathematical, Physical and Engineering Sciences*, 355(1733):2223–2233, 1997.

[45] M. Hauth, C. Freier, V. Schkolnik, A. Senger, M. Schmidt, and A. Peters. First gravity measurements using the mobile atom interferometer gain. *Applied Physics B*, 113(1):49–55, 2013.

[46] L. Zhou, Z.Y. Xiong, W. Yang, B. Tang, W.C. Peng, K. Hao, R.B. Li, M. Liu, J. Wang, and M.S. Zhan. Development of an atom gravimeter and status of the 10-meter atom interferometer for precision gravity measurement. *General Relativity and Gravitation*, 43(7):1931–1942, 2011.

[47] Alex Sugarbaker. *ATOM INTERFEROMETRY IN A 10 M FOUNTAIN*. PhD thesis, Stanford, 2014.

[48] William D. Phillips. Nobel lecture: Laser cooling and trapping of neutral atoms. *Rev. Mod. Phys.*, 70:721–741, Jul 1998.

[49] Steven Chu, L. Hollberg, J. E. Bjorkholm, Alex Cable, and A. Ashkin. Three-dimensional viscous confinement and cooling of atoms by resonance radiation pressure. *Phys. Rev. Lett.*, 55:48–51, Jul 1985.

[50] Daniel A. Steck. Rubidium 85 D Line Data. URL http://steck.us/alkalidata/rubidium85numbers.pdf.

[51] Carl Wieman, Gwenn Flowers, and Sarah Gilbert. Inexpensive laser cooling and trapping experiment for undergraduate laboratories. *American Journal of Physics*, 63(4), 1995.

[52] Christopher Stevens. Vacuum fail safe and mot image analysis for the atta experiment. Columbia Physics REU, August 2011.

[53] Robert Scholten and Alex Slavec. *External Cavity Diode Laser Model ECD004*. MOGLabs, revision 4.20 edition.

[54] H. Talvitie, A. Pietilinen, H. Ludvigsen, and E. Ikonen. Passive frequency and intensity stabilization of extended-cavity diode lasers. *Review of Scientific Instruments*, 68(1), 1997.

[55] C. J. Hawthorn, K. P. Weber, and R. E. Scholten. Littrow configuration tunable external cavity diode laser with fixed direction output beam. *Review of Scientific Instruments*, 72(12):4477–4479, 2001.

[56] O. I. Permyakova, A. V. Yakovlev, and P. L. Chapovsky. Simple external cavity diode laser. *ArXiv Physics e-prints*, December 2003.

[57] *Laser Diode Beam Basics, Manipulations and Characterizations*. Springer Netherlands, 2012.

[58] The University of Melbourne. Robert Scholten. Personal communication.

[59] Robert Scholten and Alex Slavec. *External Cavity Diode Laser Controller, Models DLC-202, DLC-252, DLC-502*, revision 7.01 edition.

[60] Thorlabs. Doppler broadend vs saturated spectroscopy. `http://www.thorlabs.de/images/TabImages/SAS_Signal_DWG_350.gif"`, OPTmonth = , year = 2015, OPTnote = , OPTannote = , url =.

[61] Robert Scholten. Personal Correspondance, March 2013.

[62] Kimball Physics. *4.50" Spherical Octagon (tapped holes) - Vacuum Chamber*.

[63] Saes getters, www.saesgetters.com. *Alkali Metal Dispensers*.

[64] Umakant D. Rapol, Ajay Wasan, and Vasant Natarajan. Loading of a Rb magneto-optic trap from a getter source. *Phys. Rev. A*, 64:023402, Jun 2001.

[65] H.J. Lewandowski, D.M. Harber, D.L. Whitaker, and E.A. Cornell. Simplified system for creating a boseeinstein condensate. *Journal of Low Temperature Physics*, 132(5-6):309–367, 2003.

[66] Ffmpeg. https://www.ffmpeg.org/.

[67] David Tschumperl. Cimg library. http://cimg.eu/.

[68] U. D. Rapol, A. Wasan, and V. Natarajan. Loading of a Rb magneto-optic trap from a getter source. *Physical Review A 64, 023402 (2001)*, 64(2):023402, August 2001.

[69] Steven Chu. Nobel lecture: The manipulation of neutral particles. *Rev. Mod. Phys.*, 70:685–706, Jul 1998.

[70] P. D. Lett, W. D. Phillips, S. L. Rolston, C. E. Tanner, R. N. Watts, and C. I. Westbrook. Optical molasses. *J. Opt. Soc. Am. B*, 6(11):2084–2107, Nov 1989.

[71] National Oceanic and Atomospheric Administration. Compute earth's magnetic field values, 2014.

[72] Torsten Petelski. *Atom Interferometers for Precision Gravity Measurements*. PhD thesis, Firenze, 2005.

[73] Alexander Senger. *A Mobile Atom Interferometer for High-Precision Measurements of Local Gravity*. PhD thesis, Humboldt-Universitt zu Berlin, 2011.

[74] Achim Peters. *High Precision Gravity Measurements Using Atom Interferometry*. PhD thesis, Stanford, 1998.

[75] Kenneth Franklin Riley and Michael Paul Hobson. *Student solutions manual for mathematical methods for physics and engineering*. Cambridge University Press, Cambridge, 2006. Autre tirage : 2008.

[76] Eric Toombs. Plot of the instantaneous intensity of a gaussian beam as a function of r and z. Wikimedia Commons, July 2011.

[77] *Defining, measuring, and optimizing laser beam quality*, volume 1868, 1993.

[78] *Acousto-optics*. Chichester ; New York : Wiley, 1979.

[79] E. A. Donley, T. P. Heavner, F. Levi, M. O. Tataw, and S. R. Jefferts. Double-pass acousto-optic modulator system. *Review of Scientific Instruments*, 76(6):–, 2005.

[80] L. Russell, R. Kumar, V. B. Tiwari, and S. Nic Chormaic. Measurements on release-recapture of cold ^{85}Rb atoms using an optical nanofibre in a magneto-optical trap. *Optics Communications*, 309:313–317, November 2013.

[81] Toptica Photonics. *High Power Diode Lasers and Amplifiers*, 2015.

[82] D. Voigt, E. C. Schilder, R. J. C. Spreeuw, and H. B. van Linden van den Heuvell. Characterization of a high-power tapered semiconductor amplifier system. *Applied Physics B: Lasers and Optics*, 72:279–284, 2001.

[83] I. Yavin, M. Weel, A. Andreyuk, and A. Kumarakrishnan. A calculation of the time-of-flight distribution of trapped atoms. *American Journal of Physics*, 70(2), 2002.

[84] Kurt E. Gibble, Steven Kasapi, and Steven Chu. Improved magneto-optic trapping in a vapor cell. *Opt. Lett.*, 17(7):526–528, Apr 1992.

[85] Jeffrey B. Fixler. *Atom interferometer-based gravity gradiometer measurements*. PhD thesis, Stanford, 2003.

[86] Malcolm H. Levitt. *Composite Pulses*. John Wiley & Sons, Ltd, 2007.

[87] J. Schoser, A. Bataer, R. Loew, V. Schweikhard, A. Grabowski, Y. B. Ovchinnikov, and T. Pfau. An Intense Source of Cold Rb Atoms from a Pure 2D-MOT. *ArXiv Physics e-prints*, January 2002.

[88] Thomas Uehlinger. A 2d magneto-optical trap as a high-flux source of cold potassium atoms. Master's thesis, Swiss Federal Institute of Technology Zurich, 2008.

[89] Susannah Dickerson, Jason M. Hogan, David M. S. Johnson, Tim Kovachy, Alex Sugarbaker, Sheng-wey Chiow, and Mark A. Kasevich. A high-performance magnetic shield with large length-to-diameter ratio. *Review of Scientific Instruments*, 83(6):–, 2012.

[90] J. M. McGuirk, G. T. Foster, J. B. Fixler, and M. A. Kasevich. Low-noise detection of ultracold atoms. *Opt. Lett.*, 26(6):364–366, Mar 2001.

[91] R.-B. Li, L. Zhou, J. Wang, and M.-S. Zhan. Measurement of the quadratic Zeeman shift of ^{85}Rb hyperfine sublevels using stimulated Raman transitions. *Optics Communications*, 282:1340–1344, April 2009.